

c.2



Lawrence Berkeley Laboratory

UNIVERSITY OF CALIFORNIA

Materials & Molecular Research Division

RECEIVED
LAWRENCE
BERKELEY LABORATORY

MAY 6 1981

LIBRARY AND
DOCUMENTS SECTION

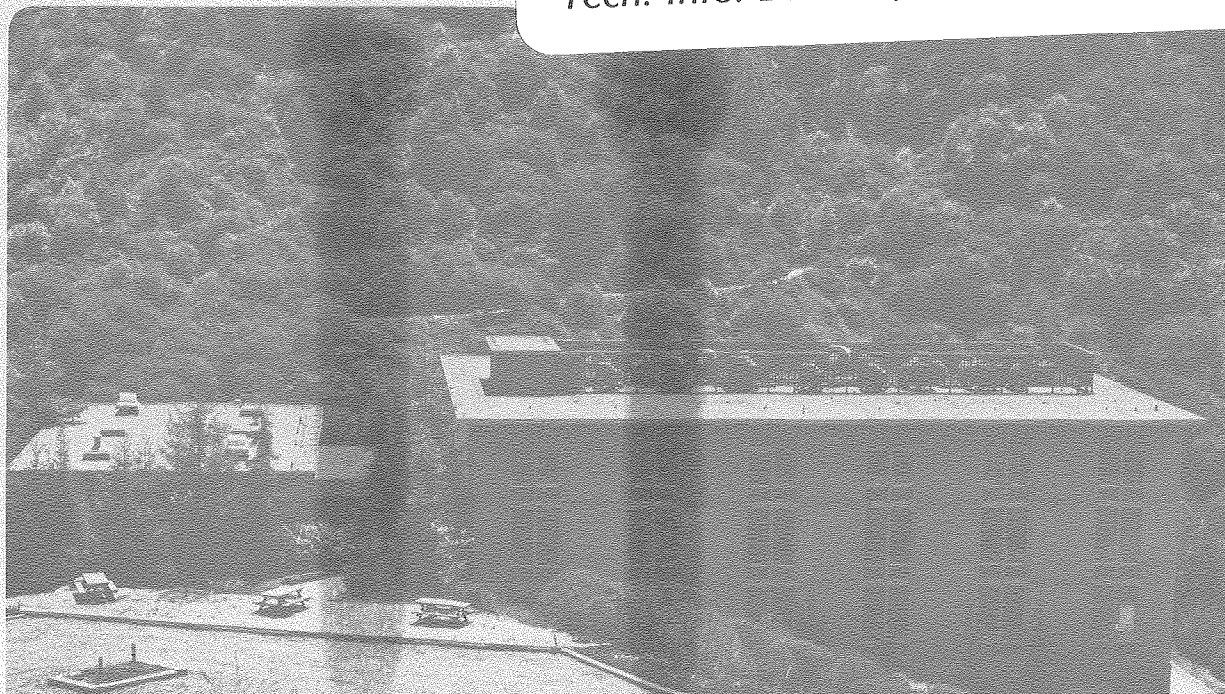
THE RESPONSE OF SOLIDS TO ELASTIC/PLASTIC
INDENTATION AND THE APPLICATION OF INDENTATION
TO ADHESION MEASUREMENTS

Shu-Sheng Chiang
(Ph.D. thesis)

March 1981

TWO-WEEK LOAN COPY

*This is a Library Circulating Copy
which may be borrowed for two weeks.
For a personal retention copy, call
Tech. Info. Division, Ext. 6782.*



LBL-11841
c.2

DISCLAIMER

This document was prepared as an account of work sponsored by the United States Government. While this document is believed to contain correct information, neither the United States Government nor any agency thereof, nor the Regents of the University of California, nor any of their employees, makes any warranty, express or implied, or assumes any legal responsibility for the accuracy, completeness, or usefulness of any information, apparatus, product, or process disclosed, or represents that its use would not infringe privately owned rights. Reference herein to any specific commercial product, process, or service by its trade name, trademark, manufacturer, or otherwise, does not necessarily constitute or imply its endorsement, recommendation, or favoring by the United States Government or any agency thereof, or the Regents of the University of California. The views and opinions of authors expressed herein do not necessarily state or reflect those of the United States Government or any agency thereof or the Regents of the University of California.

The Response of Solids to Elastic/Plastic Indentation
and the Application of Indentation to Adhesion Measurements

by

Shu-Sheng Chiang

Ph.D. Thesis

Materials and Molecular Research Division, Lawrence Berkeley Laboratory
and Department of Materials Science and Mineral
Engineering, University of California
Berkeley, CA 94720

March 1981

This work was supported by the Director, Office of Energy Research, Office of Basic Energy Sciences, Materials Science Division of the U.S. Department of Energy under Contract No. W-7405-ENG-48.

included angles, a cutting process, with a plastic zone shape that accords with rigid/plastic (e.g., slip-line field)¹⁴⁻¹⁶ expectations, is observed (Fig. 1a). For indenters of large included angle, the plastic zone shows spherical symmetry (usually hemispherical), even in materials subject to ready plasticity, e.g., annealed brass (see Fig. 1b). This deformation response (referred to as radial compression) exhibits analogies with the elastic/plastic deformation expected around a cavity subject to internal pressure.¹⁷ The difference between the two deformation responses to indentation is also manifest in the degree of material pile-up around the indentation. In the rigid/plastic regime material is displaced to the surface and therefore gives rise to a large raised lip around the indentation; whereas, for radial compression, very little pile-up is observed. The transition appears to occur over a range of cone angles,^{13,18} such that lower transition angles pertain to materials with a higher hardness-to-modulus ratio. For example, the transition range is $>120^\circ$ for aluminum,¹⁶ $\sim 105^\circ$ for work-hardened mild steel,¹⁸ and $\sim 60^\circ$ for cold rolled brass.¹³ An interpretation of the behavior of indentations exhibiting hemispherical plasticity is the primary focus of this study.

The analogy between the hemispherical indentation zone and the pressurized spherical cavity has been recognized previously, but not fully exploited. Dugdale¹⁹ and Mulhearn¹³ used a rigid-plastic, radial-compression model to relate hardness to the stress strain curve and to calculate the plastic strain field. Marsh²⁰ derived a semi-empirical relation between indentation pressure (hardness) and the ratio of elastic modulus to yield stress, based on Hill's spherical

cavity expansion solution¹⁷ for infinite elastic/plastic materials. The reduced constraint around the hemispherical cavity was introduced by allowing two constants to be adjusted to fit experimental measurements. However, effects of indenter geometry were not explicitly considered. In an alternative analysis, which has been widely adopted in recent studies on indentation, Johnson²¹ attempted to account for the influence of indenter angle by allowing the indentation pressure to be transmitted via an incompressible hydrostatic core beneath the indenter. However, the core in this analysis is a nebulous entity and the predicted indentation pressures appreciably underestimate the measured values (see Fig. 2 and 3).

The present approach commences by reassessing the correlation between indentation deformation and the spherical cavity model, and then develops new concepts for extending the spherical cavity solution to account for the reduced half-space constraint. The approach suggests an analytic procedure for calculating the stress field around an indentation. The stresses deduced in accord with this procedure will be used to consolidate further the indentation plasticity problem and thus to permit trends in the indentation pressure and plastic zone radius (with yield stress and elastic modulus) to be predicted and compared with the experiment. In addition, the stress analysis permits trends in the fracture initiation threshold with material properties to be derived and correlated with experimental observations. Finally, some implications for fracture propagation behavior also emerge from the analysis.

2. INDENTATION ANALYSES

2.1 Basic Hypotheses

Two hypotheses establish the present basis for relating indentation deformation to the spherical cavity model. Firstly, the extent of plasticity (as manifest in the volume V of the plastic zone) is considered to be fundamentally dictated by the plastic work of indentation. Secondly, the plastic zone volume is assumed to be related exclusively to the indentation volume ΔV , independent of the indenter geometry. This proposal is based on the observations (and numerical calculations) both of spherical symmetry in the plastic zone, regardless of indenter geometry,^{12,13,22-24} and, in particular, of identical plastic zone boundaries for spherical and Vickers pyramidal indentation of equal volume.¹²

The above hypotheses necessarily require that the indentation pressure be independent of indenter geometry, because the plastic work of indentation is the product of the indentation pressure and the volume of indentation. The experimental results of Atkins and Tabor¹⁸ on steel and copper are in reasonable accord with this requirement. Specifically, the hardness was determined to vary by <10% over the range of cone angles for which deformation occurs by radial compression (the actual variation depends on the degree of prior work hardening of the indented material; constant hardness occurs at a work hardening strain of about 0.1 - 0.2). In addition, results of pyramidal indentations performed in soda-lime glass, ZnS and As₂S₃ glass confirmed the approximate shape independence of the indentation pressure and plastic zone volume.²⁵

The assumed shape invariance of the indentation pressure and plastic zone dimension permits experimental indentation results to be referred to a common indentation geometry. A convenient reference geometry is the hemispherical indentation, radius a , with hemispherical plastic zone, radius b . The relative hemispherical indentation dimensions, β (see Fig. 4a), can then be simply expressed by the relation:

$$\beta = b/a = (V/\Delta V)^{1/3} \quad (1a)$$

which for pyramidal indentation becomes

$$b/a = (b/\bar{a}) (\pi/\cot\Psi)^{1/3} \quad (1b)$$

where $2\bar{a}$ is the indentation diagonal and 2Ψ is the included angle between opposite edges of the pyramid (see Fig. 4b). For a Vickers indenter, $\Psi = 74^\circ$, and $a = 0.45\bar{a}$. The relationship between a and \bar{a} for pyramidal, conical and spherical indenters is given in Appendix I. Transferring the indentation pressure directly to the reference geometry permits experimental results to be readily compared with hemispherical indentation analyses. The detailed comparison will be conducted following the stress analysis of the elastic/plastic indentation.

2.2 Correlation Between Indentation Experiments and the Spherical Cavity Solution

A preliminary analysis of indentation plasticity is conducted, in accord with the above hypotheses, by adopting the results of the spherical cavity solution¹⁷

$$\frac{p}{Y} = \frac{2}{3} [1 + \ln(\beta)^3] \quad (2a)$$

$$\frac{E}{Y} = 3(1-\nu)(\beta)^3 - 2(1-2\nu) \quad (2b)$$

where p is the indentation pressure, Y is the yield stress, E is Young's modulus, ν is Poisson's ratio and β is defined in eq. (1). These relations can be rearranged to yield expressions that are suitable for direct comparison with experimental results:

$$\frac{E}{p} = \frac{9[1-\nu](\beta)^3 - 2(1-2\nu)/3]}{2[1 + \ln(\beta)^3]} \quad (3a)$$

$$\frac{p}{Y} = \frac{2}{3} \left\{ 1 + \left[\ln \frac{(E/Y) + 2(1-2\nu)}{3(1-\nu)} \right] \right\} \quad (3b)$$

These expressions are plotted in Figs. 2 and 3. The experimental and numerical results for the relative plastic zone size β , (Table I) are compared with Eq. (3a) in Fig. 2. The quality of the correlation (which has not previously been attempted) is encouraging. In particular, it is noted that the experimental results imply that a smaller indentation pressure is needed to attain equivalent plastic zone dimensions in the half-space: a tendency consistent with the reduced elastic constraint of the half-space. This trend is ultimately quantified in Section 3.2.1.

Experimental results relating indentation pressure, yield stress and elastic modulus, elicited from the studies of March²⁰ and Hirst and Howse²⁶ are compared with Eq. (3b) in Fig. 3. (The results for the polymers are given different symbols because these materials are

subject in part to densification plasticity during indentation - as manifest in a refractive index change in the plastic zone²⁷ - and may not, therefore, be suitable for comparison with elastic/plastic solutions.) Again, there is both a good correlation and a tendency for the experimental results to deviate appropriately, toward lower indentation pressures. The existence of this correlation could, in fact, have been deduced from Marsh's²⁰ interpretation of trends in the indentation pressure, in which a reduced constraint was implicitly included in the derivation of a semi-empirical relation for the indentation pressure. The role of the reduced constraint is quantified in Section 3.2.1.

It is appropriate at this juncture to compare the above correlation with that achieved by Johnson²¹ (Figs. 2,3). It is noted that his comparison is less satisfactory, particularly with regard to the plastic zone dimension.

3. STRESS ANALYSIS

3.1 The Method of Solution

Previous studies of elastic/plastic indentation stress fields include an analytic solution²⁸ and several numerical solutions.^{29,30} The analytic solution is based on the premise that the stresses within the elastic zone are identical in form to the stress field created by fully-elastic indentation. This is not an acceptable assumption for the (axisymmetric) indentation problem* and hence, the solution yields stress fields that are inconsistent with several observed trends in crack evolution and in indentation plasticity. The numerical solutions are limited in scope, and do not provide a sufficient characterization of the indentation stress field to permit further analysis. (However, the results provide invaluable sources of comparison, at coincidence points, with analytic solutions). The stress fields needed for the analysis of trends in both fracture thresholds and indentation plasticity are developed in the present paper, using boundary conditions suggested by the reference hemispherical indentation,** discussed in Section 2.

*Elastic stress fields under elastic/plastic conditions are only necessarily similar in form to the equivalent elastic field when the problem is fully symmetric (e.g., in the pressurized spherical cavity). More generally, the only requirement imposed by the elastic solution is that St. Venant's principle³¹ be satisfied, i.e., that the far field stresses be equivalent to those given by the elastic-solution (the Boussinesq solution³² in this case).

**Small deviations from hemispherical symmetry occur in the immediate vicinity of the free surface; but these deviations reduce in magnitude as the penetration increases: becoming negligible at penetrations of one diameter.

The approach commences with the elastic/plastic solution for a spherical cavity, radius a , under a pressure p , which creates a spherical plastic zone, radius b . This provides an initially symmetric elastic/plastic field (Fig. 5). Then a free surface is created by eliminating the tangential stress field acting over a plane through the cavity center (Fig. 5). This is achieved by using the elastic point force solutions pertinent to the half-plane problem provided by Mindlin,³³ i.e., point forces that do not create either a normal stress or in-plane shear stresses at the 'surface' plane, as illustrated in Fig. 5. The stresses that result from these forces superimpose onto the initial, symmetric stresses to generate the indentation stress field. This procedure would not normally be justified for elastic/plastic problems. However, it will be demonstrated that, for the present problem, this approach (by virtue of the symmetry) provides a self-consistent solution.

Application of the surface forces induces a radial stress, σ_r^S , at the location of the cavity interface (Fig. 5). For calculations of the stress field while the pressure is still being applied, the effect of the stress σ_r^S is to create a modified pressure p' ($p' = p - \sigma_r^S$). This modified pressure pertains to the selected plastic zone and cavity dimensions, and thereby becomes that indentation pressure (or hardness, H) associated with a plastic zone of relative size β . All stresses should thus be referred to the pressure p' .

For calculations of the residual stress field, it is not permissible to retain a stress at the cavity surface. Hence, in this instance, the stress is eliminated by an iterative scheme, involving

the sequential application of cavity surface pressure and point forces until the residual forces become negligibly small.*

The application of surface forces along a plane bisecting the cavity must also generate shear stresses within the half plane, which will superimpose upon the shear stresses provided by the symmetrical cavity solution (Fig. 5). However, within the plastic zone, the maximum principal shear stress is required to be uniform in order to satisfy the Tresca yield criterion. It is implicit in the calculation, therefore, that the point force solutions result in a constant principal shear stress within this zone. Additional shear stress of significant magnitude would superimpose on those provided by the symmetrical solution; in essence, changing the yield strength of the material, from Y to Y' . The effective yield strength of a material with a relative indentation plastic zone dimension β thus becomes Y' .

The rationale for expecting the Mindlin forces to provide a relatively uniform shear stress in the plastic zone is based upon the observed spherical symmetry of the plastic boundary. The premise must be justified, however, by the results of the calculations. Specifically, the calculations must indicate spherically symmetric contours

* Several different schemes have been attempted previously in order to retain a stress free cavity surface for residual stress field. These schemes include applying a point force at the cavity center, applying forces over a projected circular area of the cavity on the surface, or applying forces over the boundary of this circular area. However, none of the schemes mentioned above give a reasonable residual stress field, i.e., the residual stress field becomes too small or negative everywhere. Hence, they are not further pursued.

of constant shear stress within the plastic zone. It will be demonstrated that these requirements are reasonably well satisfied. Hence, the method of calculation satisfies both boundary conditions: viz., a stress-free surface and an approximately uniform shear stress within the plastic zone. A self-consistent solution can thus be obtained using the proposed approach.

The stress field solutions obtained in the above manner can only be strictly applicable to a hemispherical indentation. The influence of the indenter geometry, although a minor perturbation upon the residual stress field (because the indentation surface is stress free and significant geometric effects would only be manifest in the immediate vicinity of the indentation), can be appreciable at peak load. The origin of the peak load geometry effect is associated with the shape independence of the hardness. As the shape changes (at constant indentation volume) the applied force must also change in order to maintain a constant hardness (Fig. 5). Hence, it is immediately evident that the remote elastic field must change in accord with St. Venant's principle. Presumably, a near field shape dependence can also be expected. It is expedient, therefore, to calculate bounds on the peak load stress field. One bound is provided by the hemispherical cavity solution. The other is given by superimposing onto the residual field the stress field for a half space subject to a force acting at the indentation center (Fig. 5). The magnitude of the force is selected to coincide with that pertinent to the Vickers indenter.

3.2 The Indentation Stress Field

The general form of the stress analysis provides a basis for examining those specific features that relate to the hardness, yield strength, and the incidence of fracture. The two constituents of the indentation stress field are the initial field, provided by the cavity expansion solution, and the free surface modification.

The radial σ_r and tangential σ_t stresses within the initial field are given,¹⁵ during load application by;

$$\begin{aligned}
 \frac{\sigma_r^{pl}}{p} &= \left[\frac{3 \ln(r/a)}{1 + 3 \ln(\beta)} \right] - 1 \\
 \frac{\sigma_t^{pl}}{p} &= \frac{3 [\ln(r/a) + 1/2]}{1 + 3 \ln \beta} - 1
 \end{aligned}
 \left. \vphantom{\begin{aligned} \frac{\sigma_r^{pl}}{p} \\ \frac{\sigma_t^{pl}}{p} \end{aligned}} \right\} \quad (\beta > r/a > 1)$$

$$\begin{aligned}
 \frac{\sigma_r^{el}}{p} &= \frac{-\beta^3}{(r/a)^3 (1 + 3 \ln \beta)} \\
 \frac{\sigma_t^{el}}{p} &= \frac{\beta^3}{2(r/a)^3 (1 + 3 \ln \beta)}
 \end{aligned}
 \left. \vphantom{\begin{aligned} \frac{\sigma_r^{el}}{p} \\ \frac{\sigma_t^{el}}{p} \end{aligned}} \right\} \quad (r/a > \beta)$$
(4)

where the superscripts p and e indicate the plastic and elastic regions, respectively, and r is distance from the cavity center. The equivalent stresses after load removal are;

$$\begin{aligned}
\frac{\sigma_r^{rpl}}{p} &= \left[\frac{3 \ln(r/a)}{1 + 3 \ln(\beta)} \right] - 1 + \frac{1}{(r/a)^3} \\
\frac{\sigma_t^{rpl}}{p} &= \frac{3[\ln(r/a) + 1/2]}{1 + 3 \ln \beta} - 1 - \frac{1}{2(r/a)^3}
\end{aligned}
\left. \vphantom{\begin{aligned} \frac{\sigma_r^{rpl}}{p} \\ \frac{\sigma_t^{rpl}}{p} \end{aligned}} \right\} (\beta > r/a > 1)$$

$$\begin{aligned}
\frac{\sigma_r^{rel}}{p} &= \frac{1}{(r/a)^3} \left[1 - \frac{\beta^3}{1 + 3 \ln \beta} \right] \\
\frac{\sigma_t^{rel}}{p} &= \frac{1}{2(r/a)^3} \left[\frac{\beta^3}{1 + 3 \ln \beta} - 1 \right]
\end{aligned}
\left. \vphantom{\begin{aligned} \frac{\sigma_r^{rel}}{p} \\ \frac{\sigma_t^{rel}}{p} \end{aligned}} \right\} (r/a > \beta)$$
(5)

where σ^r refers to the residual field.

The stresses σ^s created by the surface forces have the general form;

$$\frac{\sigma_{mm}^s}{p} = \int_{\text{plastic}} dA \frac{\sigma_t^j}{p} g_{mm} + \int_{\text{elastic}} dA \frac{\sigma_t^k}{p} g_{mm} \quad (6)$$

where $j = pl$, $k = el$ at peak load, and $j = rpl$, $k = re$ for the residual field, $mm = xx, xz$ or zz , (the stress distribution in cartesian coordinates) or r, t, ϕ , (in spherical coordinates) and g_{mm} are the point force functions summarized in the Appendix II. The final stresses are obtained by the superposition of Eq. (6) and Eq. (4) or (5).

The stresses at the peak load condition deduced by this procedure represent an upper bound, for the radial crack system, as noted above.*

* (For the median crack system, this represents the lower bound peak load stresses.)

Lower bound peak load stresses can be obtained by superimposing onto the residual field the stresses that derive from a point force applied at the center of the indentation.

$$\frac{\sigma_{mm}}{p} = 2(\bar{a})^2 g_{mm} \quad (7)$$

3.2.1 The Modified Pressure and Yield Strength

The radial and tangential stresses induced within the plastic zone by the surface forces result in a pressure modification, which establishes the hardness H of the material, and in a shear stress modification, which dictates the effective yield strength, Y' . The stresses that effect these modifications are σ_r^S and σ_ϕ^S which are given by Eq. (6), evaluated at peak load condition, with $mm = r$ or ϕ .

Taking $\nu=0.25$, the variations of H/p along the cavity interface are plotted in Fig. 6 for several values of β . The relative uniformity of H/p for each β indicates that the requisite constant pressure boundary condition along the indentation interface is satisfied. The indentation pressure can now be directly related to the cavity pressure p , by superposition:*

$$H/p = 1 - \sigma_r^S/p \equiv 1 - m \quad (8)$$

The effective yield strength of the material at any location in the plastic zone is given by:

* (When the specimen is fully unloaded, σ_r^S and m are replaced by σ_r^U and m_r , respectively. The variations of m and m_r with β are plotted in Fig. 8.)

$$Y' = Y + (\sigma_{\phi}^S - \sigma_r^S) \quad (9a)$$

or, expressed in normalised form;

$$\frac{Y'}{H} = \frac{(Y/p) + \sigma_{\phi}^S/p - \sigma_r^S/p}{1 - \sigma_r^S/p} \quad (9b)$$

where σ_{ϕ} is that component of the tangential stress normal to the angle ϕ (Fig. 5). The yield strengths at the indentation interface and at the elastic/plastic boundary are plotted for several β in Fig. 7. It is noted that reasonable uniformity of Y' is retained around each of these contours; although significant fluctuations begin to develop at the larger values of β . Within the uncertainty associated with these fluctuations, the magnitude of Y' is essentially the same at the elastic/plastic boundary and at the indentation interface; and similar to the original value of the yield strength, Y . No significant change in the yield strength can thus be attributed to the creation of the free surface. This relative maintenance of yield strength uniformity probably accounts for the observed hemispherical symmetry of the plastic zone.

The modified ratio of indentation pressure to yield strength thus becomes H/Y , and replaces p/Y for all subsequent analyses. The lower indentation pressure reflects the reduction in constraint induced by the free surface, as anticipated from the indentation plasticity measurements (Figs. 2,3). The modified pressure can be used to reevaluate the relationship between the indentation characteristics, H and β , and the elastic and plastic properties, E and Y , of the material. These

revised curves are plotted on Figs. 2 and 3. A good correlation with the experimental results is apparent. Some justification for the free surface modification deduced by the present analysis is thus established. It is also noted that the present analysis has, for the first time, permitted consistent relationships to be established between all of the indentation variables: the pressure, yield strength, elastic modulus and plastic zone dimensions.

3.2.2 The Stress Field

The general form of the stress field is axisymmetric, but relatively complex. The results presented in this section thus emphasize only the components of the stress field and the spatial locations that relate to the formation of the three dominant crack systems (see Fig. 9): radial cracking (created by the σ_{yy} stress near the free surface and the elastic/plastic boundary), median cracking (dictated by the σ_{yy} stress near the base of the plastic zone), and lateral fracture (dominated by the σ_{zz} stress in the same general vicinity). The stresses are deduced from the general equations (as detailed in the Appendix II) both at peak load and in the fully unloaded conditions, for several values of β .

a. The Radial System

The constituents of the surface tangential stresses, σ_{yy} , derived from the original spherical cavity solution and the modifications afforded by the surface forces are compared in Fig. 10. It is observed that the modification becomes more dominant as the relative plastic zone size β increases. Also, as expected, the modified stress

becomes negligibly remote from the plastic zone. However, the most significant influence of the modification is the enhancement of the peak tension at the elastic/plastic boundary. Also plotted in Fig. 10 are the stresses created by a point force located at the indentation center, used as a constituent of the lower bound stress at peak load. This illustrates both the compressive character of the stresses and their appreciable magnitude in the vicinity of the elastic/plastic boundary (especially for the small plastic zone dimension).

The trends in the resultant stress with β are illustrated in Fig. 13. The peak value of the relative stress σ_{yy}/H diminishes slightly as β increases, whereas the scale of the stress field exhibits a substantial increase. It should be noted that in the original cavity model, the residual tensile stresses are always smaller than the peak load stresses (see Fig. 12). However, the residual tensile stresses, under the present modified cavity model, are generally just in excess of the upper bound tensions, at the peak load. In addition, the equivalent lower bound solution indicates that the tensile stresses at the peak load are further suppressed by indenters with shallow cone angles (particular for materials with small relative plastic zone dimensions). The implication of large residual stresses compared to peak load stresses suggests that radial crack will propagate under residual stress field, which is in accord with the experimental observations. This is justified in Sec. 4.3.a.

The gradient of stress from the surface into the interior of the specimens is also of substantial interest.* The stress, plotted in Fig. 13, is observed to decrease quite rapidly with distance from the surface, particularly for small β .

b. The Median System

The components of σ_{yy} stresses pertinent to median fracture at peak load are plotted in Fig. 14. It is noted that the stresses created by a point force located at the indentation center are larger than the stresses created by surface force modifications. The trends in the resultant σ_{yy} stress (Fig. 15) are similar to those obtained for the radial fracture problem. But, in this instance, the peak load tensile stresses exceed the residual stresses. Also, the peak load stresses are higher for a point force modification contrary to the radial fracture situations. Note that the peak values of the tension are appreciably smaller than the equivalent tangential tensile stresses near the surface for large β values. The stress decreases with distance from the axis (Fig. 16) but the gradient is relatively small, especially for larger values of β .

c. The Lateral System

The magnitudes of the σ_{zz} stresses at various axial locations are plotted in Fig. 17 for $\beta = 2.2$. It is also apparent that the maximum tensions occur at a distance beneath the surface of $\sim\beta/2$. The trends in the stress with β along the planes of maximum tension are

* The surface stress is subject to error when determined by numerical integration. However, the level of the surface stress needed to obtain an accurate assessment of the stress gradient can be determined analytically, as detailed in the Appendix II.

illustrated in Fig. 18. Again a decrease in the relative peak tension with increases in β is evident. However, in this case, the residual tension is appreciably larger than the upper bound tension at the peak load, obtained from the surface force modification, indicating a greater tendency for the development of tension during unloading than encountered with the radial system.

4. IDENTATION FRACTURE

4.1 Crack Propagation

The extension of well developed radial/median cracks has been examined in detail in a recent analysis, based upon the magnitude of the effective residual 'force' exerted by the plastic zone on the surrounding elastic material.⁹ This analysis yields a relation for the crack length that depends upon the relative magnitude β of the plastic zone. The original choice of β was a tentative one based on Hill's¹⁷ spherical cavity solution, $\beta \sim (E/H)^{1/2}$, and gave a crack length relation

$$\frac{K_c}{H\sqrt{a}} \left(\frac{E}{H}\right)^{1/2} = 0.028 (\bar{a}/c)^{3/2} \quad (10)$$

where the numerical quantity is calibrated from experimental results on glass. A more pertinent relation between β and material properties can be derived from the correlation presented in Fig. 2. Using $\beta \sim (E/H)^{2/5}$ appropriate to this figure, Eq. (10) becomes

$$\frac{K_c}{H\sqrt{a}} \left(\frac{H}{E}\right)^{3/5} = 0.021 (\bar{a}/c)^{3/2} \quad (11)$$

The data from Lawn, Evans and Marshall⁹ are plotted according to Eq. (11) in Fig. 19. This plot shows an improved correlation, thus further substantiating the merits of this approach for establishing the extension of well developed radial cracks.

4.2 Fracture Initiation

4.2.1 Observations

The fracture initiation process at indentations is subject to appreciable complexity. The initiation sequence frequently involves two stages; nucleation of small microcracks, followed by the extension of those microcracks suitably located in the general indentation stress field.^{10,11} The nucleation stage may involve microcracking of regions of large localized stress concentration; microcracks have been identified at grain boundaries in polycrystals (presumably at dislocation pile-ups), at slip band intersections in single crystals, and at shear band intersections in glasses.³⁴ Alternatively, pre-existing microcracks may serve as suitable crack nuclei. However, the nucleation phase is not expected to be the critical phase, because non-propagating microcracks are usually observed. The significant step in fracture initiation is thus considered to be the activation of the microcracks by the general indentation field.¹¹

The activation of microcracks by the indentation field is necessarily statistical in nature (particularly if pre-existing microcracks act as nuclei). However, it has been noted that the characteristic behavior of cracks within stress fields of rapid spatial variation (typical of indentation) permits the definition of an absolute fracture initiation minimum load.⁹ Indentation fracture thresholds must exceed the absolute minimum, P_{\min} , by an amount that depends on the probabilistic consideration of microcrack location, size and orientation; large numbers of indentations would allow the lowest initiation load to approach P_{\min} . The minimum threshold is therefore a useful

parameter for establishing initiation trends in processes that involve multiple indentations (e.g., erosion, abrasive wear, machining damage).

The minimum force required to initiate cracks has been studied for a range of materials (see Table VII by Lankford and Davidson,³⁵).

Acoustic emission measurements performed during indentation, coupled with direct observations after indentation (using a Vickers Pyramid) suggested that radial cracks were the first to initiate, and that initiation occurred during loading. Direct observations during initiation of soda-lime glass (using an inverted optical microscope and dry nitrogen experiment, by Marshall and Lawn,⁸ also indicated that the minimum threshold (5N) pertained to radial crack nucleation, but the cracks formed while unloading (Table VII), and in a continuous loading stage, median cracks formed first at 100N load). Since radial cracks always appear to exhibit the lowest threshold, pre-existing surface cracks may be an important source of nuclei. This possibility is investigated in more detail later in this section.

4.2.2 Analysis

The prediction of the minimum threshold involves the systematic estimation of stress intensity factors, k , for cracks of various profiles, centered at different locations, in order to obtain the shape and location that yields the maximum peak value for K . Such a systematic study has not yet been conducted. Instead, it is firstly assumed that a crack centered on the elastic/plastic boundary will experience the largest K , because this is the contour of maximum tension within the indentation field. Then, for simplicity, the crack is considered to exhibit circular symmetry, as suggested by the crack profiles observed

after initiation. Thereafter, the stress intensity factors can be deduced from the stress field by a superposition method. The stress fields of the pertinent locations for median, radial and lateral fracture initiation are not generally axisymmetric, so the computed stress intensity factors would vary around the crack front. A convenient simplification that yields a uniform crack front K is adopted. This averts appreciable calculational complexity without detracting significantly from the prediction of behavioral trends. The procedure consists of the determination of an effective axisymmetric stress σ_{eff} at each radial location, assumed to be equal to the stress (at that location) averaged over the full angular range, 0 to 2π . The stress intensity factor can then be derived from the superposition solution;

$$K = 2\left(\frac{c}{\pi}\right)^{1/2} \int_0^1 \frac{\sigma_{eff}(r/c)d(r/c)}{\sqrt{1 - (r/c)^2}} \quad (12)$$

The effective stress normalized by the hardness, can be adequately represented by a polynomial

$$\sigma_{eff}/H = a_0 - a_1(r/a) + a_2(r/a)^2 + \dots \quad (13)$$

where the parameters a_0 , a_1 (both positive) and a_2 (either positive or negative) are dependent on the relative plastic zone size β . Representative values of a_0 , a_1 , and a_2 for materials with several different β values are shown in Table II. Insertion of Eq. (13) into Eq. (12), followed by integration yields the result:

$$\begin{aligned}
K/(H\sqrt{a}) &= f(\delta) \\
&= 2(\delta/\pi)^{1/2} [a_0 - (\pi a_1/4)\delta + (2a_2/3)\delta^2 + \dots] \quad (14)
\end{aligned}$$

where $\delta = c/a$. This relation exhibits a peak, $f(\delta^*)$, in the stress intensity factor (when $dK/dc = 0$). This peak coincides with a specific relative crack length, given by (neglecting coefficients a_n , with $n \geq 3$)

$$\delta^* = (3/80a_2) \left[3\pi a_1 - \sqrt{9\pi^2 a_1^2 - 640 a_0 a_2/3} \right] \quad (15)$$

The values of δ^* and $f(\delta^*)$ for a range of β values at either loading or unloading conditions are given in Table III, IV, and V. A minimum threshold occurs when the peak value of K attains K_c . The crack length at the minimum threshold is

$$c^* = \delta^* \bar{a}_{\min} = \delta^* [K_{IC}/H f(\delta^*)]^2 \quad (16)$$

and the threshold load for a Vickers pyramidal indenter becomes

$$P_{\min} = 2H\bar{a}_{\min}^2 = 2H[K_{IC}/H f(\delta^*)]^4/(0.45)^2 \quad (17)$$

The results summarized in Eqs. (16) and (17) reduce to the Lawn and Evans¹¹ result when a_2 is set to zero. It is also noted that the other difference between the Lawn and Evans study and the present analysis is that the former used only order-of-magnitude estimates of a_0 and a_1 which are based on the unmodified spherical cavity solution.

4.2.3 Results

The predicted threshold crack lengths are the threshold loads for three crack systems at either loading* or unloading conditions are given in Table III, IV, and V. Based on these results, it can be found that the trends in the threshold with material toughness and hardness are thus essentially the same as those elucidated in the earlier study, except that an additional influence of E/H emerges through the influence of the relative plastic zone size β . This additional influence is illustrated in Fig. 20 for the median and the radial systems. It is noted that the minimum normalized threshold load decreases as β increases, causing a relative diminution of the threshold as the extent of plasticity increases. The same trend can also be found in the lateral system.

The minimum threshold loads for the three crack types (radial, median, lateral), predicted for materials with a range of β values, are shown in Table VI. The calculations are referred to the Vickers geometry. Radial cracks exhibit the lowest thresholds and lateral cracks the largest. The median cracks invariably exhibit their lower threshold during loading; while the lateral crack threshold always prevails during the unloading cycle. The occurrence of the radial crack threshold depends upon the indentation geometry. For those configurations that yield to the upper bound stress field, the threshold could occur

* The predicted loading threshold values are based on the upper bound loading stresses for the radial cracks and the lower bound stresses for the median cracks.

during loading or unloading, by virtue of the similarity in the threshold condition. However, shallow indentation geometries, which are best represented by the lower bound stress, favor radial crack formation during unloading. This situation is particularly significant in solids with small β values such as glass. Observations of indentation on glass by Lawn and Marshall⁸ confirm the above statement.

a) Radial Crack Initiation

Observed radial crack threshold conditions are compared with predictions in Table VII. Good agreement is shown for Ge, Si, Al_2O_3 and ZnS. The observed threshold for NaCl appears to be lower than predicted. However, as noted by Lankford and Davidson,³⁵ the NaCl threshold is sensitive to crystallographic orientation; the lower value listed in Table VII corresponds to cracks parallel to $\langle 110 \rangle$. Radial cracks that form along the cleavage plane (001) could not be nucleated in other orientations, within the available range (60N). The $\langle 110 \rangle$ cracks in NaCl (and other ionic solids) are coincident with the primary slip bands that occur outside the generalized plastic zone. The cracks result from an enhancement of the local stress by the stress field of the dislocations, and a threshold appreciably smaller than that associated with the generalized deformation is to be anticipated.

The observed thresholds for glass are an order of magnitude higher than predicted. This observation suggests that the precursor flaw density is too small to permit an appreciable sampling of flaws of the requisite size, at the minimum threshold load. Elevation of the observed threshold above the absolute minimum is not generally observed

and hence, its occurrence in glass requires an explanation. A plausible interpretation emerges when the radial crack precursors are considered to be pre-existent surface located microcracks. Then, surfaces prepared by mechanical procedures are likely to exhibit high density of surface cracks and the absolute minimum threshold should be closely approached. This condition pertains for the tests performed on Si, Ge, ZnS and Al_2O_3 . However, for surfaces prepared without deliberate mechanical interaction (such as glass surfaces) appreciably lower surface crack densities might be expected, and some elevation above absolute minimum might be anticipated. The excess threshold load can be quantified (in terms of the availability of pre-existing nucleating flaws) by adapting some existing statistical data for surface flaws in glass.³⁶ The statistical analysis firstly invokes the characteristic variation in stress intensity factor with crack length in order to determine the pre-existing crack radius c_i (Fig. 21). Inspection of the trends in stress intensity factor indicates a rapid increase on K at small flaw lengths (up to the maximum). Relatively small deviations of the pre-existing flaw size below c^* would thus substantially elevate the observed threshold, in qualitative accord with the observation for glass. The radius of the pre-existing radial crack nucleus, c_i , can be directly deduced from the K curve by superimposing the ratio of the measured final radial crack length, c_f , and the indentation diagonal, $2\bar{a}_f$, as indicated on Fig. 23. The flaw radius pertinent to samples tested in air ($c_f = 17$

at $a_f = 10\mu\text{m}$) is determined to be $c_i = 0.5\mu\text{m}$, i.e., $\sim c^*/2$. The probability of locating flaws of this magnitude within the indentation field at the threshold load can now be estimated from the surface flaw density data. The flaw density data are described in terms of the quantity $g(S)dS$, which is the number of surface flaws in unit area with a strength between S and $S + dS$. An approximate linear fit to the density function, obtained from Ref. 36, gives;

$$\log[g(s)] = 2.9(S/S_{\max}) - 2.4 \quad (18)$$

where $S_{\max} = 8.7 \times 10^8 \text{ Pa}$. The number of surface flaws with a strength S existing in an area ΔA ($\Delta A = \pi(r_2^2 - r_1^2)$) is thus;

$$G(S) = \Delta A \int_0^S g(S) dS \quad (19)$$

The strength of a surface flaw is related to its radius by;

$$S = \frac{\sqrt{\pi}}{2.5} \frac{K_c}{\sqrt{c}} \quad (c) \quad (20)$$

The number of flaws with radius $\geq c$ in the area A is thus;

$$G(c) = \Delta A \int_0^{0.71 \frac{K_c}{\sqrt{c}}} g(S) dS \quad (21)$$

At the observed threshold load (5N) the area of surface subject to significant residual tension is $3 \times 10^{-9} \text{m}^2$.^{*} The expected number of flaws in the tensile zone (at initiation) with a size $>0.5 \mu\text{m}$ thus becomes ~ 0.1 . This is sufficiently close to the required value of unity (considering the approximate nature of the flaw statistics, the tensile area sampled and the unknown relative influences of subcritical crack growth in the air environment) that the statistical description is considered to provide a reasonable interpretative description of the excess threshold load.

Finally, the predicted radial crack thresholds for some polycrystalline materials are shown in Table VIII. It is noted that, because the threshold crack dimension for most of the materials is approximately equal to, or smaller than, the grain size, single crystal material properties (H , E and K_{IC}) would normally provide a more appropriate basis for prediction. The sensitivity to the choice of material parameters is illustrated by comparing the predictions for Al_2O_3 in Table VII (based on single crystal material properties) and Table VIII (based on polycrystal material properties). The prediction in Table IV represents an order-of-magnitude overestimate of the observed threshold. A similar overestimate is apparently obtained for SiC , since the predictions in Table VIII exceed the experimental measurements (Lankford and Davidson)³⁵ by a factor of

^{*} The area is estimated by taking $r_1 = 2a$ and $r_2 = 4a$.

~ 10 ($p^* = 0.1\text{N}$, $c^* = 1.0\mu\text{m}$). Hence, a more pertinent prediction of the threshold cannot be performed at the juncture.

b) Median Crack Initiation

It was discussed in Section 4.2.3 that radial crack may initiate either during loading or unloading conditions, depending on the indentation geometry. In the median crack system, it was shown in Fig. 17 that the loading stresses, regardless of the indenter geometry, are always higher than the unloading stresses. Hence, median cracks always initiate during loading as confirmed by experimental observations. In addition, when shallow indentation geometry is favored for indentation on very brittle solids, i.e., small β values, the stress needed to initiate median cracks during loading are higher than the stress needed to initiate radial cracks during unloading, indicating that the median cracks will initiate first during loading.

This was confirmed by the experimental observation on glass. When the load was increased to 100N during loading, median cracks were found to initiate first with no indication of radial crack formation. However, the statistical analysis is again anticipated to account for the big difference in terms of threshold load prediction (see Table IV) and the experimental observations. In addition, because the flaw density of the glass is less inside the bulk material than on the surface,[†]

[†] Glass surface is easily subjected to damage by handling or environmental effect.

a higher load is expected for median crack formation than for radial crack formation. Hence, the prediction can become meaningful only if the flaw density distribution is also considered.

c) Lateral Crack Initiation

The results in Table V indicated that lateral cracks always initiate first during the unloading cycle. The considerable load needed to initiate lateral cracks ensures that these cracks are the last to initiate among the three crack types. The predicted threshold results also indicated that lateral cracks may not initiate from the bottom of the plastic zone, contrary to the general expectations. Observations of indentations on Si and ZnS supported the prediction that lateral cracks were found away from the bottom of the plastic zone. However, these were also observations indicating that lateral cracks were found consistently to initiate from the bottom of the plastic zone, e.g., in soda lime glass. Explanation of the observation requires further analysis.

There are several reasons to account for this discrepancy. First, the present analysis is based on mode I crack formation only. At the bottom of the plastic zone, a lateral crack experiences triaxial stresses where the stresses along the other two orthogonal directions are much higher than σ_{zz} stress used for mode I crack initiation. Under a triaxial stress state, the threshold load and the threshold crack length reduce significantly. Secondly, since the median cracks initiate at a much lower load than the lateral cracks, they can, in turn, act as a source to nucleate the lateral cracks. This is also supported by the observation showing the median crack may deflect its

direction to become a lateral crack. Thirdly, lateral cracks generally follow the principal stress trajectory in uncracked solid, thus either propagating toward or away from the surface. This non-planar effect further complicates the problem. A comprehensive analysis considering all these effects are the subject for future studies.

5. CONCLUSIONS

Indentation plasticity has been examined by adapting the notions that the volume of the plastic zone and the work of plastic penetration are both dictated by indentation volume. The indentation problem can then be solved by reference to a common hemispherical indentation geometry. This geometry is related to the pressurized cavity problem solved by Hill, modified to account for the reduced constraint in the presence of the free surface. A simple hemispherical modification of the Hill solution has been developed which indicates the essential relationships between indentation plasticity and the dominant material properties: notably, yield strength, hardness, elastic modulus and Poisson's ratio. Predictions of the plastic zone dimension in terms of the hardness and elastic modulus have been shown to correlate with experimental observations for a wide range of materials. Similarly, predictions of the trend in the yield strength/hardness ratio with the elastic modulus and hardness correspond closely to the trends demonstrated by the available experimental data.

The concept has also been used to calculate the tensile stress fields generated around indentations, as a basis for predicting the initiation of indentation fractures. The presence of the free surface allows tensile stresses to be developed, during loading or while unloading, that are qualitatively consistent with observations of the three principal crack types: radial, median and lateral. The stress fields have been used to predict fracture initiation thresholds for the three crack systems. The radial cracks were anticipated to exhibit the lowest threshold loads, as observed experimentally. Comparison

of the predicted radial crack threshold loads with experimental results indicate satisfactory correlations for surfaces containing a sufficient density of pre-existent crack initiation sites. This condition was not satisfied for glass surfaces and the experimentally observed threshold was appreciably in excess of the prediction. The excess threshold was rationalized by invoking the weakest link flaw statistics concepts, using data obtained for comparable glass surfaces. The median cracks were found to initiate first during loading, the lateral cracks were the last to initiate during unloading. All these predictions are consistent with the experimental observations.

FUTURE WORK

The complexity of the elastic/plastic deformation has been demonstrated throughout the above studies. Although the present approach successfully addressed several important issues in the area of indentation plasticity and indentation fracture, there is still a definite need to expend effort in the following areas:

a) The spherical cavity solution used in this study does not allow the consideration of work hardening. However, most materials, including ceramics, exhibit work hardening. Further work should adapt a superior spherical cavity model that includes work hardening.

b) The present computer program, using Simpson's equation to calculate the double integral, is not very accurate when the free surface effects on the yield strength, and on the stresses near the surface are concerned. It appears that a finite element scheme is necessary in order to address this problem.

c) In the fracture initiation studies, the crack shape and the crack position has been chosen in advance to construct the stress intensity factor. A more realistic approach should allow these parameters to vary independently.

d) When the fracture initiation threshold is studied, the grain size effect, orientation influence, and the flaw density distribution should be carefully examined before making prediction.

e) The problem associated with the lateral crack initiation, i.e., a triaxial stress state, effect of the preexisting median crack, and the non-planar nature of the lateral crack, should be addressed in order to make reasonable predictions.

f) The present approach treated the crack initiation and propagation separately. The ultimate goal in the future studies is to extend the crack initiation analysis to crack propagation.

APPENDIX I

The Relationship Between a and \bar{a} Under
Equivalent Volume Condition

The transformation of the indentation volume for a specific indenter to a reference hemispherical geometry is given as follows for three different indenters:

A. Pyramidal Indenter (Fig. 22a)

The volume of a pyramid V_p is given by:

$$V_p = \frac{1}{3} \left(2 \cdot \frac{\bar{a}^2}{\sqrt{2}} \right) \cdot z \quad (A-1)$$

$$\text{where } z = \bar{a} \cot \psi \quad (A-2)$$

Combining (A-1) and (A-2)

$$V_p = \frac{2}{3} \bar{a}^3 \cot \psi$$

For equivalent hemispherical volume, V_h , with radius a :

$$\frac{2}{3} \pi a^3 = \frac{2}{3} \bar{a}^3 \cot \psi \quad (A-4)$$

The relationship between a and \bar{a} then reduces to:

$$a = \bar{a} \left(\frac{\cot \psi}{\pi} \right)^{1/3} \quad (A-5)$$

For Vickers indenter, $\psi = 74^\circ$, and $a = 0.45\bar{a}$.

B. Conical Indenter (Fig..22b)

The volume of a conical indenter is given by:

$$V_c = \frac{1}{3} \pi \bar{a}^2 \cdot z \quad (A-6)$$

$$\text{where } z = \bar{a} \cot \Psi \quad (A-7)$$

The relationship between a and \bar{a} is given, combining (A-6), (A-7) and let $V_h = V_c$, by

$$a = \bar{a} \left(\frac{\cot \Psi}{2} \right)^{1/3} \quad (A-8)$$

C. Brinell Indenter (Fig. 22c)

The indentation volume; V_s , for a spherical indenter is given by:

$$V_s = \frac{4}{3} \pi R^3 \left(\frac{S_0}{4\pi} \right) - \frac{1}{3} \pi \bar{a}^2 (R \cos \theta_0) \quad (A-9)$$

where R is the radius of the spherical indenter, \bar{a} is the radius of the resulting impression, and S_0 is the solid angle. S_0 can be further expressed as:

$$S_0 = \int_0^\Psi \frac{2\pi R \sin \Psi \, d\Psi}{R^2} = 2\pi (1 - \cos \Psi) \quad (A-10)$$

The relationship between a and \bar{a} is given, combining (A-9), (A-10), and let $V_s = V_a$, by:

$$a = R \left[1 - \frac{3}{2} \cos \Psi + \frac{1}{2} \cos^3 \Psi \right]^{1/2} \quad (\text{A-11})$$

$$\text{where } \cos \Psi = \sqrt{R^2 - \bar{a}^2/R} \quad (\text{A-12})$$

APPENDIX II

Detailed Expressions for Indentation Stress Field DeterminationI. The Point Force Solution

A semi-infinite elastic homogenous solid is considered to be bounded by the plane $z = 0$, the positive z axis penetrating into the body. For a point force p applied at point $(0,0,0)$ and acting in the positive z direction, the stress distribution at a point (x,y,z) inside the semi-infinite body has been determined by Mindlin³³. The solutions are;

$$\sigma_{xx} = pg_{xx}$$

$$\sigma_{yy} = pg_{yy}$$

$$\sigma_{zz} = pg_{zz}$$

$$\sigma_{xz} = pg_{xz}$$

where

$$g_{xx} = \frac{z}{2\pi R^3} \left[1 - 2\nu - 3\left(\frac{x}{R}\right)^2 - \frac{1-2\nu}{(R+z)^2} \left(R^2 - x^2 + \frac{R}{z} (R^2 - 2x^2) \right) \right]$$

$$g_{yy} = \frac{z}{2\pi R^3} \left[1 - 2\nu - 3\left(\frac{y}{R}\right)^2 - \frac{1-2\nu}{(R+z)^2} \left(R^2 - y^2 + \frac{R}{z} (R^2 - 2y^2) \right) \right]$$

$$g_{zz} = - 3z^3/2\pi R^5$$

$$g_{xz} = - 3xz^2/2\pi R^5$$

here $R^2 = x^2 + y^2 + z^2$ and ν is Poisson's ratio.

In terms of spherical coordinates (r, θ, ϕ) , for simplicity, let the point (x, y, z) lie on the xz plane, (i.e., set $y = 0$), then:

$$g_r = g_{xx} \cos^2 \phi + g_{zz} \sin^2 \phi + 2g_{xz} \sin \phi \cos \phi$$

$$g_\theta = g_{xx} \sin^2 \phi + g_{zz} \cos^2 \phi + 2g_{xz} \sin \phi \cos \phi$$

$$g_\phi = g_{yy}$$

II. The Stress Relations for the Three Crack Systems

1. The Radial System

The components of the σ_{yy} stress, along the surface ($\zeta=0$) pertinent to radial fracture, are given at peak load, for the upper bound, by* ($\zeta=0$);

$$\begin{aligned} \frac{\sigma_{yy}^{pl}}{H} &= \frac{1}{(1-\nu)} \left[\frac{3\ell n\Omega + 3/2}{1+3\ell n\beta} - 1 \right] \\ \frac{\sigma_{yy}^{el}}{H} &= \frac{1}{(1-\nu)} \left[\frac{\beta^3}{2\Omega^3(1+3\ell n\beta)} \right] \end{aligned} \quad (B1)$$

where $\Omega = x/a$

$$\begin{aligned} \frac{\sigma_{yy}^s}{H} &= \frac{2}{(1-\nu)} \int_1^\beta \int_0^\pi a^2 \xi d\xi d\theta \left(\frac{\sigma_t^{pl}}{p} \right) g_{yy} + \int_\beta^\infty \int_0^\pi \\ &\quad a^2 \xi d\xi d\theta \left(\frac{\sigma_t^{el}}{p} \right) g_{yy} \end{aligned} \quad (B-2)$$

*The greek letters represent distances normalized with respect to the cavity radius a (Fig. 23).

where

$$g_{yy} = \frac{\zeta}{2\pi a^2 \gamma^3} \left[1 - 2\nu - 3 \left(\frac{\eta}{\gamma} \right)^2 - \frac{1-2\nu}{(\gamma+\zeta)^2} \left(\gamma^2 - \eta^2 + \frac{\gamma}{\zeta} (\gamma^2 - 2\eta^2) \right) \right]$$

$$\nu = \xi \sin \theta$$

$$\gamma^2 = \xi^2 + \Omega^2 + \zeta^2 - 2\xi\Omega \cos \theta$$

At peak load, for the lower bound;

$$\frac{\sigma_{yy}^s}{H} = \frac{-(1-2\nu)}{(1-m)\Omega^2} \quad (B-3)$$

At full unload ($\xi = 0$)

$$\frac{\sigma_{yy}^{rpl}}{H} = \frac{1}{(1-m)} \left[\frac{3\ell n\Omega + 3/2}{1+3\ell n\beta} - 1 - \frac{(1-2m_r)}{2\Omega^3} \right]$$

$$\frac{\sigma_{yy}^{rel}}{H} = \left[\frac{1}{2(1-m)\Omega^3} \frac{\beta^3}{1+3\ell n\beta} - 1 + m_r \right] \quad (B-4)$$

where m_r is the term that permits creation of a stress free indentation surface (Fig. 8) as obtained by an iteration technique.

2. The Median System

The components of the σ_{yy} stress pertinent to the median fracture problem are not very different from the σ_{yy} stress relevant to

radial fracture. At peak load σ_{yy}^{Pl}/H and σ_{yy}^{el}/H bear the same form as Eq. (B1), except that Ω is replaced by ζ (the median crack propagates along the plane $\Omega = 0$), and σ_{yy}^S/H is the same as Eq. (B-2), except that γ^2 becomes $\gamma^2 = \xi^2 + \zeta^2$. In addition, Eq. (B-2) in the median system represents the lower bound loading stress while Eq. (B-3) represents the upper bound. At full unload, the same change should be made, i.e., replaced by ζ , in Eq. (B4).

3. The Lateral System

The components of the σ_{zz} stress that pertain to the lateral fracture problem are, at peak load, for the upper bound;

$$\frac{\sigma_{zz}^{Pl}}{H} = \frac{1}{(1-m)} \left[\frac{3\ln(\Omega^2 + \zeta^2)}{2(1+3\ln\beta)} + \frac{3\Omega^2}{2(1+3\ln\beta)(\Omega^2 + \zeta^2)} - 1 \right]$$

$$\frac{\sigma_{zz}^{el}}{H} = \frac{1}{(1-m)} \left[\frac{\beta^3}{(\Omega^2 + \zeta^2)^{5/2}(1+3\ln\beta)} \left(\frac{\Omega^2}{2} - \zeta^2 \right) \right] \quad (B-5)$$

σ_{zz}^S/H exhibits the same form as Eq. (B-2) except that g_{yy} is replaced by g_{zz} , where $g_{zz} = -3\zeta^3/2\pi a^2 \gamma^5$ and $\zeta = z/a$.

At peak load, for the lower bound,

$$\frac{\sigma_{zz}^S}{H} = - \frac{3\zeta^3}{(1-m)(\Omega^2 + \zeta^2)^{5/2}} \quad (B-6)$$

At full unload

$$\frac{\sigma_{zz}^{rpl}}{H} = \frac{1}{(1-m)} \left[\frac{3\ell n(\Omega^2 + \zeta^2)}{2(1+3\ell n\beta)} + \frac{3\Omega^2}{2(1+3\ell n\beta)(\zeta^2 + \Omega^2)} + \frac{(\zeta^2 - \Omega^2/2)}{(\zeta^2 + \Omega^2)} (1-m_r) - 1 \right]$$

$$\frac{\sigma_{zz}^{rel}}{H} = \frac{1}{(1-m)} \left[1 - m_r - \frac{\beta^3}{1+3\ell n\beta} \right] \frac{(\zeta^2 - \Omega^2/2)}{(\zeta^2 + \Omega^2)^{5/2}} \quad (B-7)$$

III. Analytic Solution for the Surface Stresses

At full load, the modification to the tangential stress on the surface (responsible for radial cracking) created by the free surface is;

$$\frac{\sigma_{yy}^s}{H} = \frac{2}{(1-m)} \int_1^\beta \int_0^\pi a^2_\xi d\xi d\theta \frac{\sigma_t^{pl}}{H} (g_{yy})$$

$$+ \int_\beta^\infty \int_0^\pi a^2_\xi d\xi d\theta \frac{\sigma_t^{el}}{H} (g_{yy}) \quad (B-8)$$

When $\zeta = 0$,

$$g_{yy} = \frac{(1-2\nu)}{2\pi\gamma a^2} [\zeta^2 + \Omega^2 - 2\zeta\Omega \cos\theta - 2\zeta^2 \sin^2\theta] \quad (B-9)$$

Substituting Eq. (B-9) into Eq. (B-8) the stress becomes:

$$\frac{\sigma_{yy}^s}{H} = \frac{(1-2\nu)}{\pi(1-m)} \left[\int_1^\beta (-A) \frac{\sigma_t^{pl}}{H} \xi d\xi + \int_\beta^\infty (-A) \frac{\sigma_t^{el}}{H} \xi d\xi \right] \quad (B-10)$$

where

$$A = \int_0^\pi \frac{\xi^2 + \Omega^2 - 2\xi\Omega \cos\theta - 2\xi^2 \sin^2\theta}{(\xi^2 + \Omega^2 - 2\xi\Omega \cos\theta)^2} d\theta = \begin{cases} \frac{\pi}{2} & (\Omega^2 > \xi^2) \\ 0 & (\xi^2 > \Omega^2) \end{cases}$$

if $\Omega < \beta$

$$\frac{\sigma_{yy}^s}{H} = \frac{(1-2\nu)}{(1-m)\Omega^2} \left\{ \frac{3}{1+3\ln\beta} [\Omega \ln \Omega - (1/2)(\Omega-1)] - (\Omega-1) \right\} \quad (B-11)$$

if $\Omega > \beta$

$$\frac{\sigma_{yy}^s}{H} = \frac{(1-2\nu)}{(1-m)\Omega^2} \left\{ \frac{1}{1+3\ln\beta} \left[3\beta \ln\beta - 1/2\beta + 3/2 - \frac{\beta^3}{4\Omega^2} \right] - (\beta-1) \right\} \quad (B-12)$$

At full unload, if $\Omega < \beta$

$$\frac{\sigma_{yy}^s}{H} = \frac{(1-2\nu)}{(1-m)\Omega^2} \left\{ \frac{3}{1+3\ln\beta} [\Omega \ln \Omega - (1/2)(\Omega-1)] + \frac{1-m_r}{4} \left(\frac{1}{\Omega^2} - 1 \right) \right\} \quad (B-13)$$

if $\Omega > \beta$

$$\begin{aligned} \frac{\sigma_{yy}^s}{H} = \frac{(1-2\nu)}{(1-m)\Omega^2} \left\{ \frac{1}{1+3\ln\beta} \left[3\beta \ln\beta - 1/2\beta + 3/2 - \frac{\beta^3}{4\Omega^2} \right] \right. \\ \left. - (\beta-1) - (1-m_r) \left(\frac{1}{\Omega^2} - 1 \right) \right\} \end{aligned} \quad (B-14)$$

REFERENCES

1. Ruff, A. W. and Widerhorn, S. M. (1979), "Treatise on Materials Science and Technology, Vol. 16, Erosion," Academic Press, 69-126.
2. Evans, A. G. (1979), "Treatise on Materials Science and Technology, Vol. 16, Erosion," Academic Press, 1-67.
3. Koepke, B. G. and Stokes, R. J. (1979), Science of Machining and Surface Finishing II, NBS Special Technical Publication: 561, p. 75-92.
4. Evans, A. G. (1979), "Science and Ceramic Machining and Surface Finishing II," NBS Special Technical Publication: 562, p. 1-14.
5. Marshall, D. B., Lawn, B. R., and Mecholsky, J. J. (1980), J. Amer. Ceram. Soc., 63, 358-360.
6. Marshall, D. B., Lawn, B. R., and Chantikul, P. (1979), J. Mater. Sci., 14, 2225-2235.
7. Lawn, B. R. and Fuller, E. R. (1975), J. Mater. Sci., 10, 2016-2024.
8. Marshall, D. B. and Lawn, B. R. (1979), J. Mater. Sci., 14, 2001-2012.
9. Lawn, B. R., Evans, A. G., and Marshall, D. B. (1980), J. Amer. Ceram. Soc., 63, 574-581.
10. Evans, A. G. and Wilshaw, T. R. (1976), Acta Metall., 24, 939-956.
11. Lawn, B. R., and Evans, A. G. (1977), J. Mater. Sci., 12, 2195-2199.
12. Samuels, L. E. and Mulhearn, T. O. (1957), J. Mech. Phys. Solids, 5, 125-134.
13. Mulhearn, T. O. (1959), J. Mech. Phys. Solids, 7, 85-96.

14. Hill, R., Lee, E. H., and Tupper, S. J. (1947), Proc. Roy. Soc. A188, 273.
15. Grunzweig, J., Longman, I. M., and Petch, N. J. (1954), J. Mech. Phys. Solids, 2, 81-86.
16. Haddow, J. B. and Johnson, W. (1961), Int. J. Mech. Sci. 3, 229-238.
17. Hill, R. (1950), "The Mathematical Theory of Plasticity," Oxford: Clarendon Press.
18. Atkins, A. G. and Tabor, D. (1965), J. Mech. Phys. Solids, 13, 149-164.
19. Dugdale, D. S. (1958), J. Mech. Phys. Solids, 6, 85-91.
20. Marsh, D. M. (1964), Proc. Roy. Soc. A279, 420-435.
21. Johnson, K. L. (1970), J. Mech. Phys. Solids, 18, 115-126.
22. Evans, A. G., Gulden, M. E., and Rosenblatt, M. E. (1978), Proc. Roy. Soc., A361, 343-365.
23. Hagan, J. T. and Swain, M. V. (1978), J. Phys. D: Appl. Phys. 11, 2091-2102.
24. Burlingame, N. H. (1980), M. S. Thesis, University of California, Berkeley.
25. Chiang, S. S., Marshall, D. B., and Evans, A. G. (1980). In preparation.
26. Hirst, W. and Howse, M.G.J. (1969), Proc. Roy. Soc. A311, 429-444.
27. Puttick, K. E., Smith, L.S.A., and Miller, L. E. (1977), J. Phys. D: Appl. Phys., 10, 617-632.

28. Hardy, C., Baronet, C. H., and Tordion, G. V. (1971), Int'l Jnl. Num. Methds. Eng., 3, 451-462.
29. Perrot, C. M. (1977), Wear, 45, 293-309.
30. Evans, A. G. (1979c), "Fracture Mechanics Applied to Brittle Materials," ASTM STP 678, 112-135.
31. B. De Saint Venant, see Timoshenko, S. and Goodier, J. N. (1950), "Theory of Elasticity," (McGraw Hill), 39-40.
32. Boussinesq, J., see Timoshenko, S. and Goodier, J. N. (1950), "Theory of Elasticity," (McGraw Hill), 398-402.
33. Mindlin, R. D. (1936), Physics, 7, 195-202.
34. Hagan, J. T. (1979), J. Mat. Sci. 14, 462-466.
35. Lankford, J. and Davidson, D. L. (1979), J. Mater. Sci., 14, 1662-1668.
36. Matthews, J. R., McClintock, F. A. and Shack, W. J. (1976) J. Amer. Ceram. Soc. 59, 304-308.
37. Jaccodine, R. J. (1963), J. Electrochem. Soc. 6, 524-527.
38. Lawn, B. R. and Wilshaw, T. R. (1975), "Fracture of Brittle Solids," Cambridge University Press.
39. Rai, C. S. and Manghnani, M. H. (1976), J. Amer. Ceram. Soc., 59, 499-502.
40. Freiman, S. W., McKinney, K. R., and Smith, H. L. (1978), in Fracture Mechanics of Ceramics (Eds., Bradt, R. C., Hasselman, D.P.H., and Lange, F. F.), Plenum Press, New York, 657-676.

Table I. Normalized Plastic Zone Size (β) and Material Properties

Materials	K_{Ic} MPa \sqrt{m}	H GPa	E GPa	β theory	β experiment
Soda lime glass ⁽¹⁾	.75	5.5	70	2.3	2.2 ⁽¹⁾
Ge ⁽²⁾	.5	9	140	2.5	
B ₄ C ⁽⁴⁾	6.0	32.2	500	2.5	
Al ₂ O ₃ ^{(s.c.)(5)}	2.2	23	400	2.5	
Al ₂ O ₃ +42v/o ZrO ₂ ⁽³⁾	6.5	15	264	2.6	2.5 ⁽³⁾
ZrO ₂ (PSZ) ⁽⁴⁾	6.9	11.4	170	2.6	
Si ^{(s.c.)(1)}	.7	9	168	2.65	
SiC ^{(h.p.)(4)}	4.0	19.3	420	2.8	
Si ₃ N ₄ ^{(h.p.)(4)}	4.9	14.1	320	2.8	
MgO ⁽⁶⁾	1.2	9.3	240 ^(6a)	3.0	
MgF ₂ ⁽⁶⁾	0.9	5.8	140 ^(6b)	3.0	
Al ₂ O ₃ ^{(h.p.)(6)}	4.1	12.0	393 ^(6c)	3.0	
ZnS ⁽¹⁾	1.0	1.9	103	4.0	3.0 ⁽¹⁾
ZnS ⁽⁷⁾	1.0	3.8 ^(7a)	103	3.1	2.65 ^(7a)
ZnSe ⁽⁴⁾	.9	1.0	68	4.4	

Table I. (Continued)

Cold rolled steel ⁽⁸⁾		3.4	200	4.6	4.5 ⁽⁸⁾
NaCl ⁽⁶⁾	.4	.24	43 ^(6a)	6.3	
Hot rolled brass ⁽⁸⁾		.47	110	7.0	7.0 ⁽⁸⁾

(s.c) = single crystal

(h.p) = hot pressed

- | | |
|----------------------------------|---|
| (1) Lawn, Evans and Marshall (9) | (6a) Lawn and Wilshaw (38) |
| (2) Lankford and Davidson (34) | (6b) Rai and Manghnani (39) |
| (2a) Jaccodine (37) | (6c) Freiman, Mickinney and Smith (40) |
| (3) Burlingame (24) | (7) Dynamic Impact, estimated value (2) |
| (4) Evans (30) | (7a) Computer simulated result Evans (30) |
| (5) Evans and Wilshaw (10) | (8) Mulhearn (13) |
| (6) Lawn and Evans (11) | |

Table II. Numerical Constants from Polynominal Curve Fitting

<u>RADIAL SYSTEM</u>						
PEAK LOAD				RESIDUAL		
β	a_0	a_1	a_2	a_0	a_1	a_2
2.2	.18	.19	-.028	.17	.23	-.007
2.5	.17	.19	-.031	.17	.18	-.006
2.65	.17	.14	-.012	.17	.12	-.005
2.8	.17	.15	.003	.17	.14	-.018
3.0	.17	.13	-.004	.17	.11	-.026
3.3	.16	.11	-.005	.17	.10	-.018
4.0	.16	.08	-.007	.16	.07	-.014
4.4	.15	.06	-.007	.15	.05	-.013
7.0	.14	.03	-.002	.14	.03	-.003

<u>MEDIAN SYSTEM</u>						
PEAK LOAD				RESIDUAL		
β	a_0	a_1	a_2	a_0	a_1	a_2
2.2	.15	.12	-.08	.12	.10	-.13
2.5	.14	.12	-.03	.11	.07	-.10
2.65	.14	.11	-.03	.12	.10	-.05
2.8	.13	.10	-.02	.12	.10	-.03
3.0	.13	.09	-.02	.11	.05	-.06
3.3	.12	.07	-.02	.11	.07	-.02
4.0	.11	.05	-.01	.10	.05	-.01
4.4	.10	.05	-.009	.10	.04	-.01
7.0	.09	.02	-.004	.09	.03	-.003

Table II (Continued)

LATERAL SYSTEM						
PEAK LOAD				RESIDUAL		
$\zeta \backslash \beta=2.2$	a_0	a_1	a_2	a_0	a_1	a_2
0.6	.075	-.088	-.03	.10	-.10	.001
1.0	.066	-.11	-.015	.12	-.12	-.001
2.2				.02	-.01	-.007
$\zeta \backslash \beta=2.8$						
1.0	.078	-.086	-.003	.10	-.06	-.02
$\zeta \backslash \beta=4.0$						
2.0	.07	-.04	-.007	.085	-.038	-.004

Table III. Radial Crack Initiation Threshold Prediction

β	MATERIAL	LOADING [†] CONDITION	δ^*	$f(\delta^*)$	C^* (μm)	P^* (N)
2.2	glass	P	.37	.084	.98	.38
		R	.32	.073	1.1	.65
2.5	Ge(s.c)	P	.41	.081	.16	.014
		R	.39	.078	.16	.016
2.5	B ₄ C	P	.41	.081	2.2	8.8
		R	.39	.078	2.2	10
2.5	Al ₂ O ₃ (s.c.)	P	.41	.081	.57	.44
		R	.39	.078	.58	.51
2.6	PSZ	P	.47	.088	22.0	238
		R	.45	.087	22.0	253
2.65	Si(s.c)	P	.48	.081	.36	.051
		R	.46	.088	.36	.055
2.8	SiC	P	.50	.090	2.6	5.2
		R	.47	.090	2.5	5.5
2.8	Si ₃ N ₄	P	.50	.090	7.3	30
		R	.47	.090	7.2	32
3.0	MgO	P	.55	.094	1.1	.34
		R	.55	.096	1.0	.31
3.0	MgF ₂	P	.55	.094	1.5	.43
		R	.55	.096	1.4	.39
3.3	Al ₂ O ₃	P	.62	.099	7.4	17
		R	.61	.10	7.0	15
4.0	ZnS	P	.79	.11	18	10
		R	.81	.11	17	8.5
6.3	NaCl	P	1.51	.14	350	130
		R	1.54	.14	340	116

[†] P: Peak load (upper bound)

R: Residual

Table IV. Median Crack Initiation Threshold Prediction

β	MATERIAL	LOADING [†] CONDITION	δ^*	$f(\delta^*)$	C^* (μm)	P^* (N)
2.2	glass	P	.39	.074	1.3	.6
		R	.31	.052	2.1	2.6
2.5	Ge	P	.43	.071	.22	.02
		R	.39	.058	.30	.05
2.65	Si	P	.46	.072	.54	.12
		R	.39	.058	.71	.29
2.8	SiC	P	.48	.071	4.1	14
		R	.41	.058	5.2	30
2.8	Si ₃ N ₄	P	.48	.071	11	79
		R	.41	.058	15	170
3.0	MgF ₂	P	.52	.071	2.5	1.3
		R	.50	.063	3.0	2.1
3.3	Al ₂ O ₃	P	.58	.071	13	62
		R	.51	.061	16	115
4.0	ZnS	P	.70	.072	38	54
		R	.65	.066	42	76
6.3	NaCl	P	1.24	.076	930	1320
		R	1.15	.073	940	1590
2.5	Al ₂ O ₃ (s.c.)	P	.43	.071	.77	.73
		R	.39	.058	1.0	1.6
2.5	B ₄ C	P	.43	.071	2.9	15
		R	.39	.058	4.0	33
2.6	PSZ	P	.46	.072	33	580
		R	.39	.058	43	1360
3.0	MgO	P	.52	.071	1.7	1.0
		R	.50	.063	2.1	1.6

[†] P : Peak Load (lower bound) R : Residual.

Table V. Lateral Crack Initiation Threshold Prediction

β	ζ	Material	Loading	δ^*	$f(\delta^*)$	c^* (μm)	P^* (N)
2.2	0.6	glass	P	.31	.033	5.4	16
			R	.41	.047	3.4	3.7
	1.0		P	.23	.024	7.4	55
			R	.41	.055	2.5	2.0
	2.2		—	—	—	—	— [‡]
			R	.51	.011	71	1040
2.8	1.0	SiC	P	.38	.036	12	205
			R	.51	.054	7.4	41
2.8	1.0	Si ₃ N ₄	P	.38	.036	35	120
			R	.51	.054	21	240
4.0	2.0	ZnS	P	.66	.044	96	400
			R	.84	.060	65	110

[‡] No crack will initiate at Mode I fracture.

Table VI. Radial Fracture Predictions for Polycrystalline Materials

Material	β	K_{IC} MPa $m^{1/2}$	H GPa	E GPa	c^* (μm)	p^* (N)
B ₄ C	2.5	6.0	32.2	500	2	9
PSZ	2.6	6.9	11.4	170	20	240
SiC	2.8	4.0	19.3	420	3	5
Si ₃ N ₄	2.8	4.9	14.1	320	7	30
MgF ₂	3.0	.9	5.8	140	1.4	0.4
MgO	3.0	1.2	9.2	240	1	0.3
Al ₂ O ₃	3.3	4.1	12.0	393	7	15
ZnSe	4.4	.9	1.0	68	50	3.4

Table VII. Radial Crack Initiation Threshold

Material	β	Prediction		Experimental Observations	
		c^* (μm)	p^* (N)	c^* (μm)	p^* (N)
Glass	2.2	1.1	$.6^{\ddagger}$	17	5^{Δ}
Ge(s.c)	2.5	.16	$.014^{**}$.25	$.02^{\ddagger}$
Si(s.c)	2.65	.36	$.05^{**}$.65	$.03^{\ddagger}$
Al_2O_3 (s.c)	2.5	.6	$.4^{**}$	3	$.25-.50^{\square\ddagger}$
NaCl(s.c.)	6.3	340	120	100	$15-60^{\ddagger}$
ZnS	4.0	17	8^{**}	70	$6^{\ddagger\ddagger}$

- Δ Marshall and Lawn (7)
 \ddagger Lankford and Davidson (33)
 $\ddagger\ddagger$ Evans and Wilshaw (9)
 \square Data obtained for a single grain (grain size $25\mu\text{m}$)
 \ddagger Crack initiates when fully unloaded.
 $**$ Crack initiates during loading.

Table VIII. Relative Threshold Characteristics for Radial, Median and Lateral Cracks

Material	β	Crack [†] Type	$c^*(\mu\text{m})$	$p^*(\text{N})$
Glass	2.2	R	1	0.4
		M	1	0.6
		L	3	2.0
SiC (Polycrystal)	2.8	R	3	5.0
		M	4	14
		L	7	40
Si ₃ N ₄ (Polycrystal)	2.8	R	7	30
		M	12	80
		L	20	210
ZnS (Polycrystal)	4.0	R	20	8
		M	40	50
		L	65	100

[†] R : Radial M : Median L : Lateral

FIGURE CAPTIONS

- Figure 1. Micrographs (on the left) and schematics (on the right) of indentation showing different deformation response. a) rigid/plastic indentation; b) elastic/plastic indentation.
- Figure 2. The effect of the ratio of the modulus to the hardness, E/H , on the relative plastic zone size β (b/a) for a range of materials. Also shown are the theoretical predictions from the Hill solution, the Johnson analysis and the present analysis.
- Figure 3. The trend in the ratio of the indentation pressure to the yield strength with the modulus to yield strength ratio for a range of materials. Also shown are the predictions from the Hill solution, the Johnson analysis and the present analysis.
- Figure 4. The geometry of two indentations with equivalent indentation volume: a) hemispherical indentation; b) pyramidal indentation.
- Figure 5. A schematic showing the analytic procedure for creating a stress free surface and hence, for deforming the residual stress distribution: a) the general procedure; b) the specific procedure for the hemispherical indentation; and c) the upper and lower bound conditions used for calculating the stress at peak load.

Figure 6. The ratio of the hardness H to the spherical cavity pressure p around the hemispherical indentation interface for three values of the relative plastic zone size, β , indicating the relative uniformity of H/p .

Figure 7. The ratio of the modified yield strength Y' to the spherical cavity pressure p around the hemispherical indentation interface for three values of the relative plastic zone size, β .

Figure 8. Free surface correction factors m and m_r plotted as a function of the relative plastic zone size.

Figure 9. A schematic showing crack patterns generated by Vickers indentation in a homogeneous material. a) Four radial cracks propagating along the indentation diagonal direction. b) Sectional view of the indentation; the dotted region represents the plastic zone created by indentation. The median crack coalesces with the radial crack to form a half-penny shaped crack. Lateral cracks propagate parallel to the surface.

Figure 10. The components of the peak load tangential stress at the surface ($z=0$) pertinent to radial fracture, indicating the initial cavity solution, the modification induced by the free surface and the point force solution used to compute the upper bound peak load stress.

Figure 11. The tangential stress at the surface pertinent to radial fracture, obtained at both the peak load condition and in the residual condition, for two choices of the relative plastic zone size.

Figure 13. The gradient in the near surface residual tangential stress, taken from the elastic/plastic boundary, surface intersection, for two choices of the relative plastic zone size.

Figure 14. The components of the peak load tangential stress along the median axis ($x=0$) pertinent to median fracture, indicating the initial cavity solution, the modification induced by the free surface and the point force solution used to compute the lower bound peak load stress.

Figure 15. The tangential stress distribution pertinent to median cracks in the peak load (upper bound) and residual conditions.

Figure 16. The gradient in the tensile stress component that dictates median fracture.

Figure 17. The σ_{zz} stress that determines lateral fracture at different depth locations for a relative plastic zone size of 2.2 (a) at peak load and (b) the residual stress.

Figure 18. The trends in the σ_{zz} stress with relative plastic zone size.

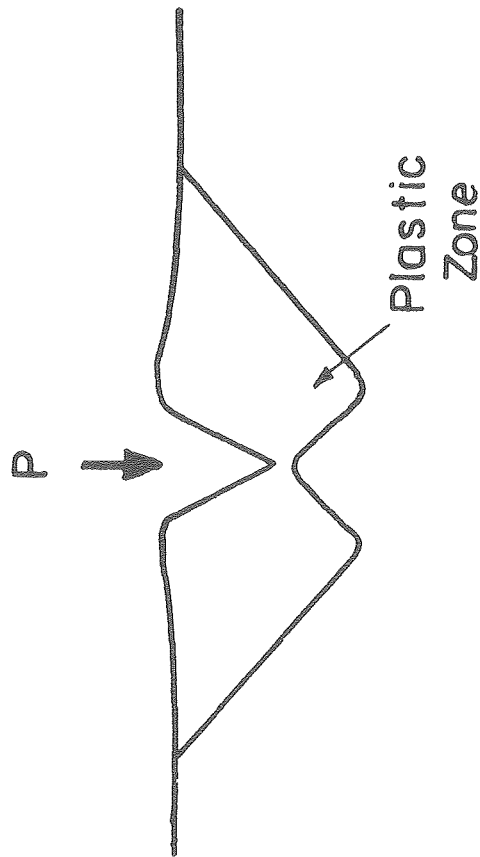
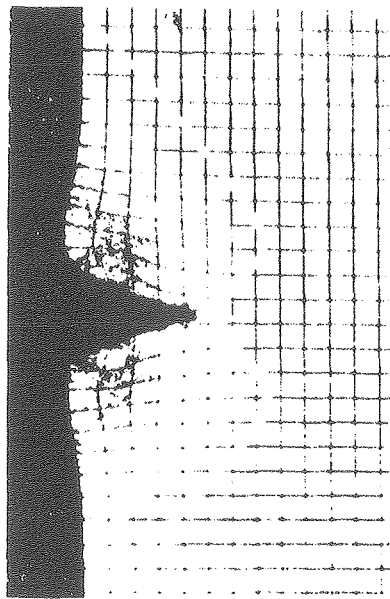
Figure 19. A correlation of the predicted radial crack length with experimental data for well developed cracks.

Figure 20. The variation of the predicted minimum threshold loads for radial and median cracking with the relative plastic zone size.

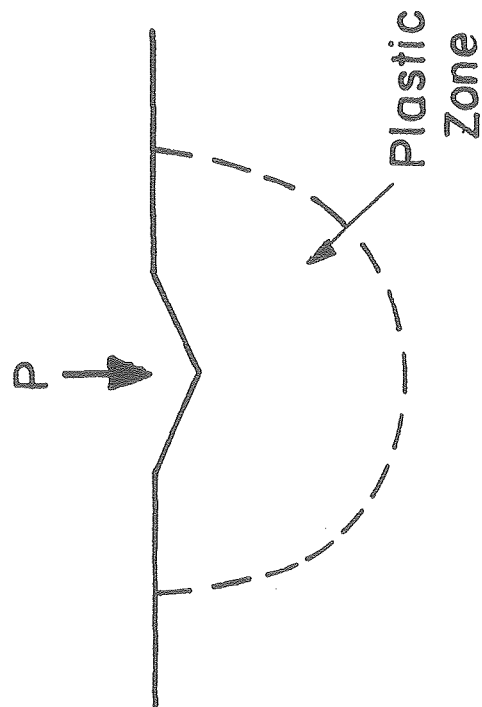
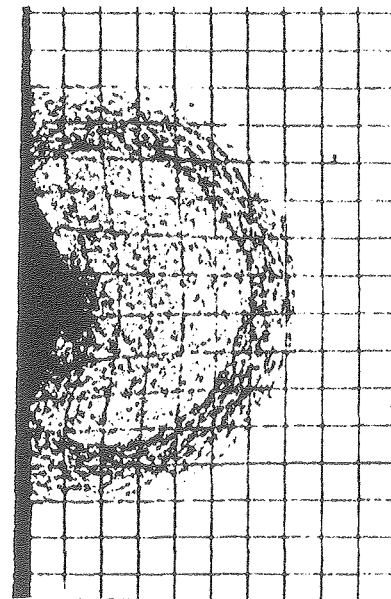
Figure 21. The variation in the normalized stress intensity factor for radial cracks with the relative crack length.

Figure 22. The geometry of three different indenters; a) pyramid,
b) cone, c) sphere.

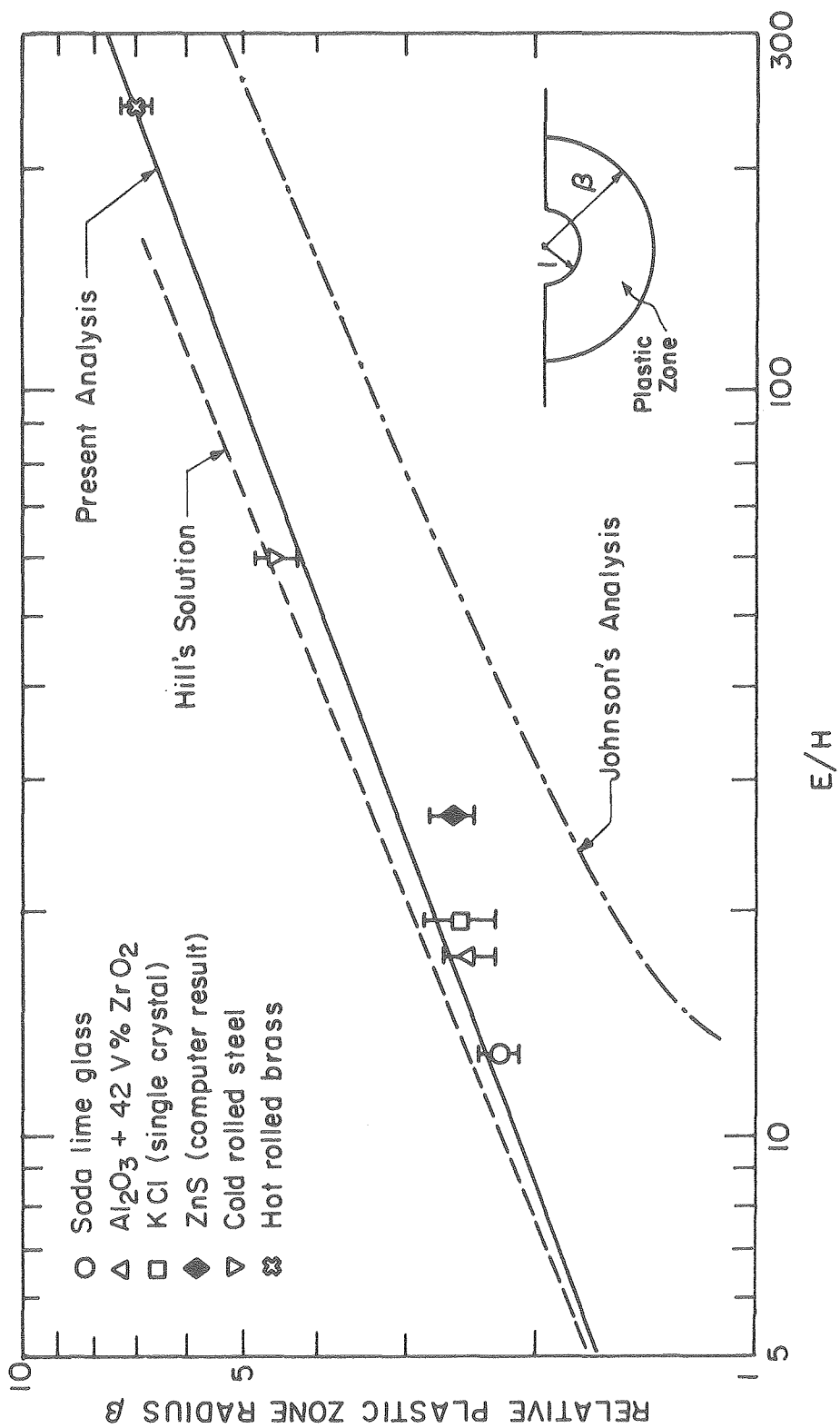
Figure 23. The coordinate system used for stress analysis.



(a) Rigid / Plastic Indentation

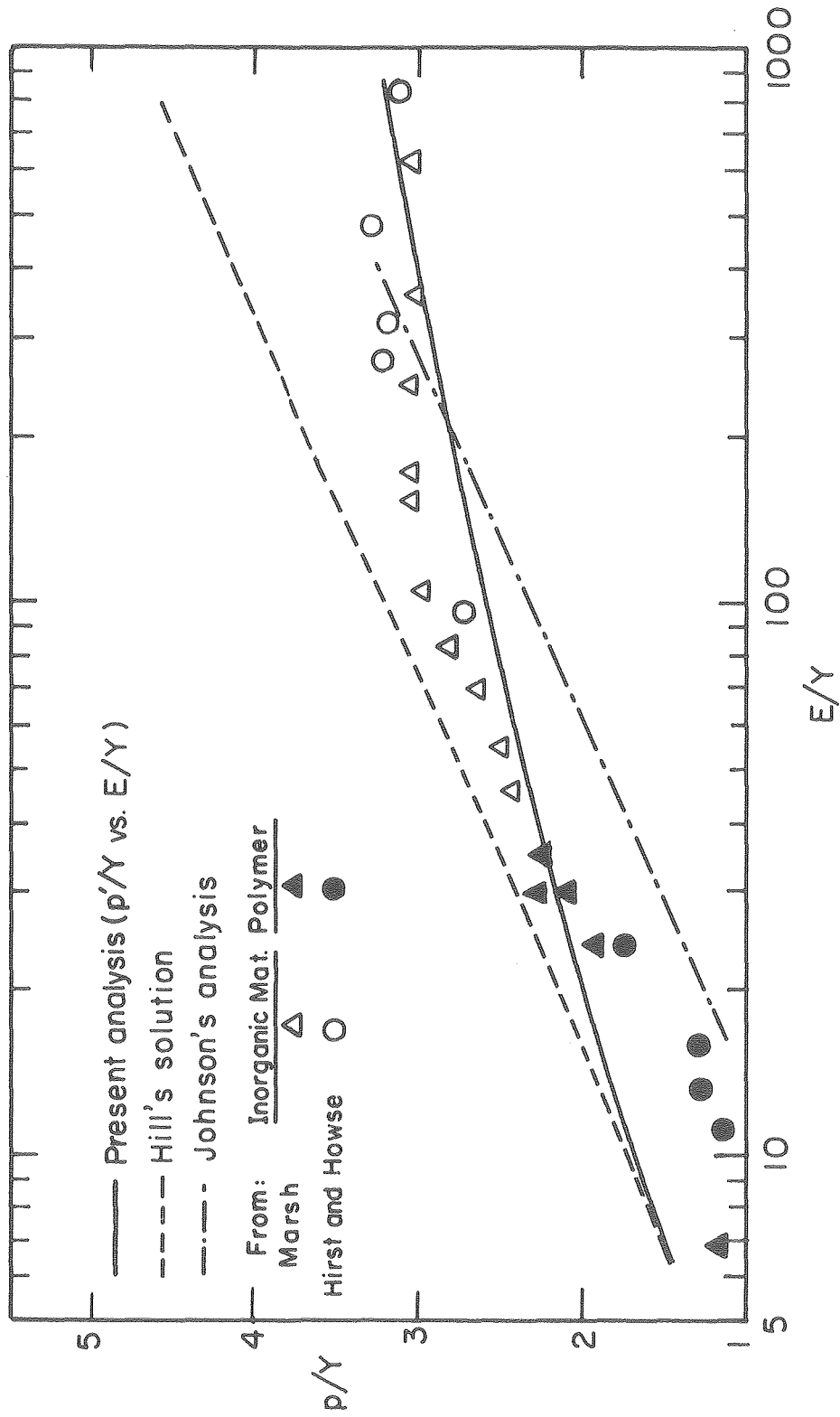


(b) Elastic / Plastic Indentation



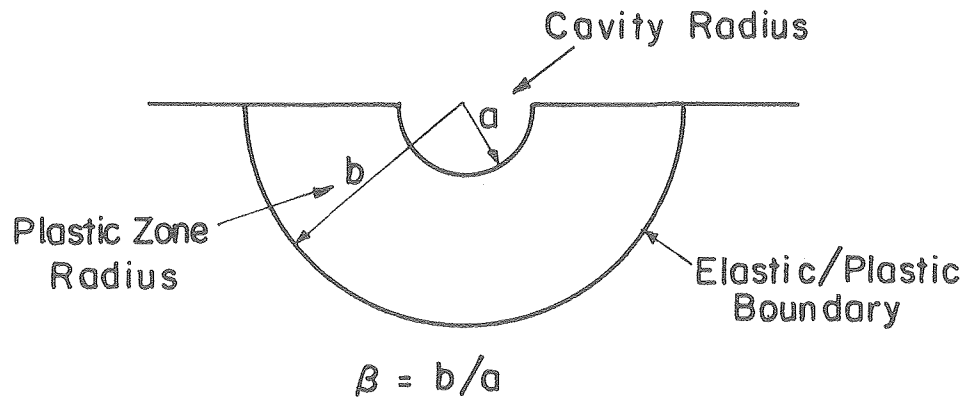
XBL 806-5362 A

Fig. I-2

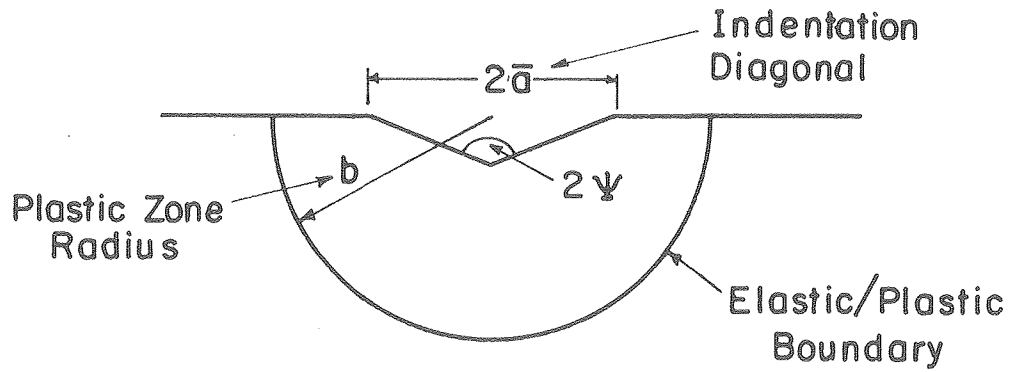


XBL 806-5363

Fig. I-3



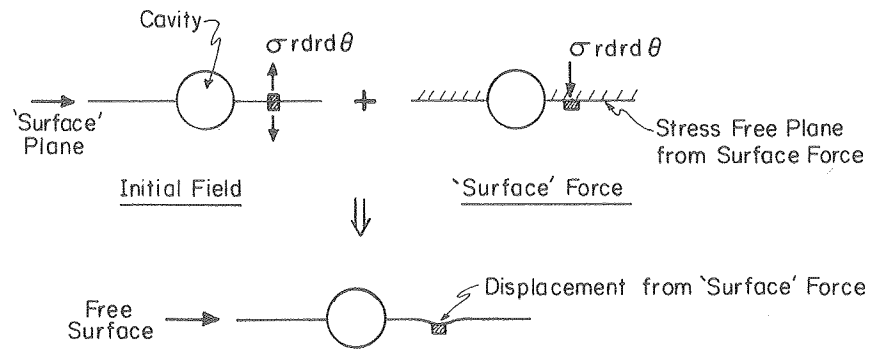
(a) Hemispherical Indentation



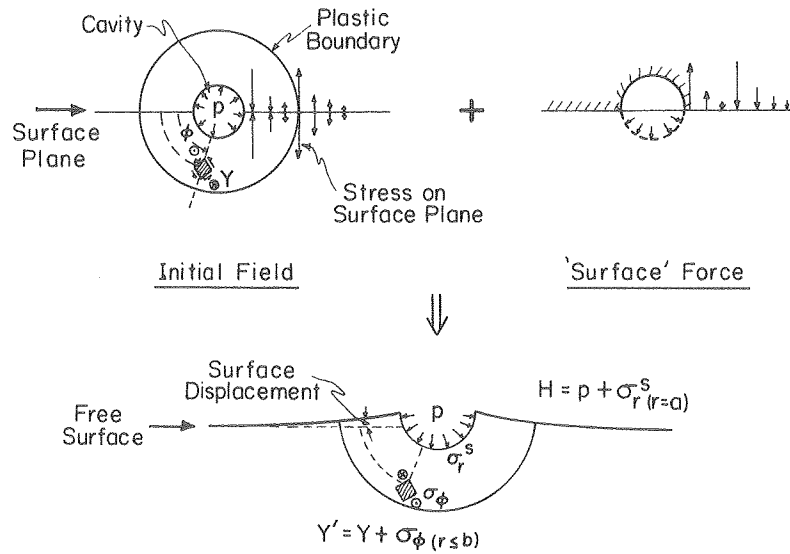
(b) Pyramidal Indentation

XBL 8011-6344

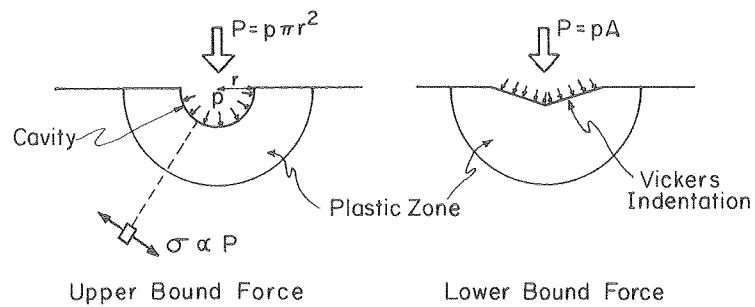
Fig. I-4



a) Elemental Procedure for Creating a Stress Free (Surface) Plane

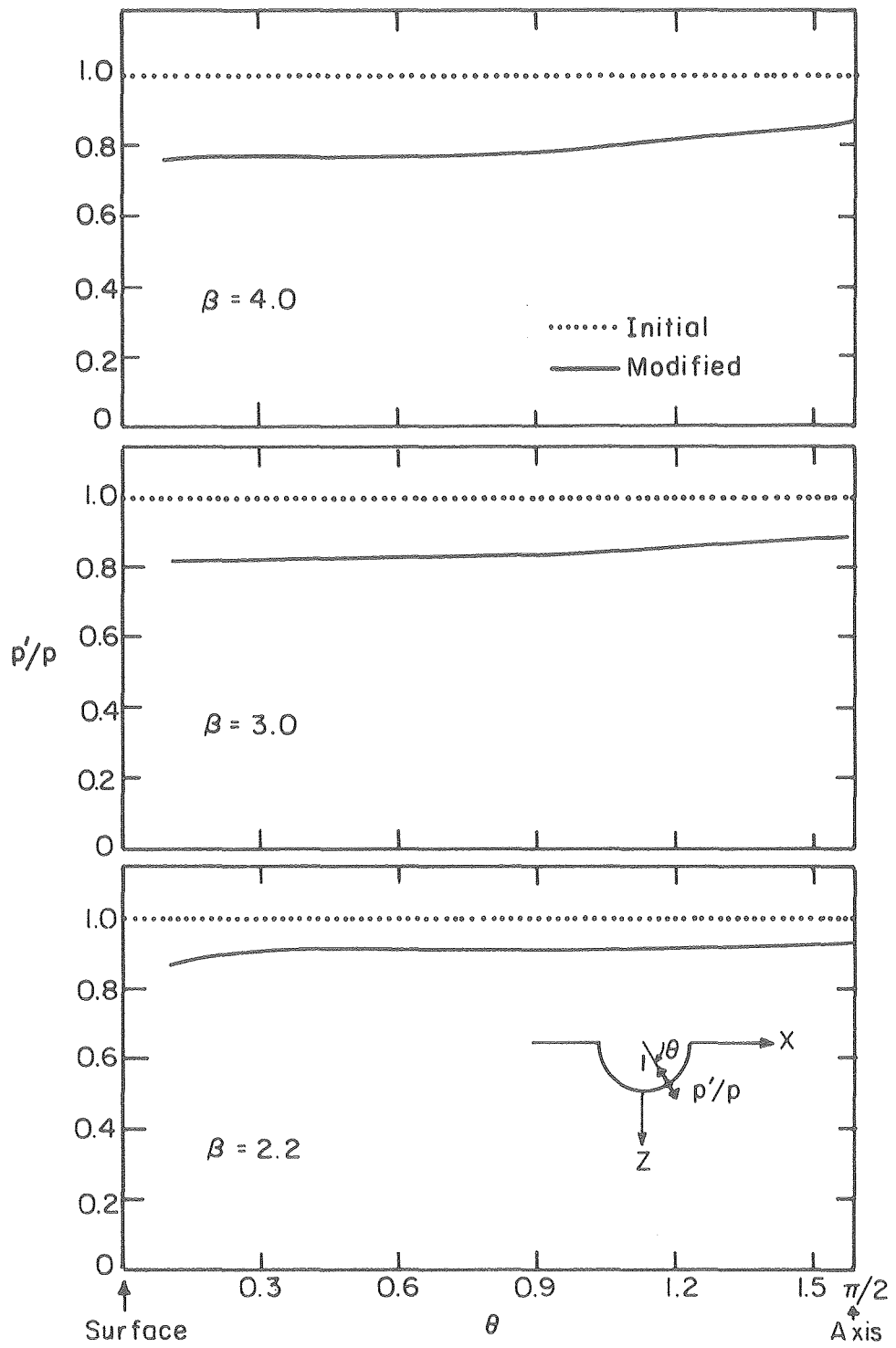


b) Specific Procedure



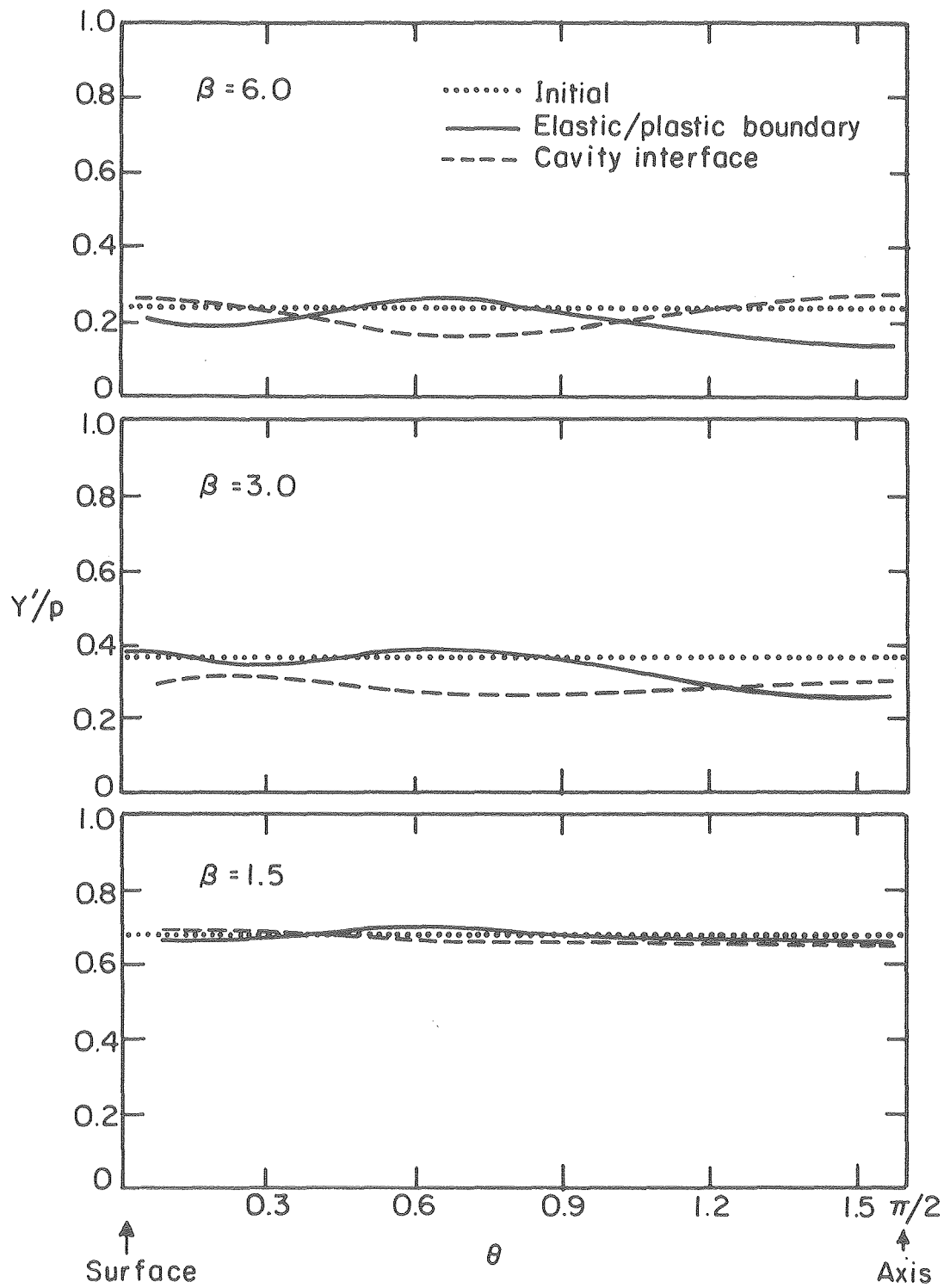
XBL 806-5376

Fig. I-5



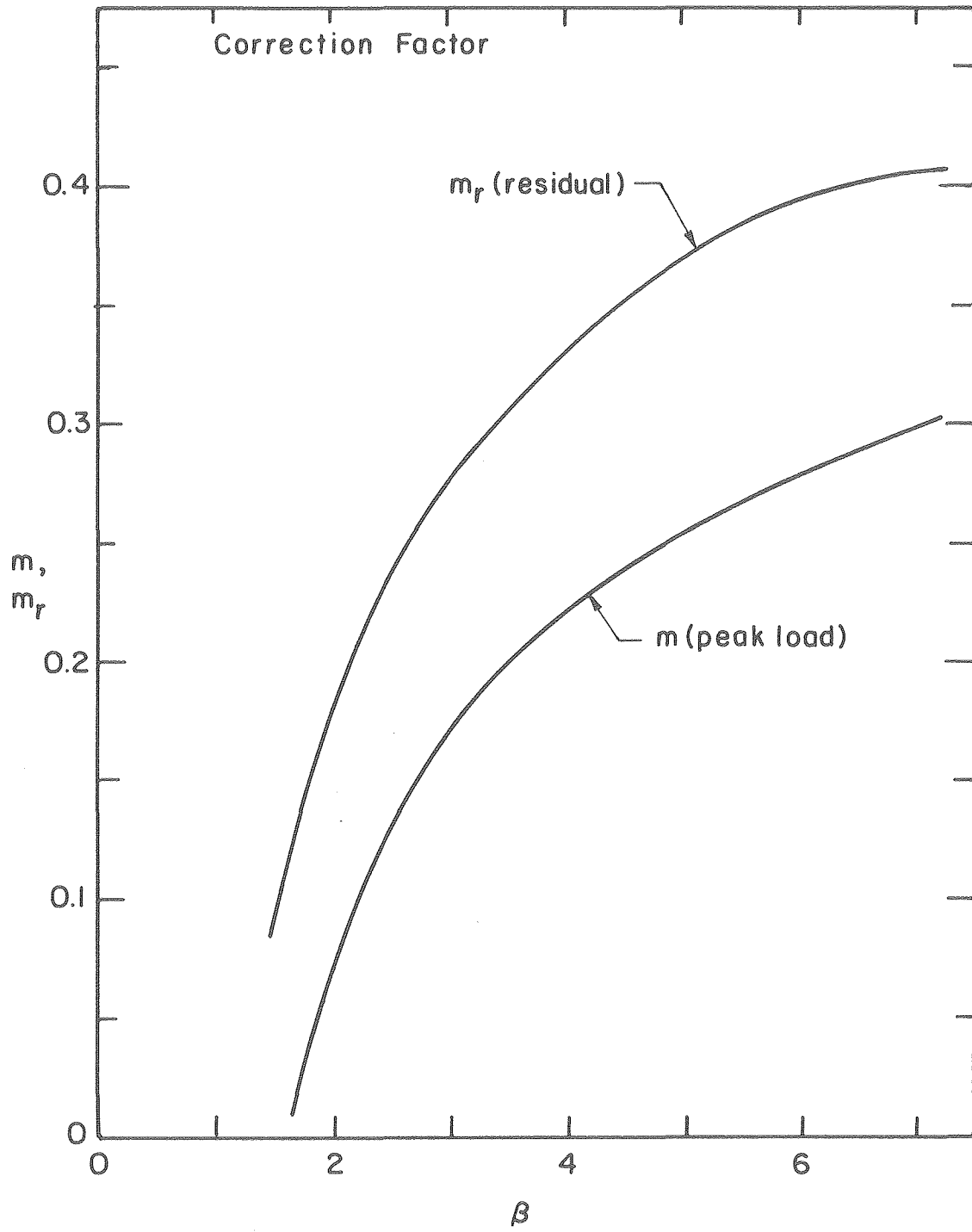
XBL 806-5365

Fig. I-6



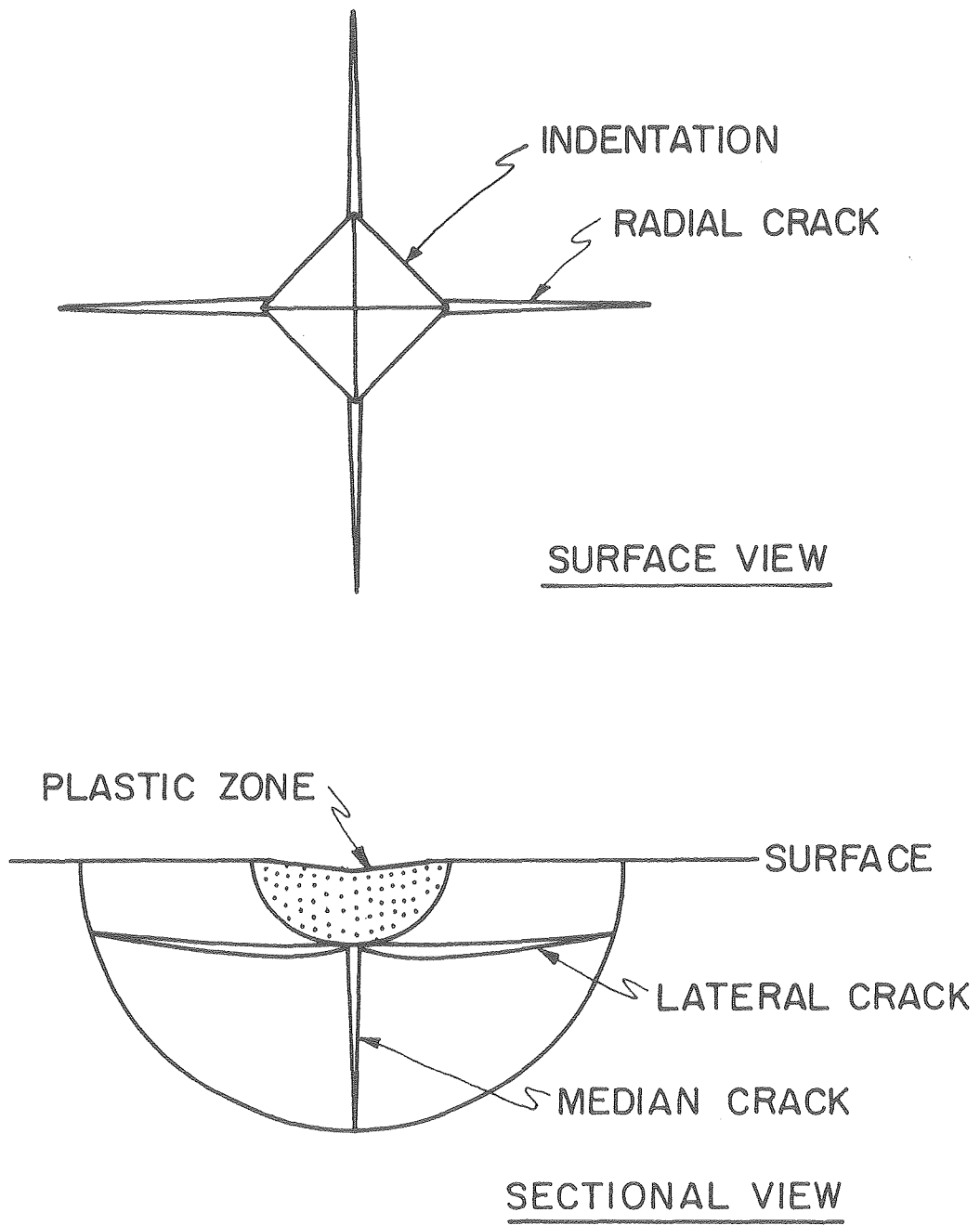
XBL806-5366

Fig. I-7



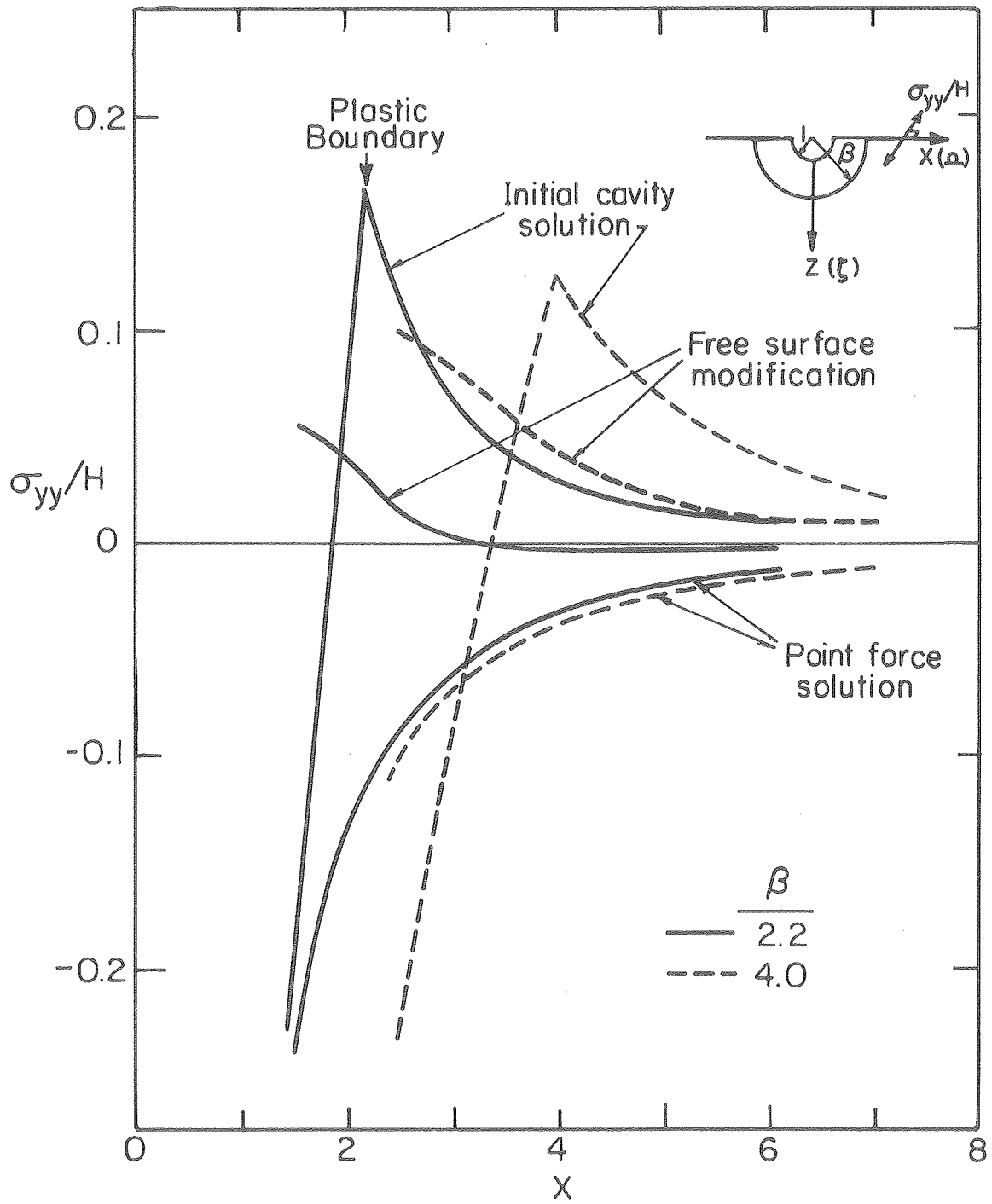
XBL 806-5364

Fig. I-8



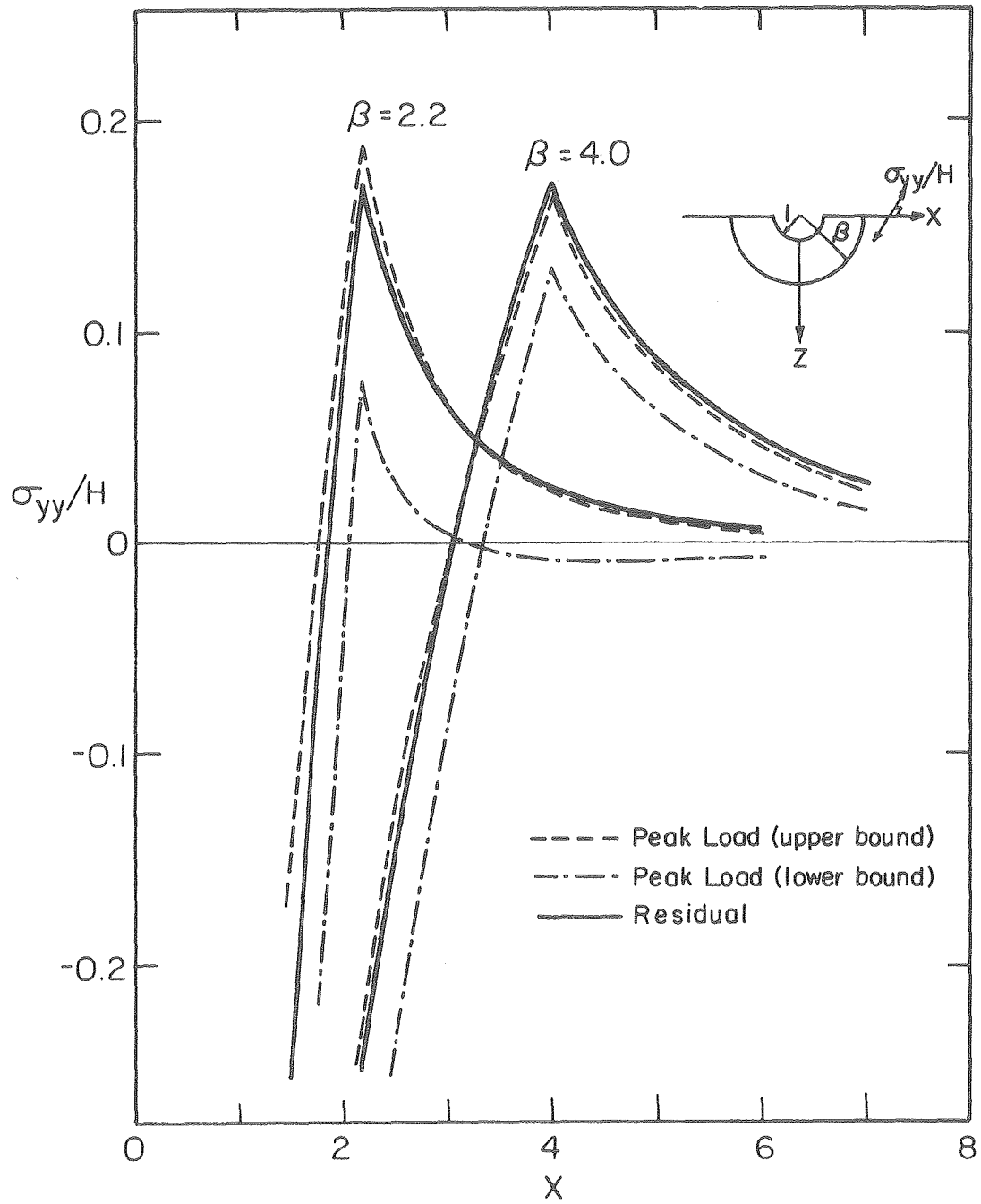
XBL 8010-6085

Fig. I-9



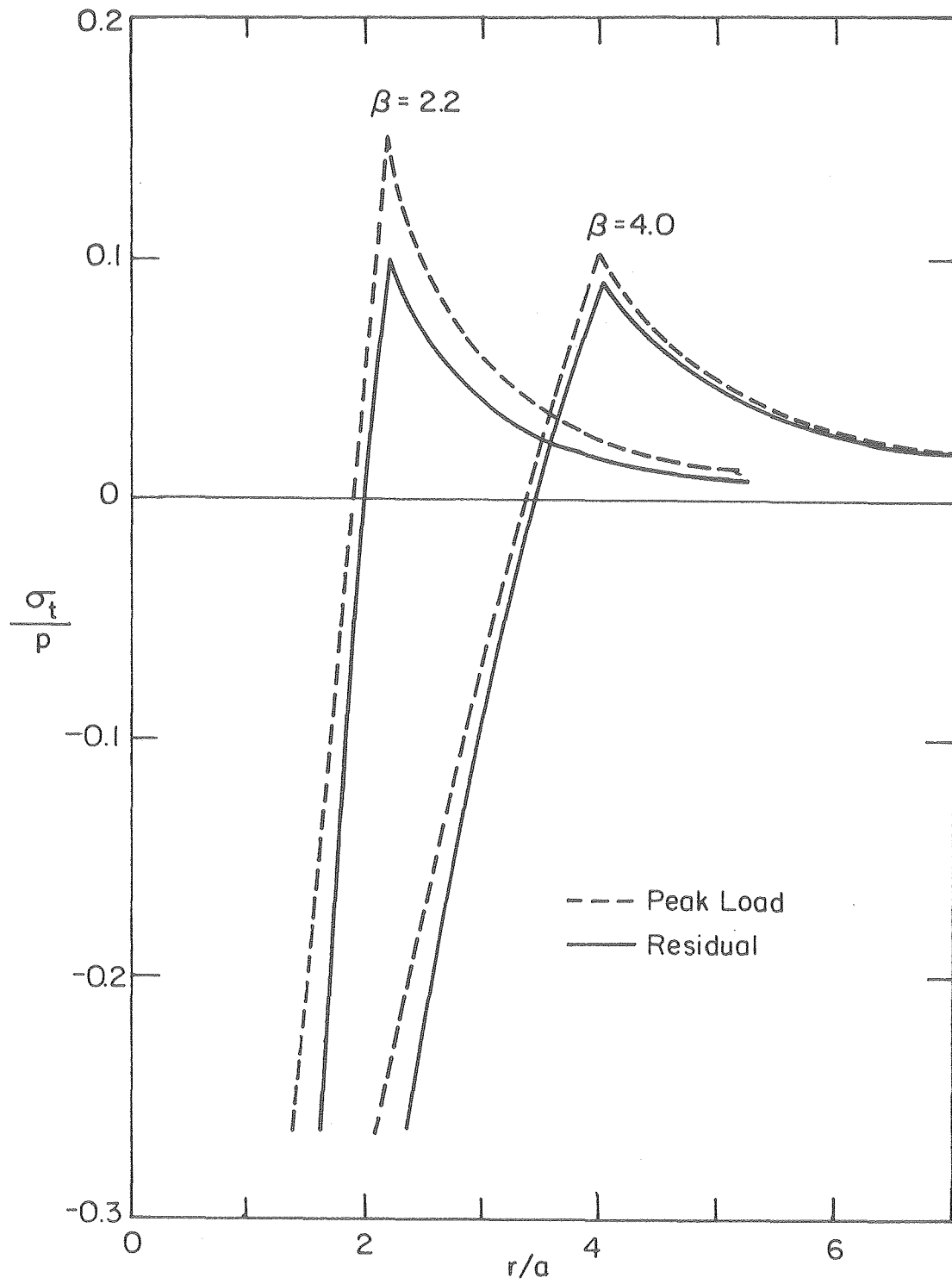
XBL 806-5372 A

Fig. I-10



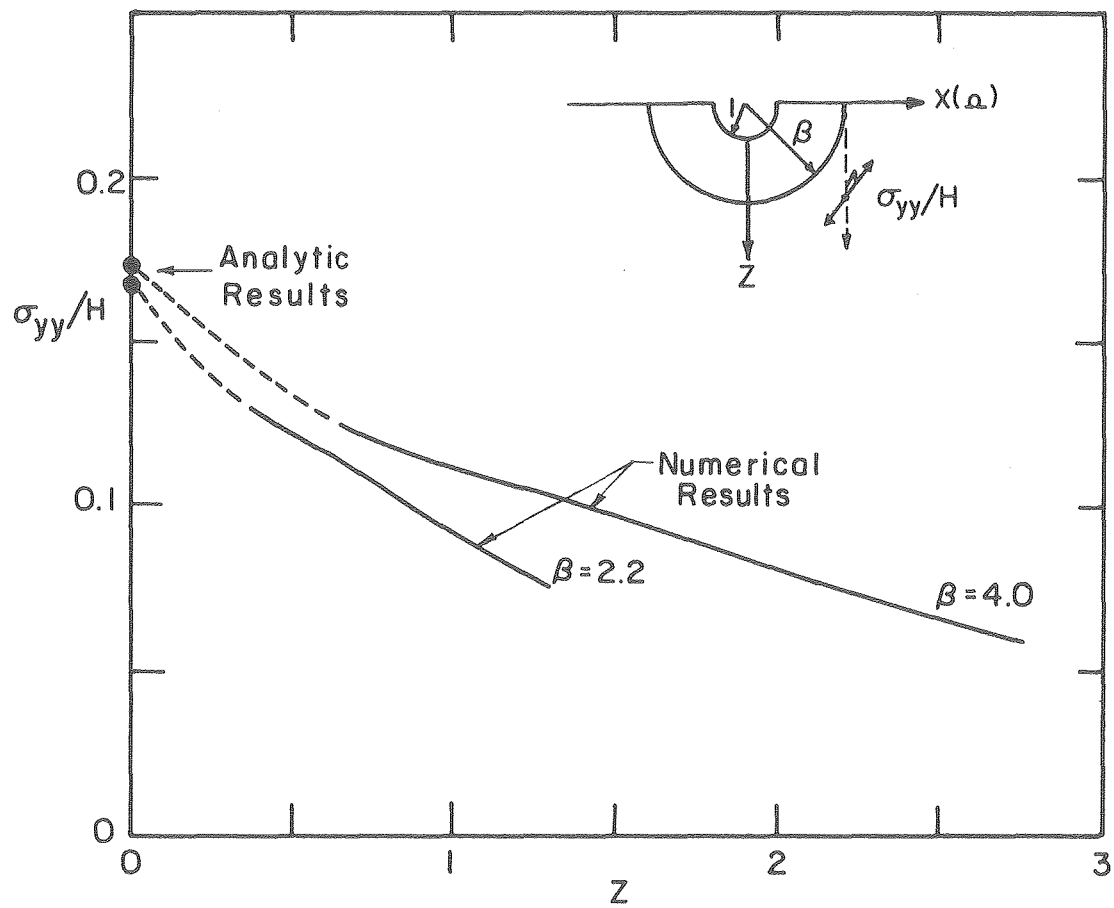
XBL 806-5371A

Fig. I-11



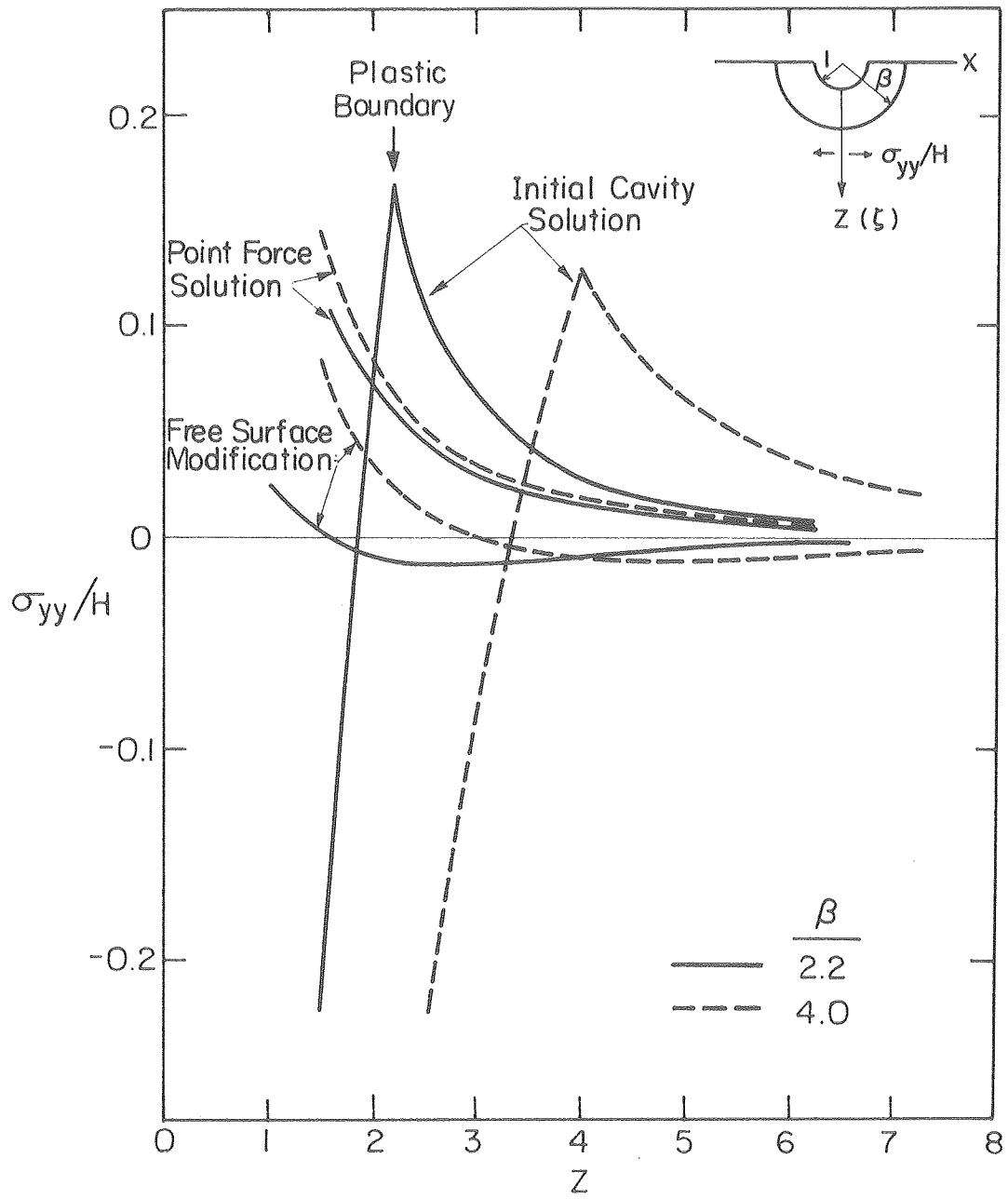
XBL8011-6342

Fig. I-12



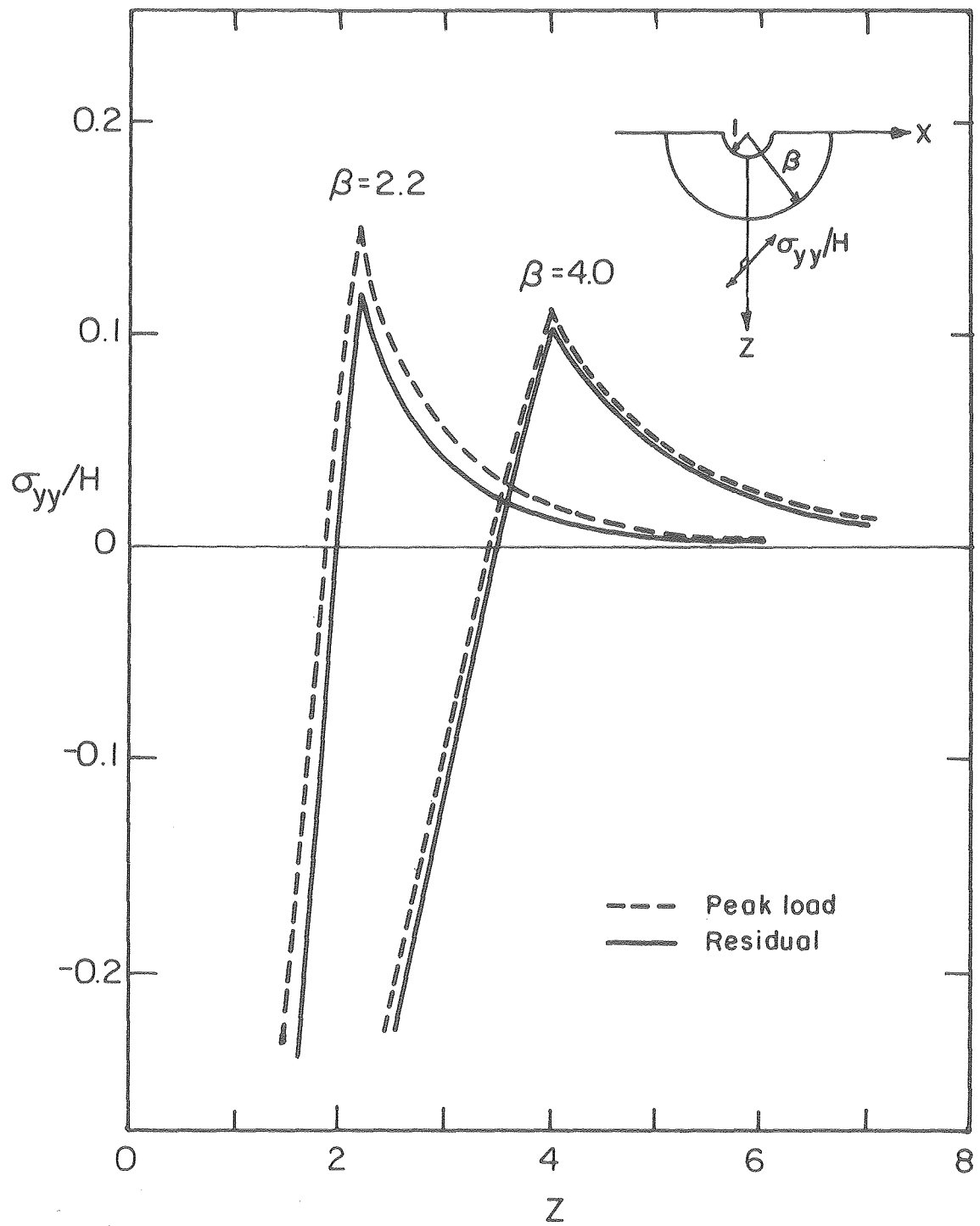
XBL 806-5367 A

Fig. I-13



XBL 8012-13435

Fig. I-14



XBL 806-5374 A

Fig. I-15

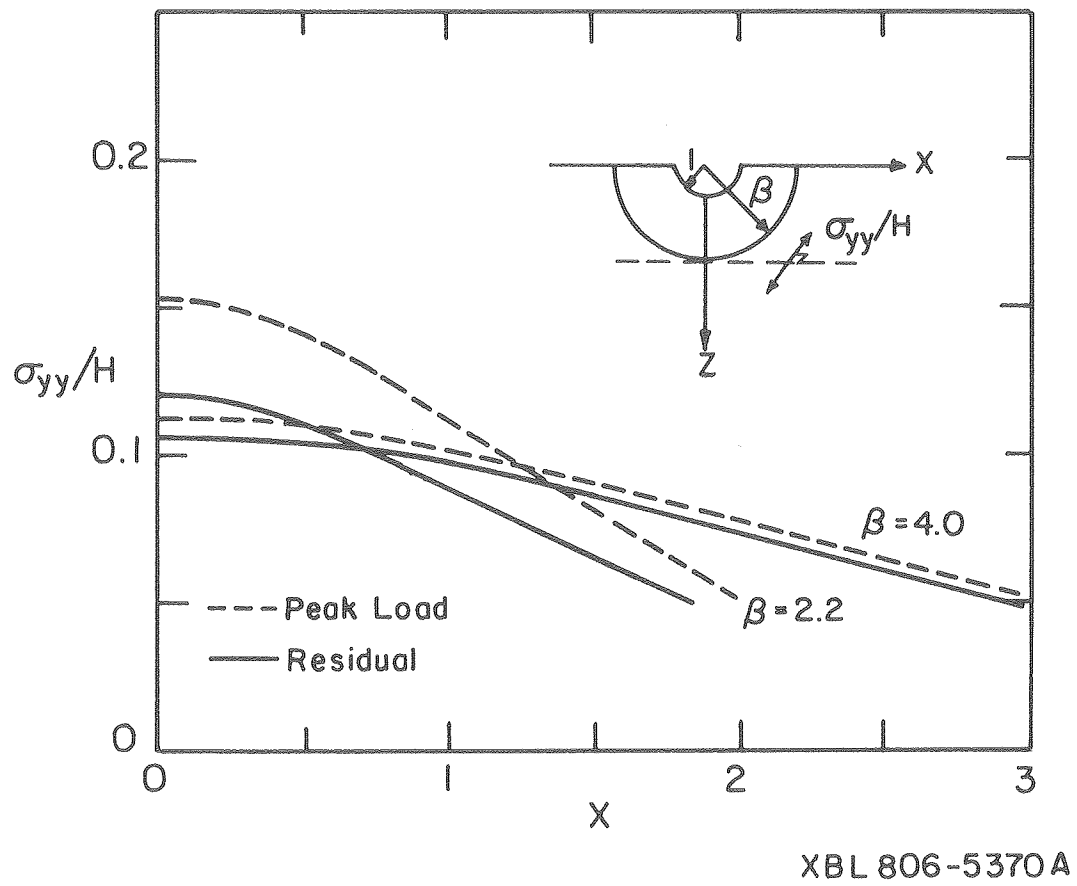
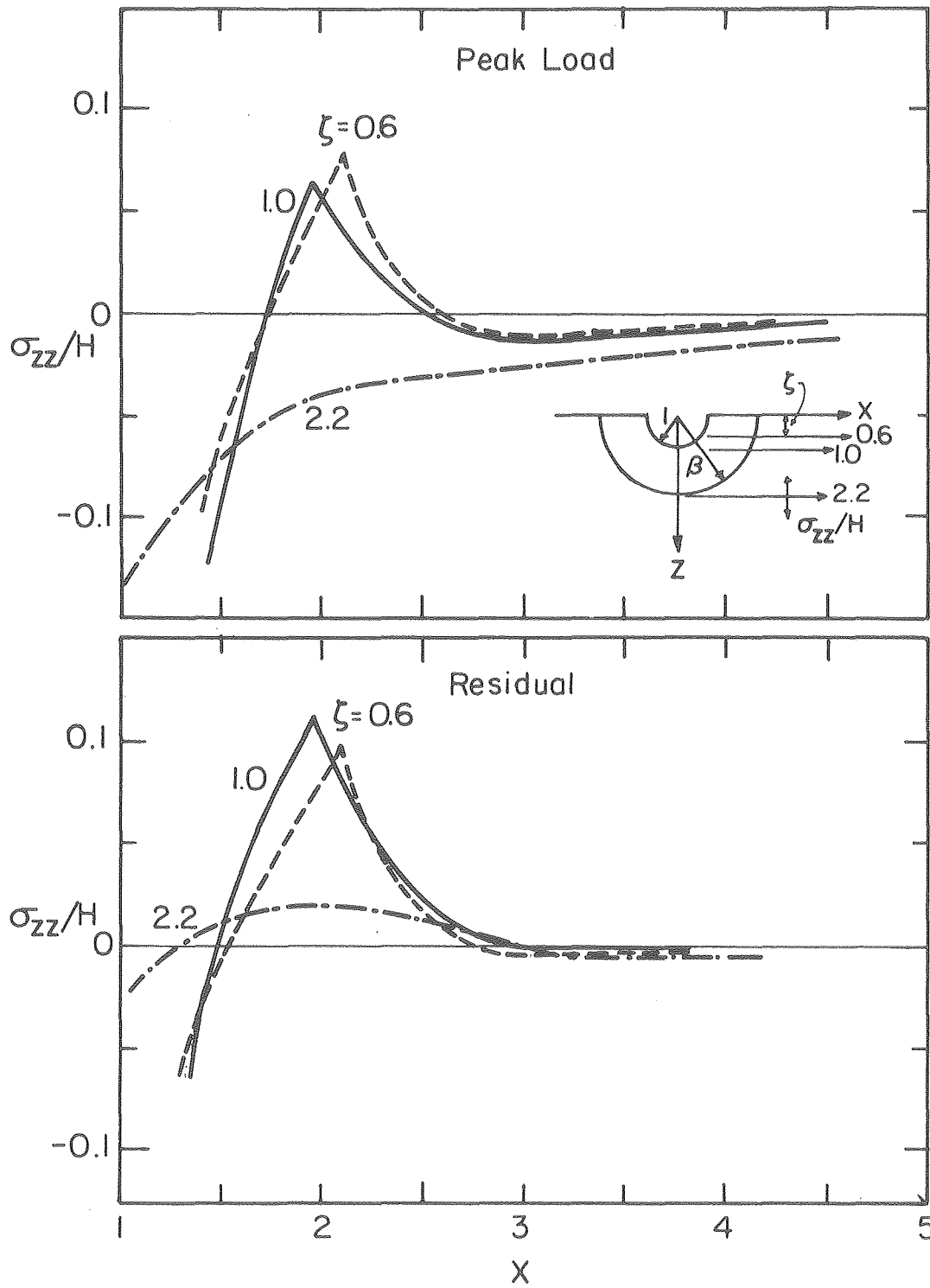
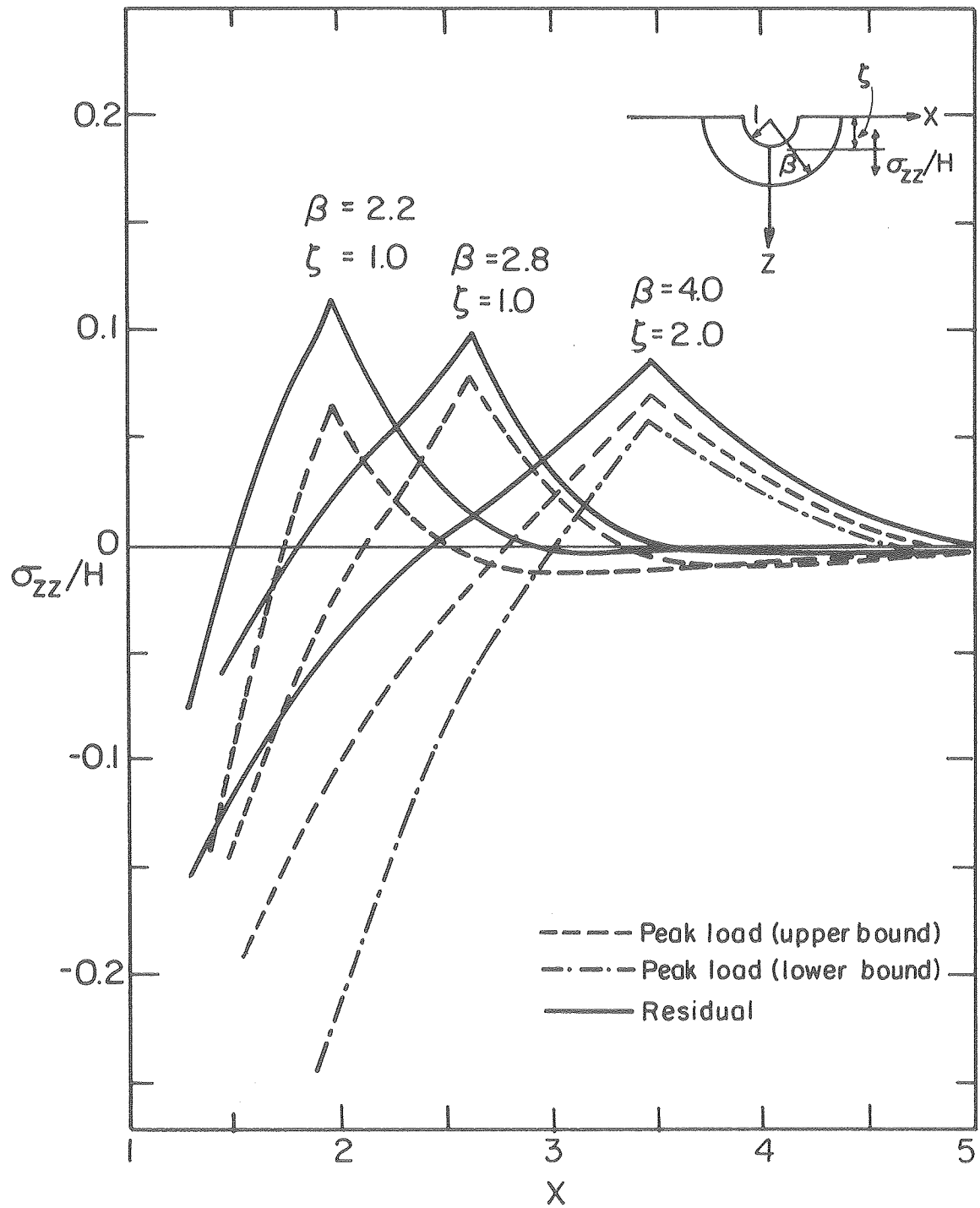


Fig. I-16



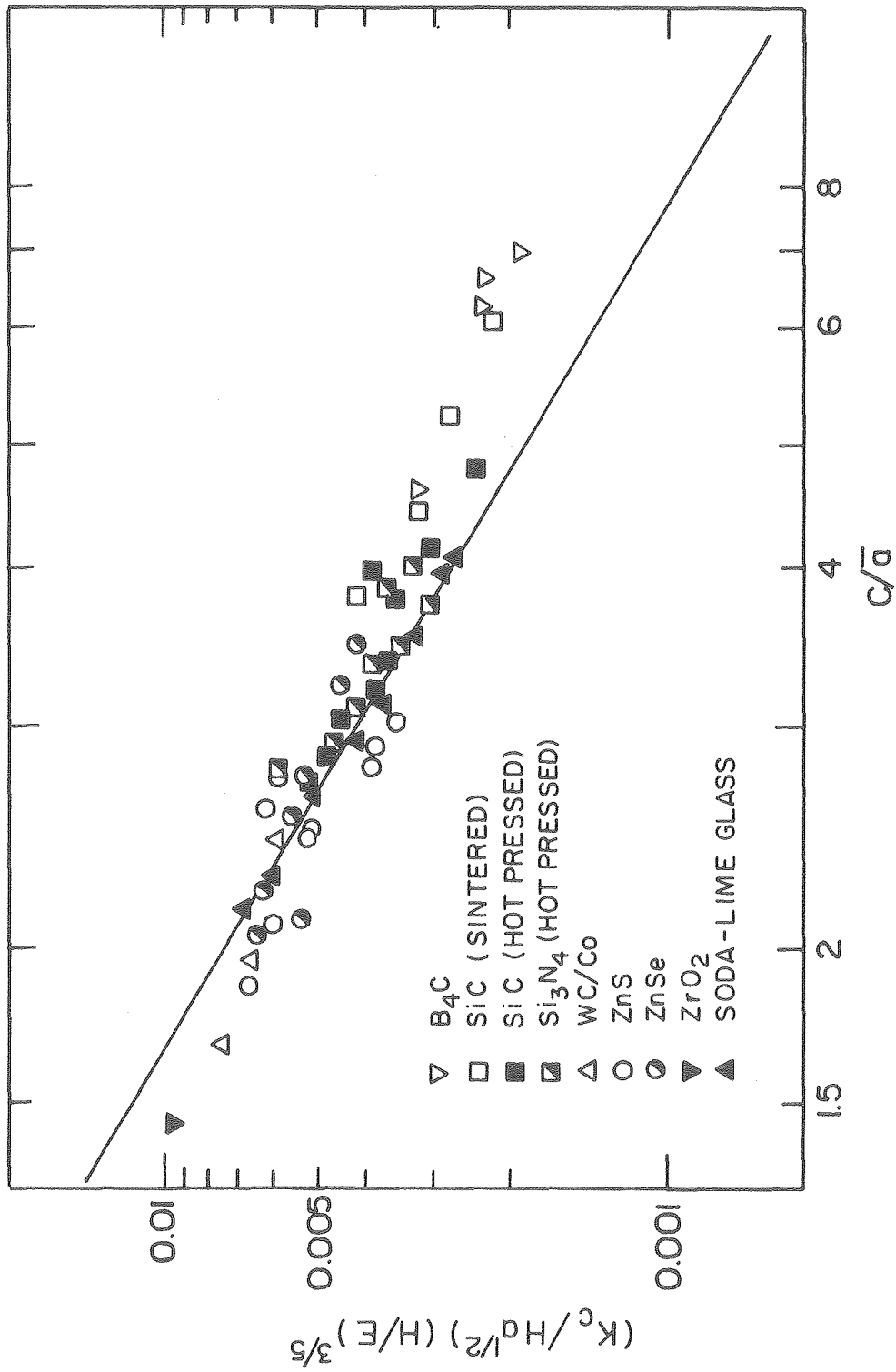
XBL 806-5373 A

Fig. I-17



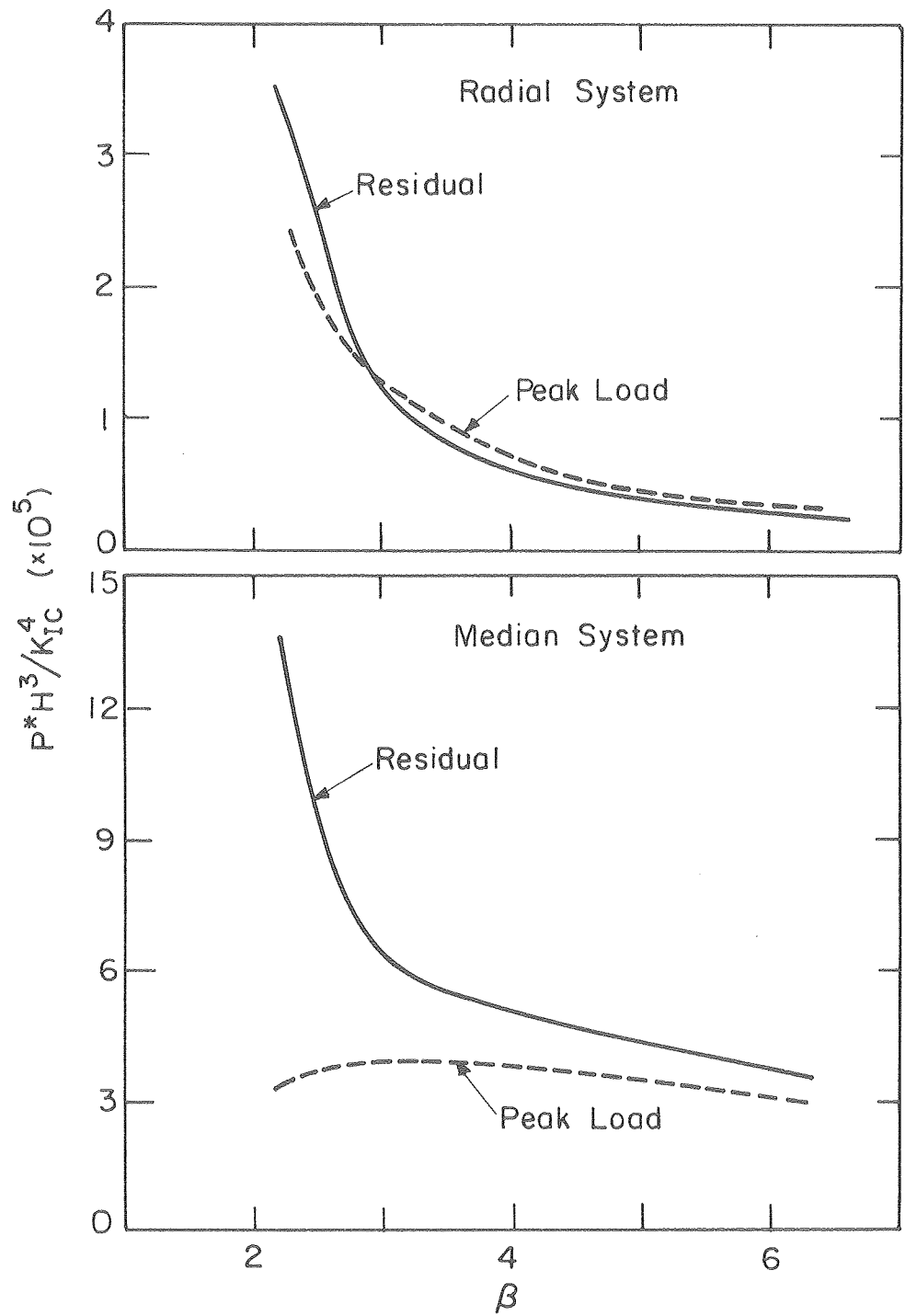
XBL 806-5375A

Fig. I-18



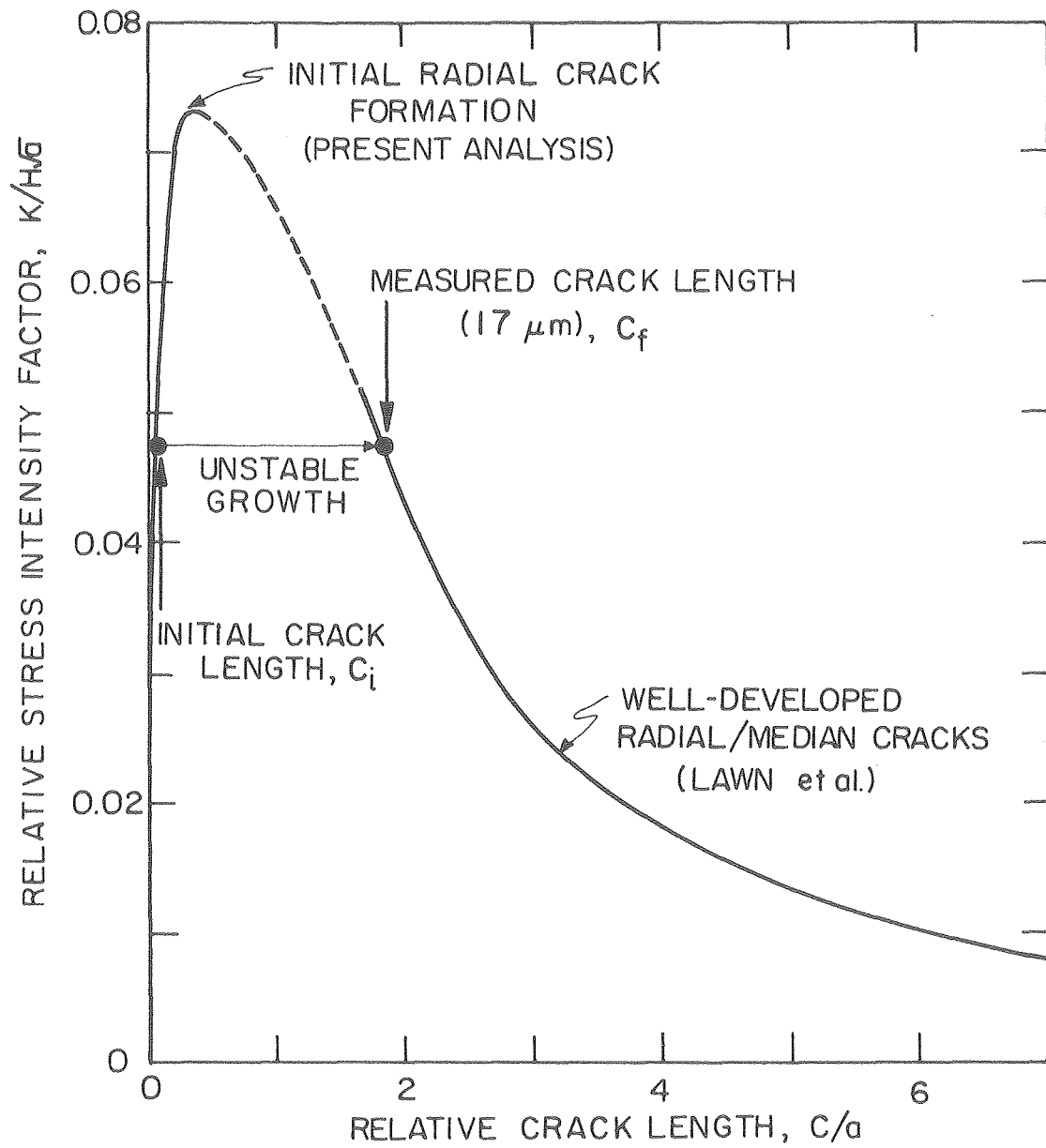
XBL 8010-6081

Fig. I-19



XBL8010-6057

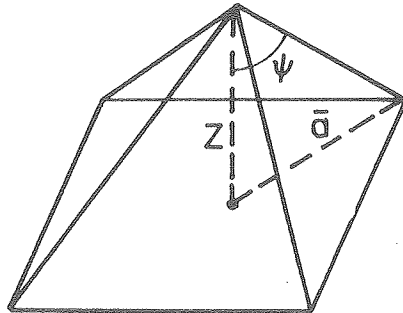
Fig. I-20



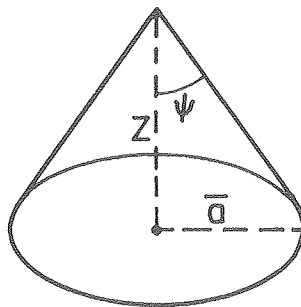
XBL 8010-6080

Fig. I-21

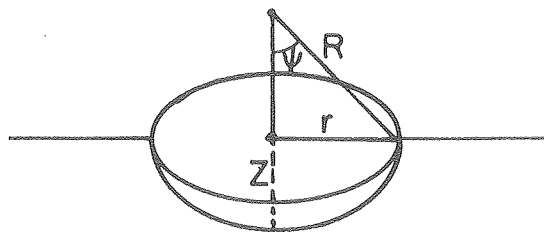
EQUIVALENT HEMISPHERICAL VOLUME



(a) Pyramidal Indenter



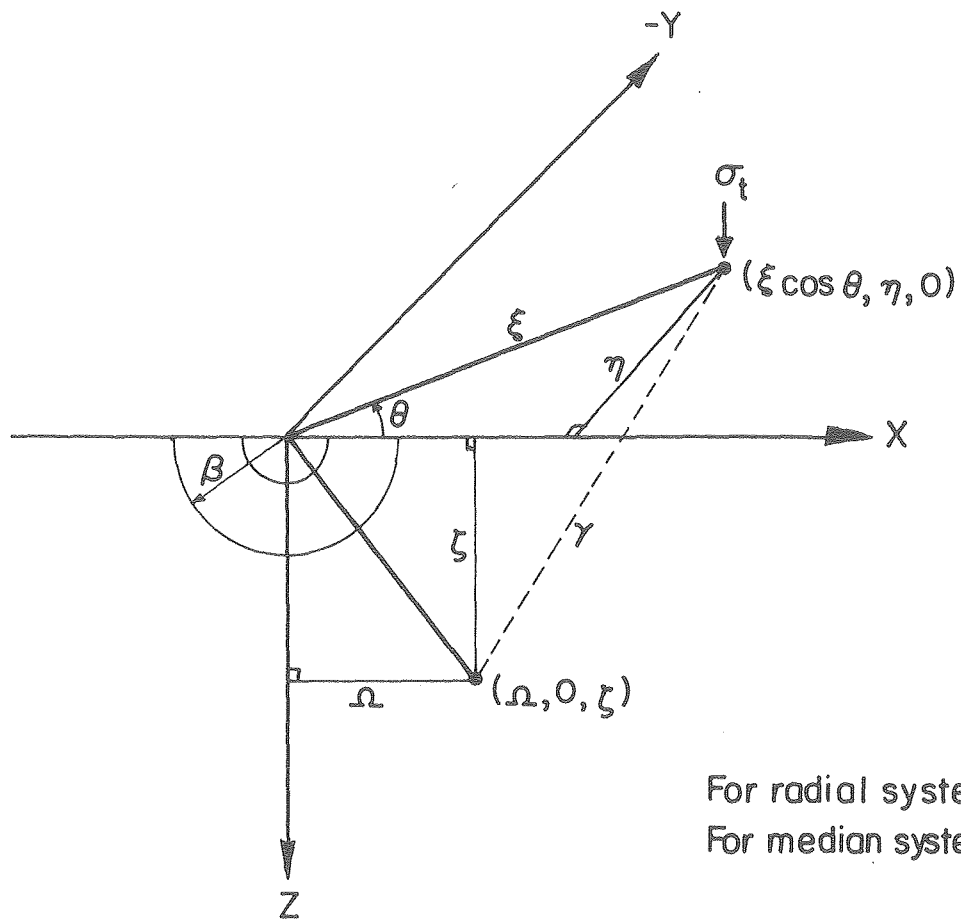
(b) Conical Indenter



(c) Spherical Indenter

XBL8011-6343

Fig. I-22



XBL8010-6056

Fig. I-23

PART II

THE APPLICATION OF INDENTATION TO ADHESION MEASUREMENTS

1. INTRODUCTION

1.1 General

The quantification of adhesion between films (or coatings) and substrates is an important but inadequately resolved problem. A meaningful method of measuring adhesion is needed both for quality control and for the development of improved film properties (e.g., monitoring variations of adhesion with different treatments and fabrication methods). This need has become increasingly important with the recent expansion in the use of thin film/substrates in the electronics industry.

Ideally, the requirements of an adhesion test are: quantitative interpretation, applicability to a wide range of film thickness and film/substrate combinations, economy (minimal material use and machining requirements), reliability, sensitivity, and adaptability to routine testing. Despite many attempts to develop techniques for adhesion measurements,¹⁻⁸ an entirely adequate quantitative test has not yet emerged. A brief survey and critique of the tests currently used will be given in Sec. 1.2. The objective of the present study is to develop an adhesion test, based on indentation fracture procedures, that satisfies these criteria.

Adhesion tests based on fracture mechanics principles are the most likely source of quantitative procedures.^{9,10} Fracture mechanics methods exhibit several attractions. Firstly, an adhesion parameter, such as the adhesion strength, the work of adhesion, or the interface fracture resistance (or toughness) K_C^{inter} , can be defined.

Secondly, fracture mechanics provides a mathematical framework for developing sound, theoretically based, measurements of interface toughness. In addition, scattered results obtained in adhesion measurement can be characterized and rationalized by adopting concepts based on fracture statistics. Finally, the fracture test provides results with the potential of being used as a design parameter. However, currently available tests¹⁰ are of restricted application and are too complex for most purposes (see Sec. 1.2.2).

The test method proposed in this study involves the introduction of a mechanically stable crack into the interface, by employing conventional indentation procedures. The resistance to propagation of the crack along the interface is then used as a measure of adhesion. Analysis of the results is based on recently developed indentation fracture mechanics.¹¹⁻¹³ The test is demonstrated to yield a sensitive measure of interface toughness. Also, by virtue of its inherent simplicity, and small scale, it appears to meet most of the requirements for a widely applicable adhesion measurement technique.

1.2 Review of Adhesion Measurement Techniques

Many techniques of measuring adhesion between film and substrate systems have been described in the literature. However, the parameter measured and its physical significance remain ambiguous. Chapman,³ with further elaboration by Mittal,⁴ pointed out that these methods generally conform to two approaches. The first is referred to as an academic approach. It measures "basic adhesion," which is the inter-atomic bonding force across or within the interface. This approach is based on the premise that an understanding of film adhesion at the

macroscopic level must be based on a knowledge of interface bonding.

Basic adhesion can be theoretically calculated (based on quantum mechanics or molecular models) or experimentally determined (by understanding the wetting behavior¹⁴ or the nucleation mechanics²).

The second approach, referred to as a pragmatic approach, measures a "practical adhesion," parameter: either the bond strength or the adhesion strength as obtained in common mechanical tests. This bond strength is considered to be a function of the basic adhesion coupled with other factors, such as substrate surface finish, impurity contamination, fracture trajectory, etc. Deryagin¹⁵ clarified the distinction between these approaches by noting that adhesion can be regarded as two separate processes. On the one hand, it is a process whereby two bodies are brought together and attached; this is the basic adhesion described by Chapman and Mittal. On the other hand, it is the process of breaking bonds between bodies that are already in contact.

In an adhesion measurement, the second adhesion process is clearly the more important. It is essential to recognize that, although these two processes are related, they are not equivalent. The difference can be illustrated by the following results. Recent theoretical calculations^{16,17} and fracture mechanics experiments in a homogeneous material have revealed that the theoretical calculated energy involved in the formation of a bond is only one tenth the energy needed to break a bond in a fracture situation. The implication of this result is that it can require more energy to break a bond than to form a bond. It can be expected that the same situation exists in adhesion. Experiments on peeling a film from a substrate (Peeling test) confirmed this

speculation. Deryagin¹⁵ stated that the work of film peeling was found to be the order of 10^4 to 10^5 ergs/cm² some 2 or 3 orders of magnitude greater than the energy of chemical bonding. Thus, the academic approach is indeed of academic interest only. A meaningful adhesion measurement should be able to measure the resistance of the interface separation regardless of whether the interface is ideal, strengthened (interlocking) or weakened (contamination). Mechanical test clearly possess such a capability. However, inconsistent results and unsatisfactory correlations between different tests have impeded the development of such tests. A better understanding of these tests is clearly needed.

Recent progress in fracture mechanics offers an opportunity for a better understanding of the above problems. A mechanical test can be classified (according to its ability to provide a true measure of the resistance of the interface separation) as a fracture test or a fracture mechanics test. A fracture test measures the critical force (σ_f) or stress needed for separation. A fracture mechanics test measures a parameter characteristic of adhesion. This fracture parameter is fracture toughness of the interface. It appears in the form of a stress intensity factor, K_c , or a strain energy release rate, G_c . The relationship between fracture strength (σ_f) and fracture toughness (K_c) is given by the following equation:¹⁸

$$\sigma_f = \frac{K_c}{\sqrt{a} Y}$$

where a is the length of the crack along the interface that initiates the separation and Y is a function of specimen geometry. The above equation indicates that the measured fracture strength is dependent on fracture toughness, specimen, geometry and interfacial crack length. A fracture test which measures only the fracture strength σ_f without taking account of the specimen geometry and the interfacial crack size is thus subject to a wide variation. On the other hand, a toughness value, measured in a fracture mechanics test, is independent of specimen geometry and shows less variation.* In addition, it can be expected to exhibit a better correlation with other thin film physical properties.** Hence, it is generally more desirable to measure the fracture toughness than the fracture strength. Future effort should then concentrate on developing fracture mechanics tests. However, it should be noted that, although the fracture strength is not an unique material property (it depends on the test method etc.) incorporation of the fracture strength data into a weakest link probability^{19,20} framework permits useful information to be deduced concerning the mechanical durability of the interface. Specifically, the probability of failure ϕ , is given by

* The variation of fracture toughness is usually normal with a small standard deviation while the fracture strength usually conforms to an extreme value distribution.

** See Experimental Results, Section 3.

$$\Phi = 1 - \exp \left[- \int_V dV \int_0^\sigma g(s) ds \right]$$

where V is the volume of test specimen and $g(s) ds$ is the number of flaws per unit area with a strength between s and $s + ds$. The strength distribution $g(s)$ can frequently be characterized by a Weibull function,^{21,22}

$$\int_0^\sigma g(s) ds = \left(\frac{S - S_u}{S_o} \right)^m$$

where S_o , S_u and m are Weibull parameters. A series of tests on specimen with known geometry determines the fracture probability, and subsequently calibrates the Weibull parameters. Once the strength distribution is known, the fracture probability (under different test conditions or with different geometries) can be predicted at a given stress level.

Most adhesion tests described in the literature are fracture tests. It is important to realize that certain fracture tests can be converted into fracture mechanics tests by introducing a crack length measurement step. A list of adhesion tests is given in Table I; a brief description of each test is presented below.

1.2.1 Fracture Test

a. Direct Pull off Method²³⁻²⁴

A pulling device is attached to the film surface and a force applied normal to the film/substrate interface (using a tensile testing machine). The critical force at which the film is pulled off is related to the adhesion strength. There are several difficulties

involved in this test: Firstly, alignment must be perfect to ensure that a uniform tensile stress exists across the surface. Secondly, the attached pulling device may damage the film surface and probably disturb the interface properties. Thirdly, the results are difficult to interpret because the film is detached through a mixed mode of tensile and shear fracture.

b. Electromagnetic Test²⁵

The principle of this test is to use the interaction between an electric current in the film and an external magnetic field to produce a force normal to the interface that is needed to detach the film from the substrate. This is an improvement over the direct pull off method, which a normal force is applied without attaching a pulling device to the film surface. However, thin film has to be patterned in this test to allow the electric current to pass through. It is very convenient to use this method for electronic microcircuit films. Otherwise a considerable inconvenience arises when the film is patterned. Another limitation of this test is the heating effects, created by the electric current, produces a thermal stress.

c. Pulse Laser Method^{26,27}

A pulse laser machine is used to deliver a high energy pulsed laser beam on the backside of the substrate, which is coated with an absorbing layer. The incident radiation is converted rapidly to thermal energy; this generates a compressive stress wave which propagates through the substrate, toward the film substrate interface. Then the reflection of the compressive wave from the surface gives rise to a tensile stress and leads to removal of the film.

A threshold incident power at which the film is detached from the substrate is related directly to the adhesion strength. This test can also be performed using a pulsed electron beam instead of a pulsed laser beam.

It was claimed that the main advantage of this test over other tests is that a film can be detached from a substrate without any prior disturbance. However, this advantage seems to be overshadowed by many other disadvantages. Firstly, the equipment is large, expensive and complex. Secondly, the film has to be patterned into dots smaller in diameter than the incident beam. If not, the film will tear and then spall off. Thirdly, considerable uncertainties are involved in the stress wave measurement (such as destructive interference, damping effects, thermal energy dissipation, etc.), additionally served unfavorable phenomena often develop in response to the shock wave, such as substrate shattering or decomposition, interface structural changes, and stress induced recrystallization, etc.

d. Ultrasonic Test²⁸

The principle of this method is to create a normal force at the film/substrate interface by employing an ultrasonic source. A film is attached to the free end of a metal cylinder and vibrated longitudinally at a convenient ultrasonic frequency. The film is detached from the substrate when the force due to acceleration exceeds the adhesion force at the interface.

This method is potentially capable of evolving into a quantitative technique for measuring adhesion provided that the crack size can be determined at some point during the test. At present, this method

measures only the average value of the adhesion strength. Additionally, if the mass of the film used to produce acceleration is small (either the film is very thin or low density), the frequency needed to produce enough acceleration increases so substantially that it is not possible to conduct the test within the equipment capability. It is also noted that the adhesion of thick films cannot be extrapolated to obtain the adhesion of thin films.

e. Ultracentrifugal Method²⁹⁻³⁰

This is also a promising method but has the same limitations described in the previous test. A film/substrate specimen is suspended inside the center of a vacuum chamber (in the form of a rotor) by a magnetic field. Another rotating magnetic field is used to spin the specimen at high speed and to create a centrifugal force. The film is detached from the substrate at a critical rotation speed. The adhesion strength is related to this critical rotation speed, the film density and geometry. This method measures an average adhesion strength.

f. Scotch Tape Test³¹⁻³²

This is a very old and quantitative method for testing adhesion. A pressure sensitive tape is pressed onto the film and then stripped. This adhesive strength of the film is ranked according to whether the film is completely removed, partially removed, or not removed at all. This inexpensive, simple and quick test has been used as a routine screening test. The disadvantages are obvious: it cannot provide a quantitative measure of adhesion. The results are affected by the type of tape, the pressure applied, and the stripping manner. Another

restriction is that it is applicable only when the adhesion between the film and the substrate is less than the adhesion between the film and the tape.

g. Scratch Test³³⁻³⁵

This is a relatively new and popular test. A stylus, usually a chrome steel ball, a tungsten carbide, or diamond tip, is drawn across the film surface with the substrate moving at a controlled speed. The load normal to the interface applied to the stylus tip is gradually increased until the film is completely cut through and leaves a clear channel. This critical load is related to the adhesion strength of the film.

It is a very simple and quick test, ideal for routine testing. The equipment is inexpensive and easy to set up. However, this test has been subject to many criticisms. It has been shown that a film can be detached before the formation of a clear track and it may also be thinner to optical transparency without being removed. The mechanism involved in stylus motion is also quite complex. It involves elastic/plastic deformation, film tearing and material pile-up.

One way to minimize these problems is to keep the substrate stationary. The test then becomes a hardness indentation and the adhesion strength can be obtained from indentation fracture analyses. A detailed description of the hardness indentation technique is given in Section 2.

h. Blister Method³⁶⁻³⁷

This method is used primarily for polymer film coatings. The principle of this method is to inject a fluid (gas or liquid) beneath

the coating, at the coating substrate interface, and the hydrostatic pressure is increased until the coating begins to detach from the interface. (If the crack length and the hydrostatic pressure were measured, the fracture toughness could be determined using this technique.) This method has only been applied to thick coatings.

1.2.2 Fracture Mechanics Tests

a. Peel Test³⁸

This is a very popular test. It is an improvement over the scotch tape test. The film can be peeled off from the substrate by applying a force either directly on to the film or through an adhesive tape pressed onto the film. This force is applied over a specific width of the film, at a specific angle to the film surface and at a controlled rate. The peeling energy (Fracture energy) can be expressed in terms of the work done per unit area, since both the force applied and the length of the film detached from the substrate can be measured.

Although the peeling test measures a fracture energy of interface, the interpretation of this energy remains ambiguous. For example, Chapman reported that the peeling energies measured, with or without a tape attached to the film, can be quite different (e.g., for gold films on soda lime glass). The energy measured with a tape on the film is 4 times higher than that without a tape. Also, Chen and Flavin³⁹ indicated that the inelastic deformation of the film contributes to the peeling energy; by giving an erroneous measure of adhesion. In addition, the peeling energy is highly dependent on the rate of peeling and on the width of film over which the force is applied.

b. Constant Compliance Test¹⁰

This test was developed originally for adhesive joint testing. A tapered double cantilever beam adhesive specimen is under Mode I loading. The energy release rate G can be expressed as a function of load applied, the beam thickness, elastic modulus, the beam height at the crack tip and the crack length. Bascom and Bitner¹⁰ applied this technique to thick film adhesion. A single beam test specimen was devised. The beam was cut from the brass plate shaped into a specific form and dip soldered onto a thick film specimen. The principal disadvantage of this test concerns the extensive specimen machining needed to conduct. Also, residual stresses from soldering can result in erroneous measurements.

c. Applied Moment Test¹⁰

This is another form of double cantilever beam test. Instead of applying a force normal to the pre-existing crack, a constant moment is applied. The same specimen preparation disadvantages that apply to the constant compliance test also apply to the constant moment test.

In view of the complexity and the restricted application of the currently available fracture mechanic tests, a new test method based on hardness indentation is introduced.

2. INDENTATION FRACTURE

The "well developed" deformation/fracture pattern which results from indentation of the surface of a homogeneous brittle solid with a Vickers pyramid is shown schematically in Figure 1. The elastic/plastic nature of the deformation response has been analyzed in the first part of the thesis. Two distinct crack systems are apparent; the "median/radial" system comprising two orthogonal, semi-circular cracks parallel to both the load axis and an indentation diagonal, and the penny-shaped "lateral" crack parallel to the surface and centered near the base of the plastic deformation zone. Both crack systems develop mainly during the unloading half cycle and are driven primarily by the residual elastic/plastic stress field.

Recent analysis of these crack systems has provided improved understanding of the behavior of flaws in brittle surface, and enabled development of predictive models for material degradation processes. The radial/median crack system is pertinent to strength degradation (static contact,⁴⁰⁻⁴¹ particle impact,⁴²⁻⁴³ machining damage⁴⁴) and the lateral crack system to material removal processes (erosion and wear).⁴⁴⁻⁴⁵ In addition, the derivation of the functional dependence of the radial crack dimension on the pertinent parameters (contact load P , material hardness H , elastic modulus E , and toughness K) has led to a simple and efficient technique of toughness measurement.⁴⁷⁻⁴⁸ The method has been extended to measure the interface toughness of very thick coatings by sectioning normal to the interface and aligning the indentation such that one radial crack propagates

along the interface.⁴⁹ However, the method cannot be applied to thin coatings (less than ~1 mm) because of free surface effects on the crack propagation.

A more suitable basis for the present film adhesion measurements is provided by the lateral crack system. The film surface parallel to the interface is indented, and the lateral crack is induced to propagate along the interface (Fig. 2). Then measurements of the crack radius c , the indentation load P , the indentation diagonal $2a$, and film thickness h , will be demonstrated to provide a measure of the toughness K_C^{inter} . Lateral cracks in the homogeneous material usually, but not always, form near the base of the plastic zone. However, the driving force for lateral crack propagation exists over a range of depth and the actual depth at which a crack propagates is influenced by the availability of crack nucleation sites.⁵⁰ The proposed test is based on the rationale that an interface (in the vicinity of the plastic zone) with a lower toughness than that of either the film material or the substrate material will be the preferred site for lateral crack formation. When fracture cannot be induced at the interface (but occurs in the film or substrate) it can be immediately concluded that the interface toughness is at least as large as that of the weaker material constituent.

Further observations also indicated that a preferred interfacial lateral crack was developed in ZnO/Si systems (see Fig. 4). The similar material properties of ZnO and Si simplifies the fracture analysis in Sec. 4. Additionally, the deposition of ZnO film using a

planar magnetron sputtering technique is much faster than depositing poly Si using low temperature CVD method. All the subsequent experiments were conducted on ZnO/Si systems. The present study is confined to combinations of ZnO on Si and Si on Si because the materials have similar values of both hardness and elastic modulus (the parameters that dictate the magnitude of the residual stress which provides the crack driving force). This choice simplifies the theoretical analysis and permits direct correlation between theory and experiment. The effects of a mismatch in hardness and/or elastic modulus will be addressed in a subsequent analysis.

3. EXPERIMENTAL OBSERVATIONS

The viability of the indentation technique for measuring adhesion was firstly established by examining the influence of a sub-surface interface on the development of lateral fractures. In most cases, subsurface lateral crack cannot be seen under a scanning electron microscope. An optical microscope is thus used to observe lateral cracks under a Nomarsky interference contrast mode. Lateral cracks obtained in a Si single crystal are compared with those that develop at the interface between a 2 μ m polycrystalline Si film deposited onto single crystal Si (Fig. 3). A circular sub-surface lateral crack, located at the interface, was clearly evident in the latter, while a smaller, less distinct lateral crack developed in the single crystal. These observations indicate that interfaces are preferred sites for the lateral fracture process, thereby satisfying the basic prerequisite for applying the indentation technique to the adhesion problem. Further observations also indicated that a preferred interfacial lateral crack was developed in ZnO/Si systems (Fig. 4). The similar material properties of ZnO and Si simplifies the fracture mechanics analysis in section 4. Additionally, the deposition of ZnO film using a planar magnetron sputtering equipment is much faster than depositing polycrystalline Si film using low temperature CVD method. All subsequent experiments were conducted on ZnO/Si systems.

It can be anticipated from previous work^{12,13,45} in indentation fracture that the radius of the lateral crack will depend on the indentation load and the film thickness (i.e., the crack location) in addition to the interface toughness (the parameter of interest). A

typical influence of the load on the crack length is illustrated for ZnO/Si in Fig. 5. Quantitative application of the indentation method will require determination of the functional dependence of the crack length on each of these variables. This issue will be addressed in Section 4. At this juncture, some important trends in adhesion are established. This is achieved by comparing crack lengths for the same load and film thickness obtained on indented samples of ZnO/Si, prepared under different conditions. In some instances, the adhesion trends are correlated with other property measurements, in order to demonstrate the general utility of indentation as a reproducible, comparative method for determining adhesion.

The indentation results obtained at 300 g. for the following two systems, $6\mu\text{m ZnO}/1000\text{\AA SiO}_2/(\text{111})\text{Si-N}$ type and $6\mu\text{m ZnO}/1500\text{\AA Pt}/500\text{\AA Ti}/(\text{111})\text{Si-N}$ type, are illustrated in Fig. 6. It is noted that faceted lateral cracks develop in the latter, indicating the existence of preferred paths of fracture resistance (typical of lattice orientation effects in single crystals), and that the average crack radius for this system is smaller. Superior adhesion thus obtains for the system with the Pt/Ti interlayer.* Independent measurements of the acoustic properties⁵⁰ indicate appreciably larger acoustic signals for the latter. A correlation between adhesion and acoustic properties indicates that deposition conditions that develop a good quality

* It should not be concluded that the Pt/Ti interlayer invariably provides superior adhesion. Other film formation parameters are of substantial importance with regard to adhesion.

interface also lead to films of high quality which, in turn, provide good acoustic properties.

Another series of tests on $10\mu\text{m ZnO}/1000\text{\AA SiO}_2/(111)\text{ Si}$ samples are summarized in Fig. 7. One sample exhibits superior adhesion to the other two, as manifested in a faceted lateral crack configuration, with a smaller average crack radius. Sectional views of these samples (Fig. 8) indicates that the sample with the superior adhesion consists of a ZnO film with columnar grains, oriented with (0001) normal to the substrate surface. This film also exhibits greater optical transparency. Additionally, X ray rocking curve experiments show that the full width at half maximum of the (0001) diffraction peak is smaller for the sample with superior adhesion than for the other samples (1.9° compared to 2.8°). Other studies have indicated that films with a highly oriented structure, good optical quality and columnar grain geometry typically provide optimum acoustic properties.⁵¹⁻⁵⁴ Again, therefore, the measure of adhesion obtained by indentation seems to reflect trends in other important physical properties.

The sensitivity of the indentation test to inferior adhesion is demonstrated in Fig. 9. Very large lateral cracks develop on poor quality films; in some instances causing sections of the film to be removed (Fig. 9b). The variability in the extent of lateral fracture obtained at various locations over the surface indicates that adhesion in such films exhibits substantial spatial variation (good quality films show very little scatter in the lateral crack dimension).

Finally, the application of indentation tests, as a simple means for monitoring trends in adhesion is emphasized. For this purpose, 10 μ m ZnO/Si samples have been annealed in air and in vacuum and then the lateral fracture extension determined in each case (Fig. 10). It is immediately evident that vacuum annealing substantially enhances the adhesion, while annealing in air causes a corresponding degradation.

4. THE INTERFACE TOUGHNESS

A quantitative measure of the interface toughness can be provided by developing an adequate model of lateral crack extension. The extension of well developed indentation fractures has recently been subject to successful analysis by treating the indentation plastic zone as a precompressed spring that provides the driving force for crack extension, and relaxes as the crack extends.^{11,12} This same approach can be used to anticipate the crack extension c along an interface, located at a depth, h , beneath the surface (Fig. 11). The analysis in this case differs from that in a homogeneous material¹² only in the treatment of the depth h (for interface cracks h is constant and equal to the film thickness, whereas cracks in a homogeneous material are located at the base of the deformation zone and h varies with indentation load).

4.1 Analysis

Based on the previous analysis,^{11,12} the residual driving force P_r for the crack extension can be expressed, using the analog of a precompressed spring, as

$$\frac{P_r}{P_{r0}} = 1 - \frac{U}{U_{r0}} \quad (1)$$

where U is the crack opening displacement when the load is removed, P_{r0} and U_{r0} can be treated as two spring constants. The above equation states that when the force exerted by the spring element is in the fully compressed state, i.e., $P_r = P_{r0}$, the crack opening

displacement U is zero. On the other hand, if the spring is fully relaxed, i.e., $P_r=0$, the crack opening displacement becomes U_{ro} . Since P_{ro} and U_{ro} are functions of the peak load \hat{P} , and the material constants (E,H) , they can then be expressed (Appendix I), as follows:

$$P_{ro} \sim (E/H)^{3/5} \hat{P} \quad (2)$$

$$U_{ro} \sim (H/E)^{4/5} (\hat{P}/H)^{1/2} \quad (3)$$

The crack opening displacement U is related to the residual driving force P_r through the following equation

$$U = \lambda P_r \quad (4)$$

where λ , the compliance of the film, is related to the lateral crack length c based on the thin plate theory. It is given by,¹²

$$\lambda = \frac{AC^2}{Eh^3} \quad (5)$$

where A is a constant, E and h are the elastic modulus and the thickness of the film. The relationship between the residual driving force and the lateral crack length is thus established. It is achieved by substituting eq. (4) into eq. (1):

$$P_r = \frac{P_{ro}}{1 + \lambda \frac{P_{ro}}{U_{ro}}} \quad (6)$$

It is necessary in the next step to relate the residual driving force to the interface toughness, K_{IC}^{int} , and the lateral crack length.

The stress intensity factor K for plane strain fracture is given by

$$K = \left[\frac{GE}{1-\nu^2} \right]^{1/2} \quad (7)$$

where the strain energy release rate G can be expressed as⁵⁵

$$G = \frac{P_r^2}{2} \frac{d\lambda}{d(\pi c^2)} \quad (8)$$

The stress intensity factor K is thus related to the residual driving force by combining eq. (5), (7), (8) and eliminating G and λ . It reduces to

$$K = \frac{\Lambda P_r}{h^{3/2}} \quad (9)$$

where

$$\Lambda = \left[\frac{A}{2(1-\nu^2)\pi} \right]^{1/2}$$

Finally, the crack length c is related to the load, the material properties and the interface toughness by substituting eq. (2), (3) and (6) into eq. (9) and letting $K=K_{IC}$. The result is

$$c = \alpha \left(1 - \frac{P_0}{\hat{p}}\right)^{1/2} \hat{p}^{1/4} \quad (10)$$

where P_0 is a threshold load for crack formation and α is given by:

$$\alpha = \left[\alpha_1 \frac{h^{3/2}}{K_{IC}} E^{1/5} H^{9/10} \right]^{1/2} \quad (11)$$

where α_1 is a material independent coefficient that can be determined by calibration, on a homogeneous material with known H and K_{IC} . Once α_1 is known, subsequent experimental determination of α , obtained by fitting crack lengths at several load levels to eq. (10), permits K_{IC}^{inter} to be obtained from eq. (11); provided the film thickness h is also measured (H is determined directly from \hat{p} and the indentation diagonal).

4.2 Results

The calibration of the coefficient α_1 , based on glass indentation experiment,¹² yielded a value of 5.5×10^{-14} . Indentations were carried out on a ZnO/SiO₂/Si system for several different loads and the crack lengths were measured. The results are shown in Fig. 12. A fit of the data to eq. (10) indicates that the threshold load is $P_0 = 3N$ and that $\alpha = 4.5 \times 10^{-5} mN^{-1/4}$. Inserting the film thickness $h = 10\mu m$ and the hardness $H = 8.5GPa$ into eq. (11), the interface toughness is determined to be $0.1 MPa\sqrt{m}$. This compares with material toughness of, $0.5 MPa\sqrt{m}$ for Si, $\sim 0.7 MPa\sqrt{m}$ for SiO₂ and $\sim 1MPa\sqrt{m}$ for ZnO. The interface thus exhibits a lower fracture toughness than the constituent materials, as required for the observation of interface

fracture. Preliminary credence in the model is thus provided. Much additional experimentation is needed, however, to determine if the analysis correctly predicts trends in film thickness, load and interface toughness.

5. DISCUSSION AND CONCLUSIONS

A simple indentation test for measuring the adhesion of thin or thick films to substrates has been developed. The general utility of this test as a simple way for establishing trends in the adhesion of film systems, achieved by employing different deposition or post-deposition techniques, has been demonstrated. This was achieved by conducting experiments on various ZnO/Si systems. Important influences on adhesion of the interlayer material (Pt/Ti being preferred to SiO₂) and of the deposition conditions (columnar ZnO grain morphologies yielding superior adhesion) were discussed and correlated with the acoustic properties. Additionally, substantial effects of heat treatment procedures on the adhesion were detected in this manner. It should be stressed that the simplicity of the indentation technique renders it ideally suitable for trend determinations of this type. The technique can be used with small specimens (a few millimeters in length), no special specimen preparation is required, a standard hardness testing machine and optical microscope are the only equipment requirements, the adhesion measurements are reproducible, and results can be obtained routinely, quickly and with minimal material damage.

The development of indentation methods for the absolute measurement of interface fracture resistance has been studied. An analytic solution for well developed lateral cracks has been shown to conform quite satisfactorily with data obtained on a ZnO/Si system. For other film/substrate combinations where the material properties are not compatible

(the plastic zone created by the indentation may not retain the hemispherical shape), further analysis as well as experimental studies are needed to substantiate the fracture model. Thereupon, the method should be capable of providing direct information concerning the fracture toughness of interfaces.

APPENDIX I. EVALUATION OF P_{ro} and U_{ro}

The elastic/plastic mismatch stress generated around the plastic zone boundary provides information for parameters P_{ro}/U_{ro} . In the well developed crack system it has been demonstrated successfully that Eshelby's method⁵⁶ of solving inclusion problems can be applied to the elastic/plastic indentation problem. Thus, the P_{ro} and U_{ro} are evaluated in the following manner.

1) In an unstressed half space, remove a segment of material hemisphere with radius b from the indentation site.

2) Plastically deform the removed material by indentation over a contact radius a . Thus, irreversible strain is created by the expansion of the characteristic zone, the plastic zone, with radius b . If V is the volume of indentation and V is the volume of the characteristic zone, the configurational strain ϵ produced by indentation is given by

$$\epsilon = \frac{V}{V} \sim a^3/b^3 \quad (A-1)$$

The relation between b/a and the material constants E/H is given, in part I of this study, by

$$b/a \sim (E/H)^{2/5} \quad (A-2)$$

3) If the plastic deformation zone is restored elastically to its original dimensions, a hydrostatic compressive stress σ , given by

$$\sigma \sim E\left(\frac{v}{V}\right) \sim E(a/b)^3 \quad (A-3)$$

is generated across the outer boundaries of the plastic zone.

4) Reinsert the pressurized segment into the original cavity and allow the system to relax. The plastic zone can now be considered as a source of effective outward residual force. The residual force P_{ro} can be obtained, when there is no crack present, by integrating the hydrostatic compressive stress σ over the area of the plastic zone

$$P_{ro} \sim E\left(\frac{v}{V}\right)b^2 \quad (A-4)$$

U_{ro} is determined in terms of radial displacement of the zone boundary in going from the fully compressed to the fully relaxed state:

$$U_{ro} \sim v/b^2 \quad (A-5)$$

The parameters a and b are related to the indentation load, hardness and elastic modulus through the following equations:

$$a \sim (P/H)^{1/2} \quad (A-6)$$

$$b \sim (P/H)^{1/2} (E/H)^{2/5} \quad (A-7)$$

Hence, P_{ro} and U_{ro} are obtained by substituting eqs. (A-6) and (A-7) into eqs. (A-4) and (A-5):

$$P_{ro} \sim (E/H)^{3/5} p \quad (A-6)$$

$$U_{ro} \sim (H/E)^{4/5} (p/H)^{1/2} \quad (A-7)$$

REFERENCES

1. K. L. Mittal in Adhesion Measurement of Thin Films, Thick Films and Bulk Coatings, ASTM STP 640, K. L. Mittal Ed., pp. 5-17.
American Society for Testing and Materials, Philadelphia, PA, 1978.
2. D. S. Campbell, in Handbook of Film Technology, L. I. Maissel and R. Gland, Editors, Chapter 12, McGraw Hill Book Company, N.Y., 1970.
3. B. N. Chapman, J. Vac. Sci. Tech. II, 106-113 (1974).
4. K. L. Mittal, Electrocomponent Sci. Technol. 3, 21-42 (1976).
5. R. P. Arnard, Microelectronics and Reliability, Vol. 10, No. 4, 1971, pp. 269-275.
6. J. Savage in Handbook of Thick Film Technology, P. J. Holmes and R. G. Loasby, Eds., Electrochemical Publications Ltd., Ayr, Scotland, 1976, pp. 108-112.
7. T. R. Bullet and J. L. Prossner, Prog. Org. Coatings 1, 45-73 (1972).
8. T. T. Hitch, pp. 211-231 of Ref. 1.
9. R. J. Good, pp. 18-26 of Ref. 1.
10. W. D. Bascom, P. F. Becher, J. L. Batner and J. S. Murdoy, pp. 63-79 of Ref. 1.
11. B. R. Lawn, A. G. Evans and D. B. Marshall, J. Amer. Ceram. Soc., 63, 574-581, (1980).
12. B. R. Lawn, A. G. Evans and D. B. Marshall, work in preparation.
13. S. S. Chiang, Part I of this thesis.
14. L. E. Murr, pp. 82-97 of Ref. 1.

15. B. V. Deryagin, N. A. Krotova and V. P. Smilga, "Adhesion of Solids," (Consultants Bureau, N.Y.), 1978.
16. S. M. Wiederhorn, J. Amer. Ceram. Soc. 52, 99-105 (1969).
17. S. M. Wiederhorn, Int. J. Frac. Mech. 4, 171 (1968).
18. R. W. Hertzberg, "Deformation and Fracture Mechanics of Engineering Materials," (John Wiley and Sons, N.Y.), 1976.
19. B. W. Lindgren and G. W. McElrath, "Introduction of Probability and Statistics," (MacMillan, N.Y.), 1959.
20. A. G. Evans and R. L. Jones, J. Amer. Ceram. Soc. 61, 156-150, (1978).
21. W. A. Weibull, Ingenioersvetenskapsakad, Handl., 153, 1-55 (1939).
22. W. A. Weibull, J. Appl. Mech. 18, 293-297 (1951).
23. R. B. Belser and W. H. Hicklin, Rev. Sci. Instrum. 27, 293-296 (1956).
24. J. R. Frederick, and K. C. Ludema, J. Appl. Phys. 35, 256-257 (1964).
25. S. Krongelb, pp. 107-119 of Ref. 1.
26. N. C. Anderson and A. Goodman, KTIS Technical Report No. SC-DR-69-320, Sandia Lab, New Mexico, (1972).
27. J. L. Vossen, pp. 122-131 of Ref. 1.
28. S. Moses and R. K. Witt, Ind. Eng. Chem 41 2334-2338 (1949).
29. J. W. Beams, Science, 120, 610-625 (1954).
30. J. W. Beams, Tech. Proc. Amer. Electroplaters Soc. 43, 211-214 (1956).
31. J. Strong, Publ. A.S.P. 46, 18 (1934).

32. D. M Mattox and J. E. McDonald, J. Appl. Phys. 34, 2493-2494 (1963).
33. O. S. Heavens and L. E. Collins, J. Phys. Radium, 13 658-660 (1952).
34. P. Benjamin and C. Weaver, Proc. Roy. Soc. 254A, 163-176 (1960) and 254A, 177-183 (1960).
35. J. Ahn, K L. Mittal and R. H. MacQueen, 134-156 of Ref. 1.
36. E. Hoffman and O. Geogonssis, J. Oil. Color. Chem. Assoc. 42 267-269 (1959).
37. H. Dannenberg, J. Appl. Polymer Sci. 5, 125-134 (1961).
38. B. N Chapman, Aspects of Adhesion 6, 43-54 (1971).
39. W. T. Chen and T. F. Flavin, IBM, Journal of R & D 16, 203-213 (1972).
40. D. B. Marshall, B. R. Lawn and P. Chantikul, J. Mater. Sci. 14 2225-2235 (1979).
41. D. B. Marshall and B R. Lawn, J. Amer. Ceram. Soc., in press (Sept-Oct. issue, 1980).
42. A. G. Evans, in Fracture Mechanics of Ceramics (Eds. R. C. Bradt, D. P. H. Hasselman and F. F. Lange), Plenum Press, New York, 1978, pp. 303-331, Vol. 3.
43. S. M. Wiederhorn and B. R. Lawn, J. Amer. Ceram. Soc., 62, 66-70 (1979).
44. D. B. Marshall, B. R. Lawn and J. J. Mecholsky, J. Amer. Ceram. Soc. 63, 358-360 (1980).
45. A. G. Evans, M. E. Gulden and M. Rosenblatt, Proc. Roy. Soc. A361 343-365 (1978).

46. M. V. Swain, in Fracture Mechanics of Ceramics (Eds. R. C. Bradt, D. P. H. Hasselman and F. F. Lange), Plenum Press, New York, 3, 257-272 (1978).
47. A. G. Evans and E. A. Charles, J. Amer. Ceram. Soc., 59, 371-372 (1976).
48. G. R. Anstis, P. Chantikul, B. R. Lawn, D. B. Marshall, Submitted to J. Amer. Ceram. Soc.
49. P. Dokko and A. G. Evans, unpublished work.
50. B. T. Khuri-Yakub, unpublished work.
51. A. J. Bahr, R. E. Lee, F. S. Hickernell, C. B. Willingham, and T. M. Reeder, Ultrasonic Symposium Proceedings, pp. 202-205 (1972).
52. F. S. Hickernell, J. Vac. Sci. and Technol. 12, 879-883 (1975).
53. B. T. Khuri-Yakub, G. S. Kino and P. Galle, J. Appl. Phys. 46, 3266-3272 (1975).
54. T. Shiosaki, Ultrasonic Symposium Proceedings, pp. 100-110 (1978).
55. B. R. Lawn and T. R. Wilshaw, "Fracture of Brittle Solids," Cambridge University Press, Cambridge (1975).
56. J. D. Eshelby in "Progress in Solid Mechanics," (Ed. I. N. Sheddon and R. Hill), North Holland, Amsterdam, 2, 89 (1961).

Table 1. Comparison of Adhesion Test

Test	Type*	Comment **
Direct Pull off Method	F	S
Electromagnetic Test	F	S
Pulse Laser Test	F	S
Ultrasonic Test	F	S
Ultracentrifugal Test	F	S
Scotch Tape Test	F	
Scratch Test	F	
Blister Test	F	S
Peel Test	FM	
Constant Compliance Test	FM	
Contant Moment Test	FM	
Indentation Test	FM	

* Fracture Mechanics Test is designated by "FM". "F" indicates the Fracture test.

** Those that can be converted to Fracture mechanics test, provide that crack size is measured, are designated by S.

FIGURE CAPTIONS

Figure 1. A schematic showing crack patterns generated by Vickers indentation in a homogeneous material. a) Four radial cracks propagating along the indentation diagonal direction. b) Sectional view of the indentation; the dotted region represents the plastic zone created by indentation. The median crack coalesces with the radial crack to form a half-penny shaped crack. Lateral cracks propagate parallel to the surface.

Figure 2. A schematic of an indentation made on a film/substrate sample. The lateral crack propagates preferentially along the interface.

Figure 3. Optical micrographs of indentation of Si. a) An indentation made on single crystal (111) Si surface, indicating four radial cracks, and b) an indentation made on thin film specimen, $2\mu\text{m}$ poly Si/ 500\AA SiO_2 /(111)Si. A circular subsurface lateral crack, located at the interface, can be seen using an interference contrast method.

Figure 4. Optical micrograph of indentation on ZnO/Si system indicating a subsurface lateral crack was developed along the interface.

Figure 5. Optical micrographs illustrating the effect of the indentation load on the lateral crack length for a ZnO/Si system. a) 5 N and b) 10 N.

Figure 6. Optical micrographs of 300 g indentation made on a) $6\mu\text{m}$ ZnO/ 1000\AA SiO_2 /(111)Si-N type, b) $6\mu\text{m}$ ZnO/ 1500\AA Pt- 500\AA Ti/(111)Si-N type. The average crack radius is smaller in the latter, indicating a superior adhesion.

Figure 7. Optical micrograph of 1000 g indentations on three 10 μm ZnO/1000Å SiO₂/(111)Si samples deposited under different conditions. (c) shows better adhesion than (a) or (b), as manifest in a faceted lateral crack configuration, with a smaller average crack radius.

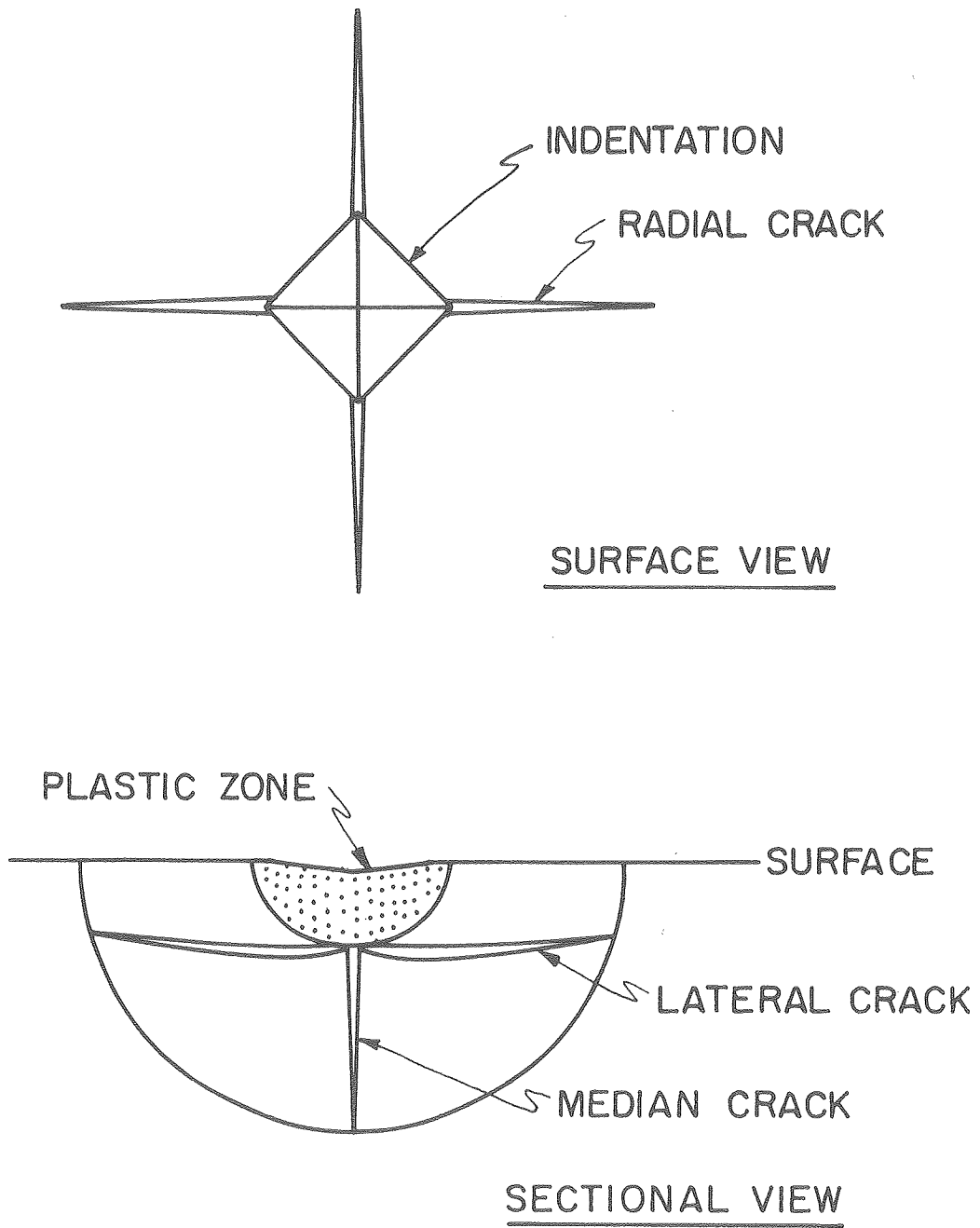
Figure 8. Scanning electron micrographs of fracture surfaces through the three samples shown in Fig. 7. Sample (c), which exhibits superior adhesion, shows a columnar grain structure in the ZnO film.

Figure 9. Optical micrographs indicating variations in the lateral crack size for a sample indented at different locations. This film exhibits poor and variable adhesion.

Figure 10. Optical micrograph of 1000 g indentations on 10 μm ZnO/(111)Si samples annealed at 1000°C for 1 hr in different atmospheres. (a) as deposited sample (b) annealed in air. Film peeled off dramatically after indentation indicating adhesion is very poor. (c) annealed in vacuum at low oxygen partial pressure, adhesion is improved as compared to (a). (d) annealed in vacuum at extra low oxygen partial pressure. Both the hardness and the adhesion of the film exhibited the greatest improvement.

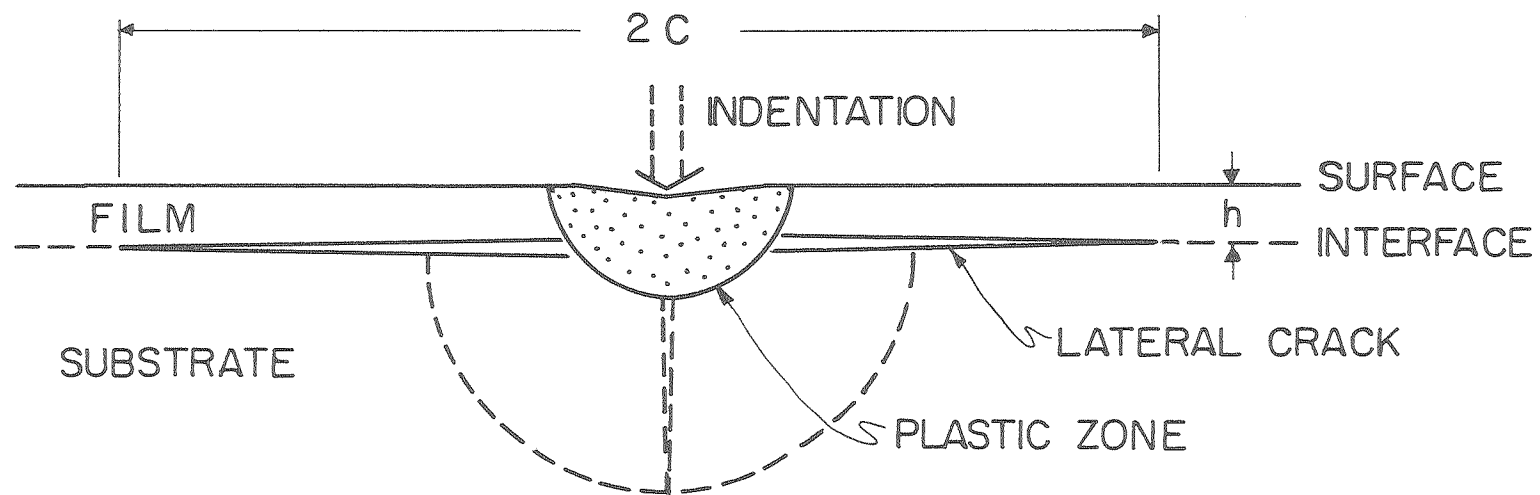
Figure 11. A schematic of the indentation model indicating the residual force associated with the plastic zone that acts as the driving force for lateral crack extension.

Figure 12. Dependence of the lateral crack length on the indentation load. The specimen is 10 μm ZnO/1000Å SiO₂/(111)Si.



XBL8010-6085

Fig. II-1



XBL8010-6083

Fig. 11-2

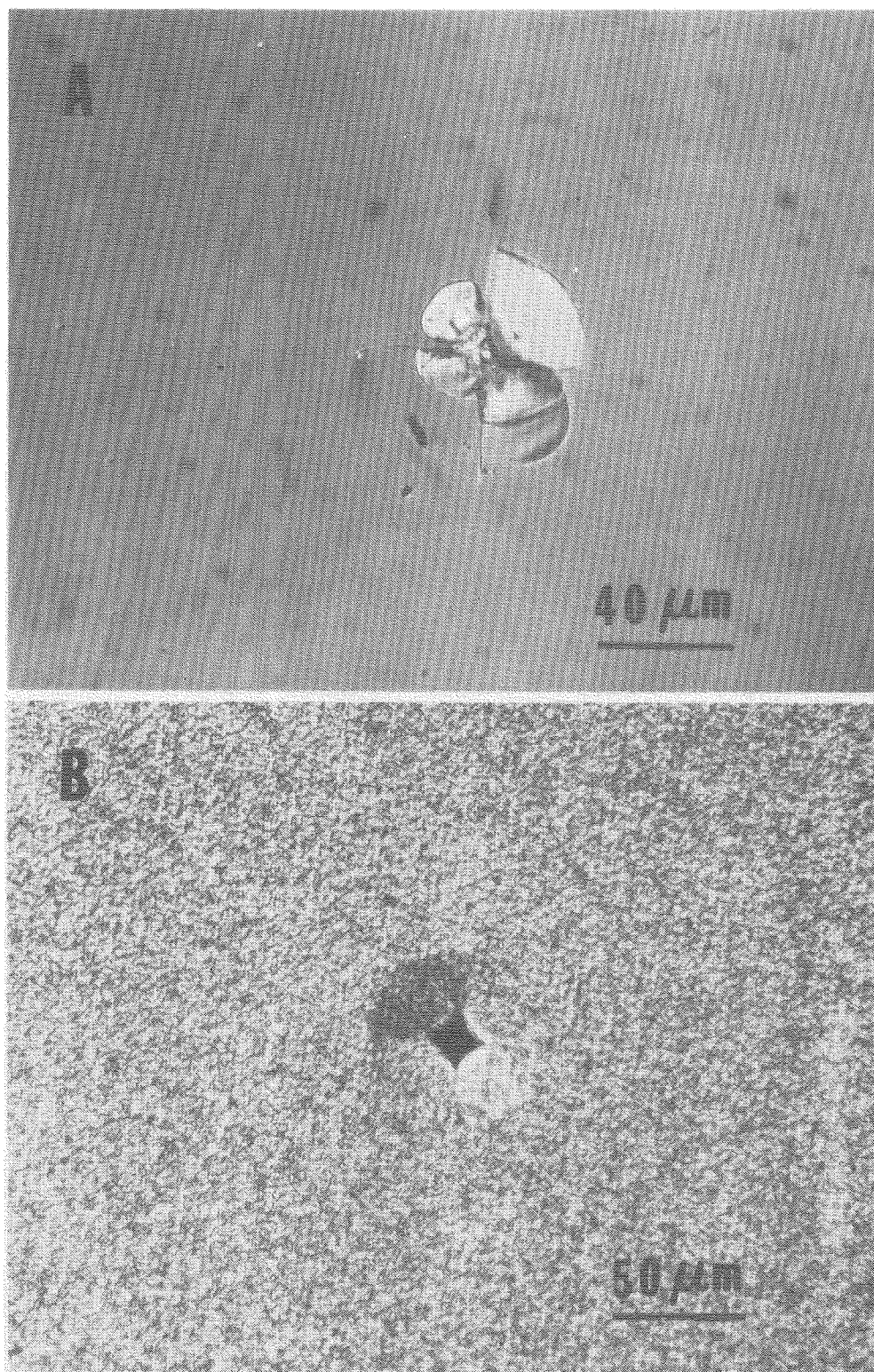


Fig. II-3

CBB807-08223

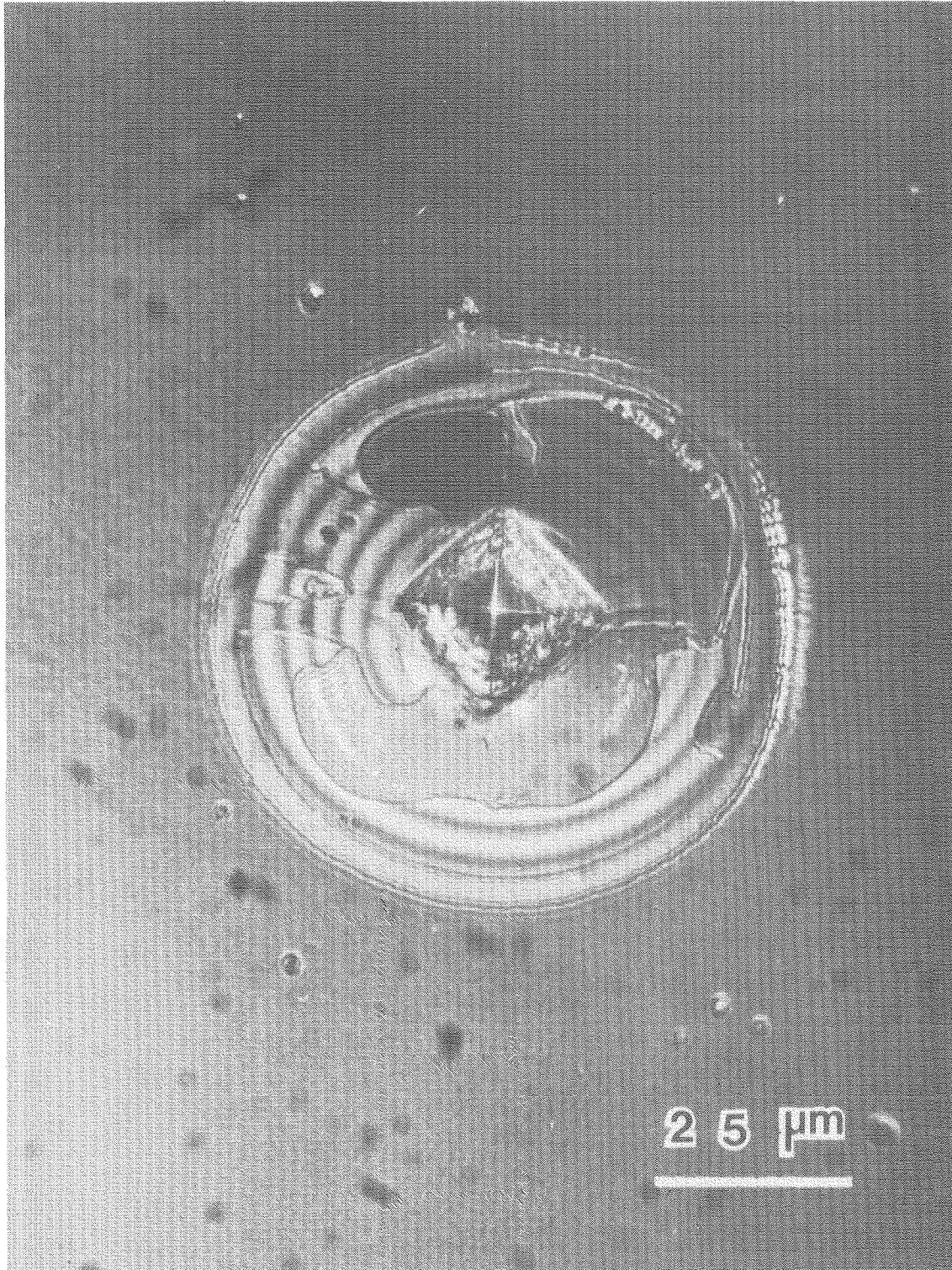


Fig. II-4

XBB807-8229

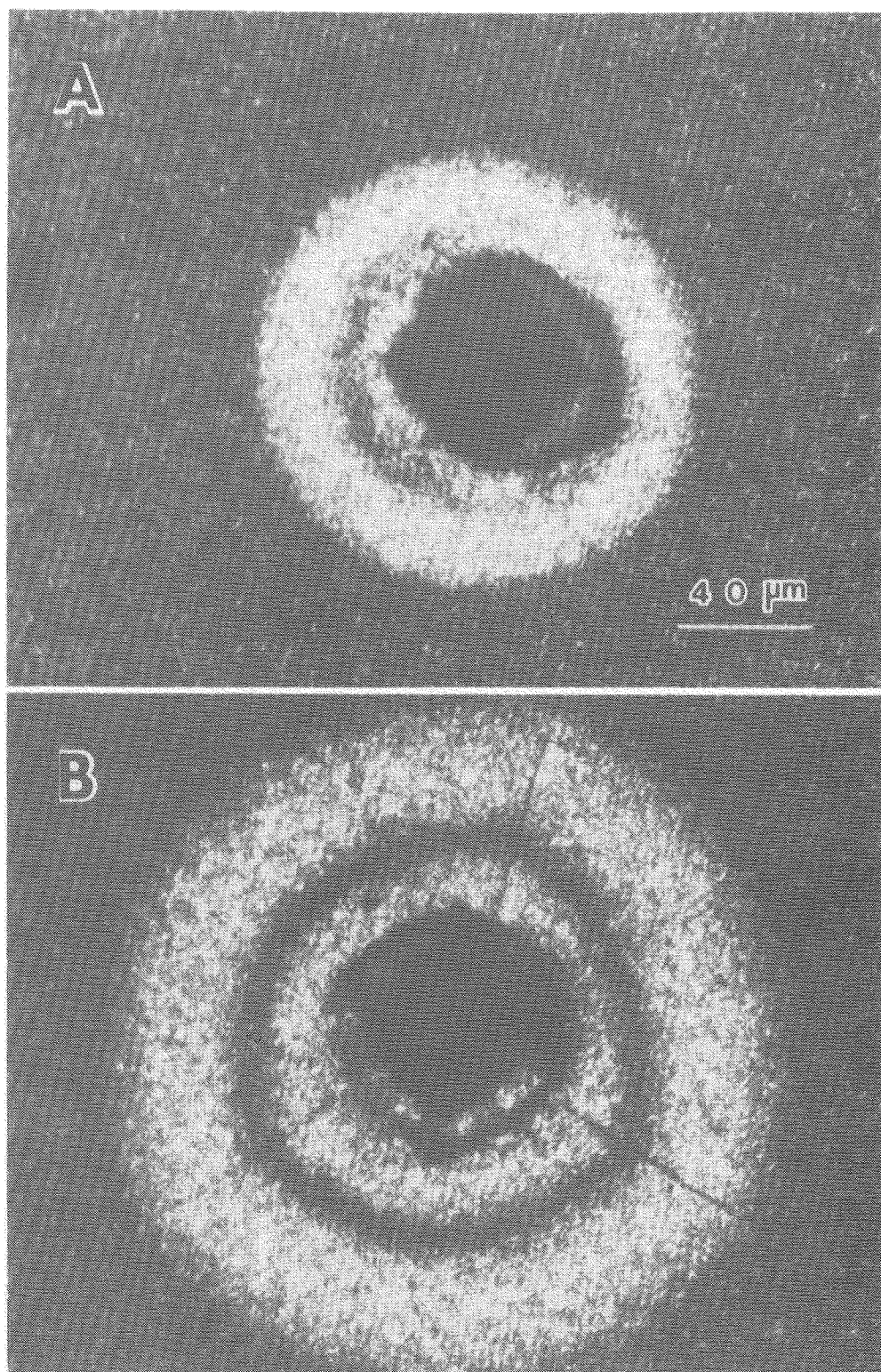


Fig. II-5

XBB807-8227

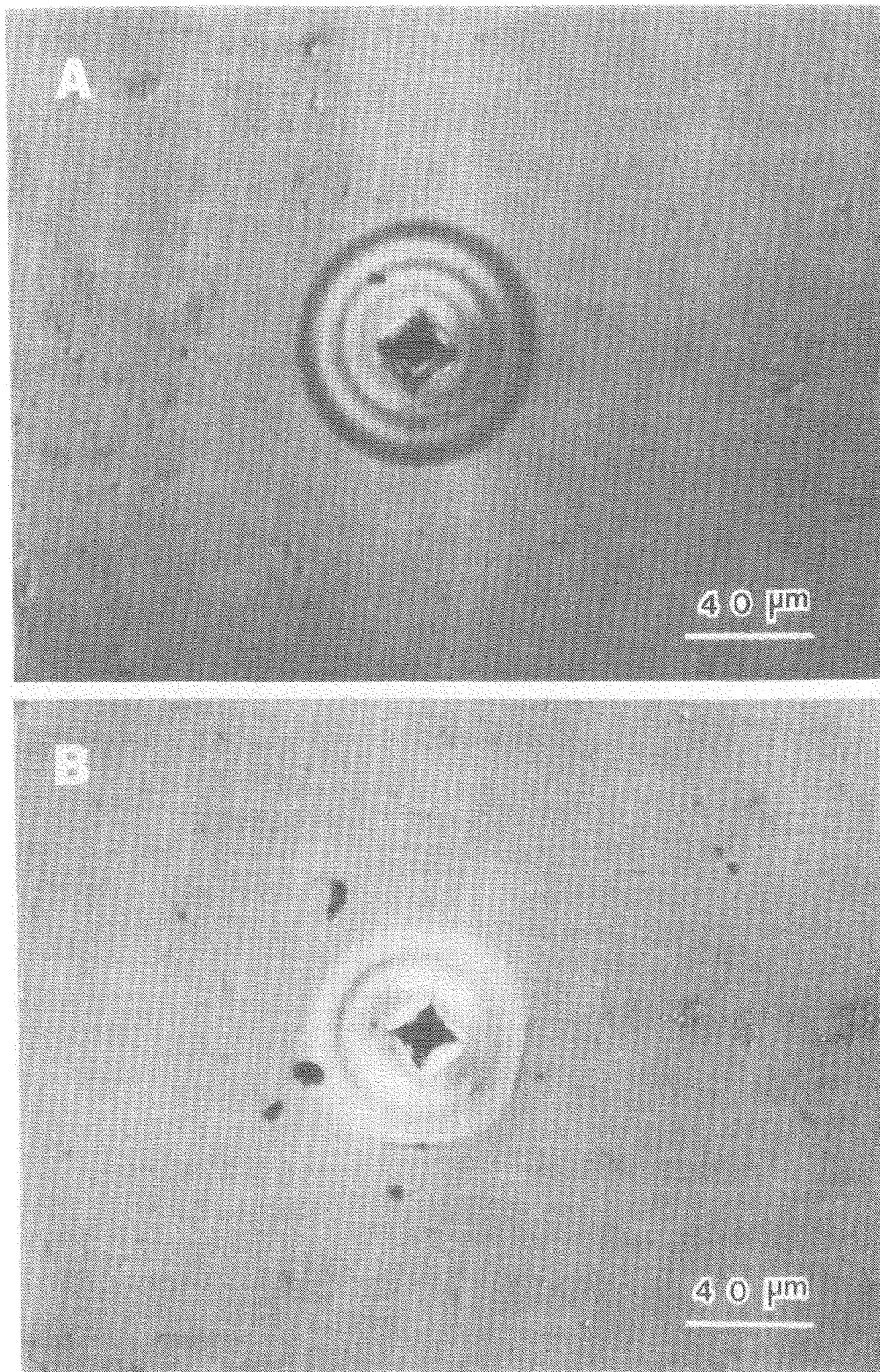


Fig. II-6

XBB807-8163

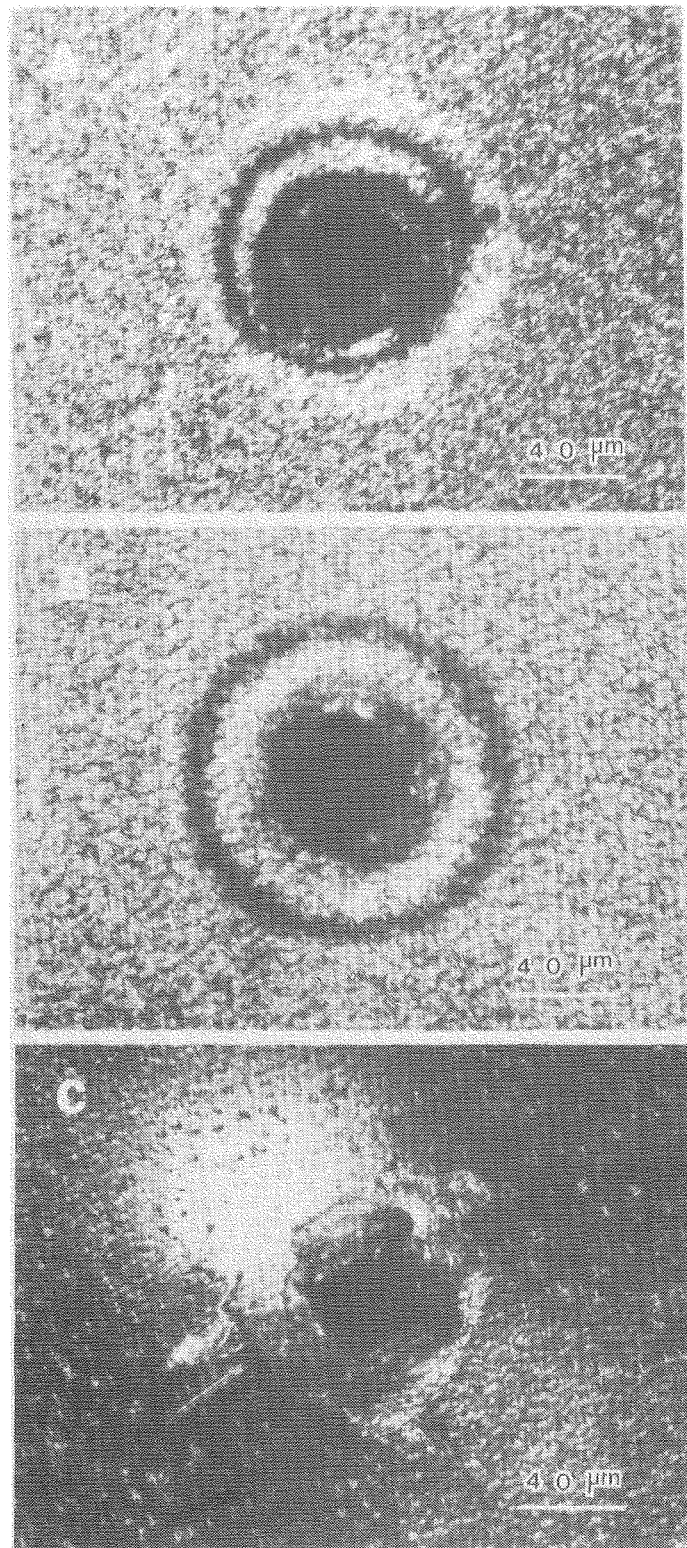


Fig. II-7

CBB807-8161

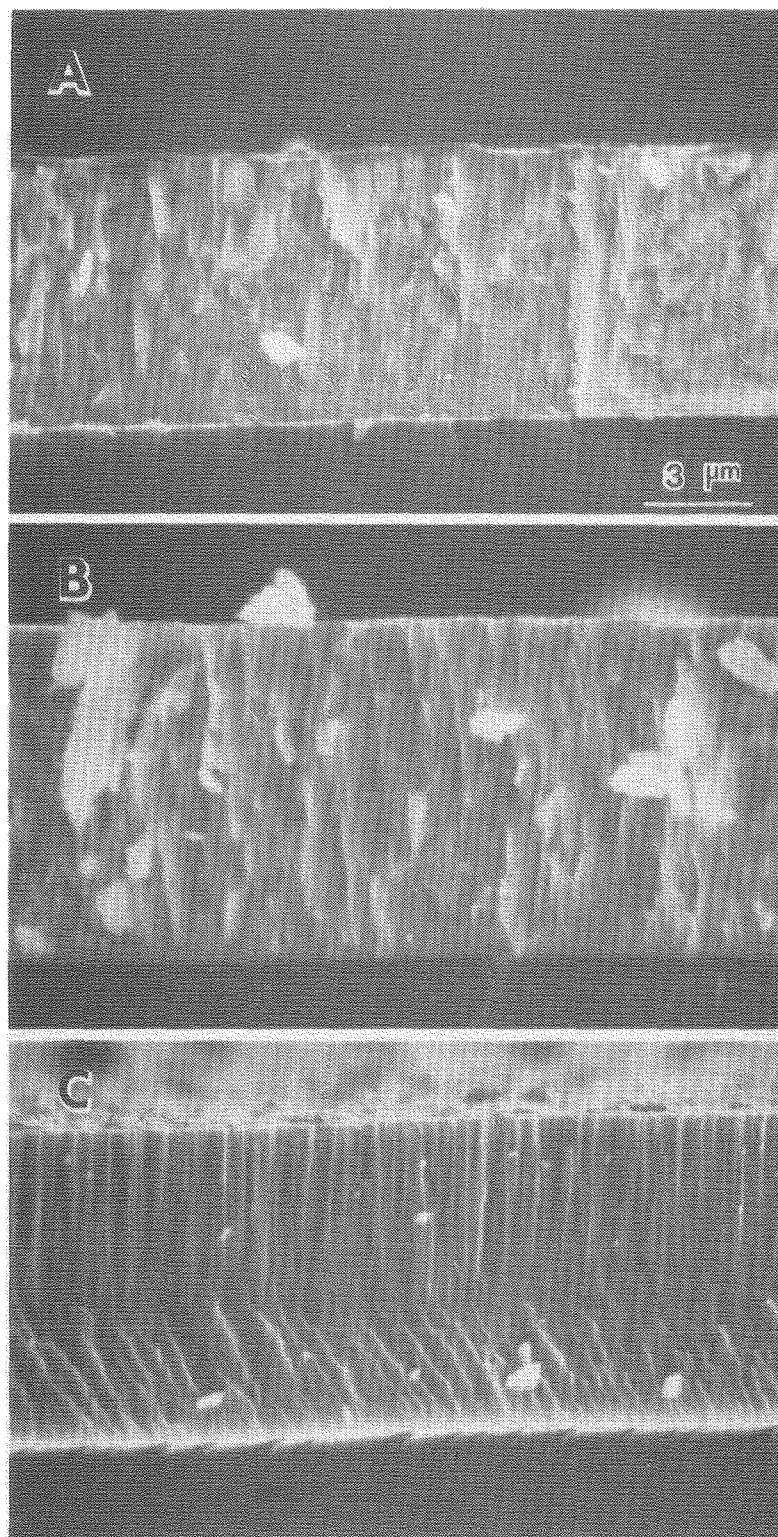


Fig. II-8

XBB807-8232

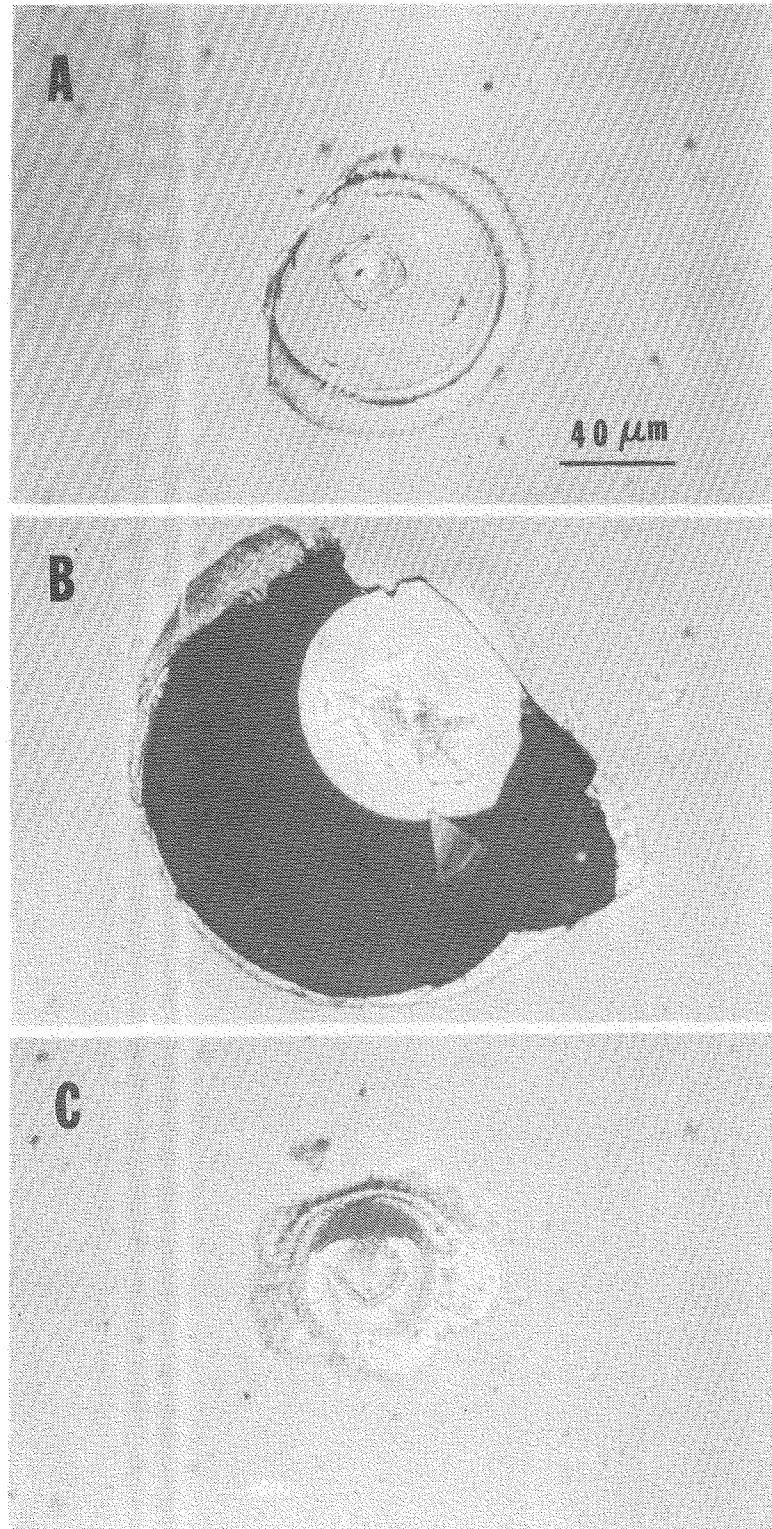


Fig. II-9

CBB807-08225

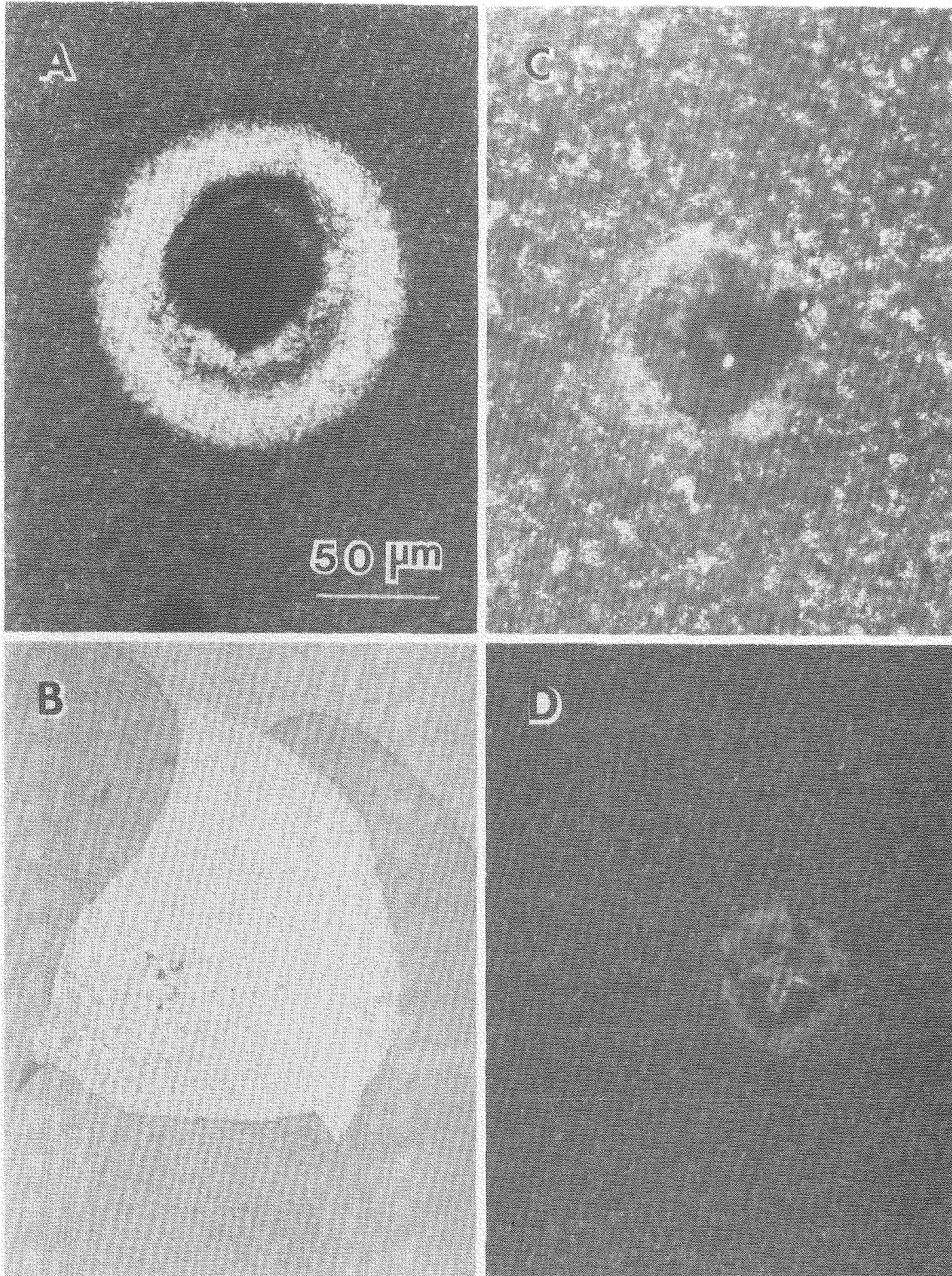
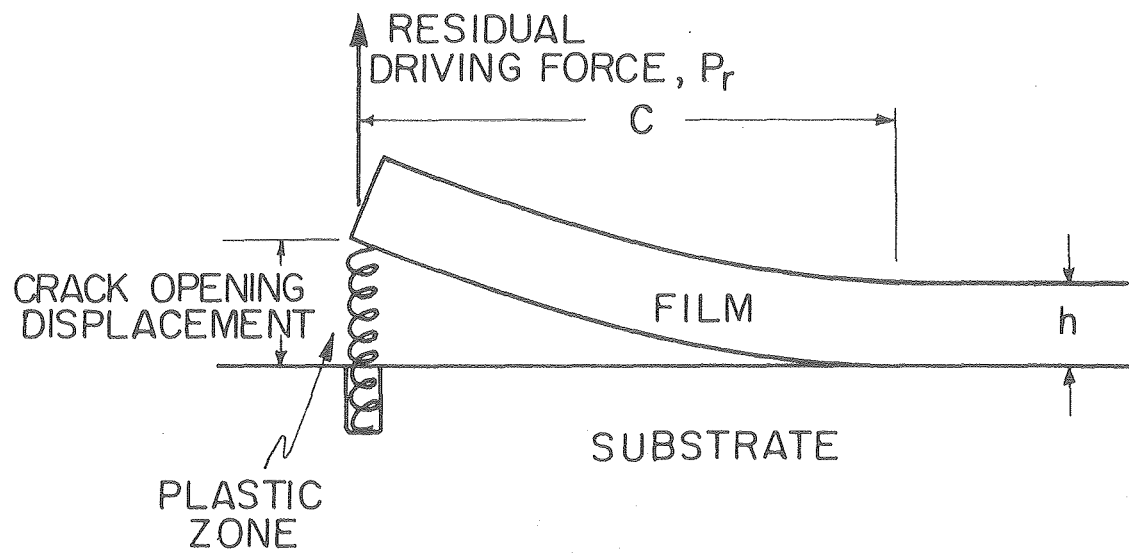


Fig. II-10

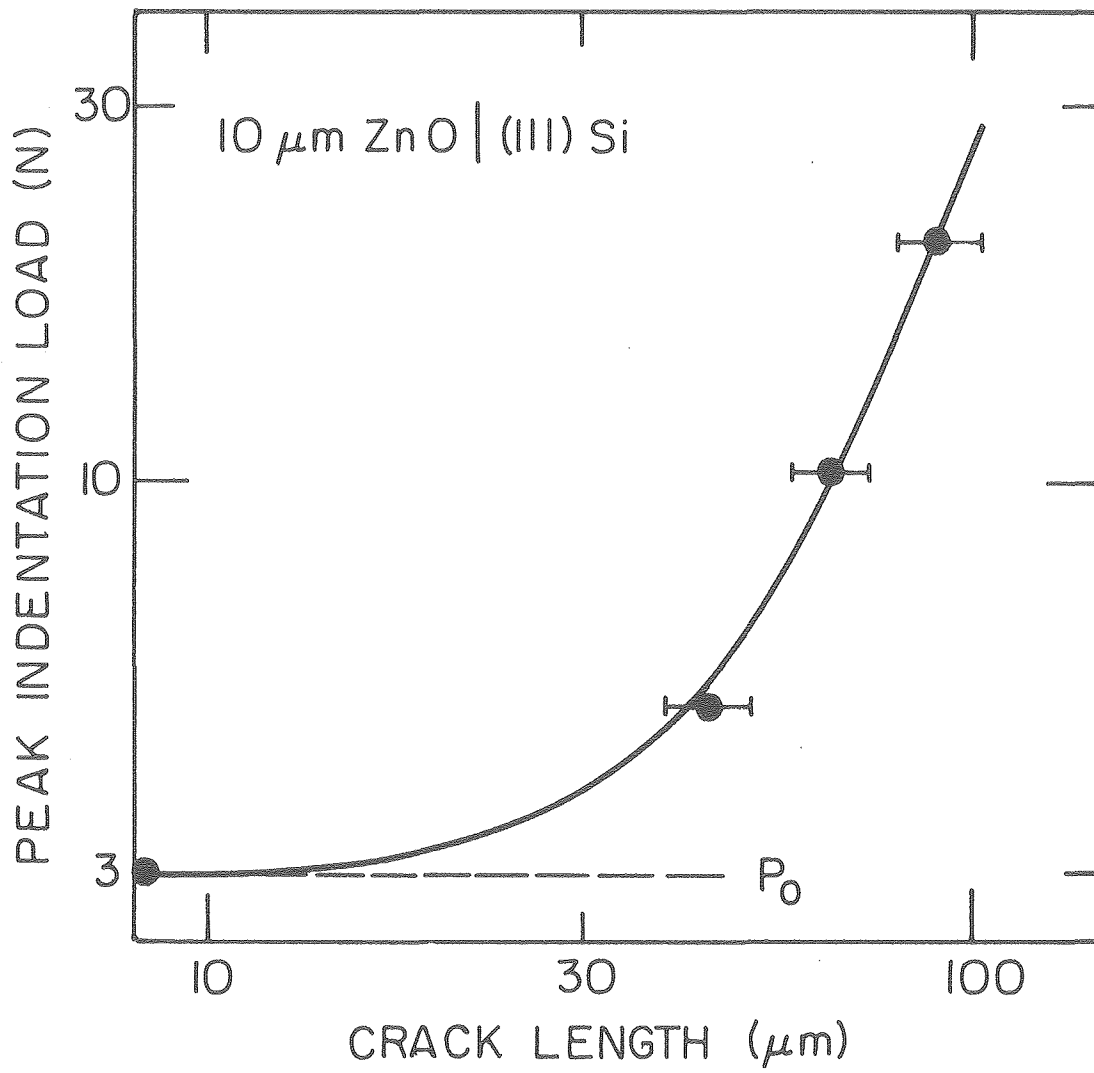
XBB807-8230

INDENTATION MODEL



XBL 8010-6084

Fig. II-11



XBL8010-6082

Fig. II-12

ACKNOWLEDGMENT

I would like to express my deep appreciation to Prof. A. G. Evans and Prof. J. A. Pask for their guidance and support during this work. It was a great pleasure working with them and being a part of many stimulating and enlightening discussions. The learning experience in Berkeley would be incomplete without being associated with each of them.

I would also like to thank Prof. R. M. White for allowing me to use the Solid State Electronics Lab. facilities and for his many helpful suggestions. Thanks are also extended to Prof. I. Finnie for his valuable comments on this thesis.

The friendly atmosphere in the lab. made this long and painstaking study much more endurable. Without the many heated discussions with my colleagues in the lab., life would be like eating food without adding spices. I'm especially indebted to those who listened to my endless preachings. In addition, I will always cherish the friendships with Dr. Tony Tomsia, Feipeng Chang (even though he is from Mainland China), Donald Huang and Y. C. Chen (both helped me through the dark ages on computer programming), Mei Chang, Bill Blumenthal, Tien Dai, Kathy Fabor, Phil Flaitz, Yen Fu, C. H. Hseuh (I can pronounce his name much better in Chinese than in English), Sing Chung Hu, Sylvia Johnson, Dr. David Marshall, Marlene Spears, and many others whom I have come to get acquainted with over the last four years.

This acknowledgment list would not be complete without including the very helpful secretaries, Mary Besser and Virginia Farr, who made my life much easier in many aspects, the University and LBL technical staffs.

Finally, I thank my parents, my brother and sister for their love, understanding and encouragement through these years.

This work was supported by the Division of Materials Sciences, Office of Basic Energy Sciences, U.S. Department of Energy under Contract No. W-7405-ENG-48.